Kaunas University of Technology

Faculty of Mathematics and Natural Sciences

Analysis of Similarity and Dosimetry Data Variability for the Left Breast Without Lymph Nodes Case

Master's Final Degree Project

Mindaugas Ilickas

Project author

Assoc. Prof. dr. Jurgita Laurikaitienė
Supervisor

dr. Laimonas Jaruševičius
Consultant

Kaunas, 2022

Kaunas University of Technology

Faculty of Mathematics and Natural Sciences

Analysis of Similarity and Dosimetry Data Variability for the Left Breast Without Lymph Nodes Case

Master's Final Degree Project

Medical Physics (6213GX001)

Mindaugas Ilickas

Project author

Assoc. Prof. dr. Jurgita Laurikaitienė

Supervisor

dr. Laimonas Jaruševičius

Consultant

Assoc. Prof. dr. Živilė Rutkūnienė

Reviewer

Kaunas, 2022

Kaunas University of Technology

Faculty of Mathematics and Natural Sciences

Mindaugas Ilickas

Analysis of Similarity and Dosimetry Data Variability for the Left Breast Without Lymph Nodes Case

Declaration of Academic Integrity

I confirm the following:

I have prepared the final degree project independently and honestly without any violations of the copyrights or other rights of others, following the provisions of the Law on Copyrights and Related Rights of the Republic of Lithuania, the Regulations on the Management and Transfer of Intellectual Property of the Kaunas University of Technology (hereinafter – University) and the ethical requirements stipulated by the Code of Academic Ethics of the University;

All the data and research results provided in the final degree project are correct and obtained legally; none of the parts of this project is plagiarised from any printed or electronic sources; all the quotations and references provided in the text of the final degree project are indicated in the list of references;

I have not paid anyone any monetary funds for the final degree project or the parts thereof unless required by the law;

I understand that in the case of any discovery of the fact of dishonesty or violation of any rights of others, the academic penalties will be imposed on me under the procedure applied at the University; I will be expelled from the University, and my final degree project can be submitted to the Office of the Ombudsperson for Academic Ethics and Procedures in the examination of a possible violation of academic ethics.

Mindaugas Ilickas

Confirmed electronically

Ilickas, Mindaugas. Analysis of Similarity and Dosimetry Data Variability for the Left Breast Without Lymph Nodes Case. Master's Final Degree Project / supervisor Assoc. Prof. dr. Jurgita Laurikaitienė; Faculty of Mathematics and Natural Sciences, Kaunas University of Technology.

Study field and area (study field group): Medical technologies, Health Sciences.

Keywords: similarity characteristics, left breast cancer, contouring, benchmarking.

Kaunas, 2022. 118 pages.

Summary

The master's final degree project focuses on using a reference delineation plan according to the recommendations of the European Society Radiation Oncology (ESTRO) in a left breast without lymph node cancer patient who has been diagnosed with a high grade of polymorphism "in situ" invasive ductal carcinoma. Breast cancer is the leading cause of cancer-related death in women (87.2 women per 100,000 population), although most patients are diagnosed with a malignancy that has not spread to other organs. Modern modelling of radiotherapy treatment is a complex procedure. Ultrasound, mammography, magnetic resonance imaging (MRI), and breast biopsy tests are used to diagnose cancer, surgical treatment, hormone therapy, chemotherapy, biological therapy, and radiation therapy are used for treatment, which can be used alone and achieve better survival results, also different treatments can be combined in between.

During the implementation of the final project, patient delineation plans were developed by the head of the Radiotherapy department (Hospital of Lithuanian University of Health Sciences Kaunas Clinics) dr. Laimonas Jaruševičius and 15 other radiation-oncologists working in a department. These plans were evaluated with a reference delineation plan (developed according to ESTRO recommendations) using the treatment planning system "Eclipse" and the open-source software "EvaluateSegmentation". The volumes of the clinical structures – *CTV_WB*, *PTV_WB*, and *PTV_WB_dvh* and the critical organs – *Heart*, *Lung_ipsilat*, and *Spinal_cord* were evaluated using the "Eclipse" system. *DICE* similarity coefficient was calculated in the "Eclipse" and "EvaluateSegmentation" software. Mathematical models were found using the "Origin 2021b".

The volumes of structures were analysed – *CTV_WB* (641.0 – 834.0 cm^3), *PTV_WB* (934.4 – 1381.4 cm^3), *PTV_WB_dvh* (761.4 – 908.3 cm^3), *Heart* (399.7 – 636.5 cm^3), *Lung_ipsilat* (1879.4 – 2057.3 cm^3), and *Spinal_cord* (26.3 – 48.5 cm^3). The ratio of PTV/CTV can explain the difference between the volumes of *CTV_WB* and *PTV_WB*; this ratio is 1.34 – 1.85 a. u. The values of the *DICE* coefficient were found to be the following: *CTV_WB* (0.88 – 0.96 a. u. (software) | 0.91 – 0.96 a. u. ("Eclipse")), *PTV_WB* (0.86 – 0.96 a. u. (software) | 0.85 – 0.97 a. u. ("Eclipse")). It has been observed that the open-source "EvaluateSegmentation" software gives very similar results to "Eclipse". Therefore the "EvaluateSegmentation" software (differently than "Eclipse") additionally can be calculated other coefficients, like Jaccard coefficient, area under the ROC curve, Cohen Kappa coefficient, Rand index, and adjusted Rand index. The value of covered the *PTV_WB_dvh* volume when the clinical goal – $V24.70 \geq 95\%$ is 75.30 – 96.18%, the value of *Heart* is 6.35 – 18.31% (V1.50 <30%), the value of *Lung_ipsilat* is 14.39 – 15.75% (V8.00 <15%), the dose value of Spinal_cord was 1.38 – 1.77 Gy (D_{max} <23.64 Gy). The dependence of the covered volume *PTV_WB_dvh* on the volume of the structure is 8-order polynomial (R^2 = 0.6504), *Heart* is the inverse polynomial with centre (R^2 = 0.9511), *Lung_ipsilat* has a linear dependence (R^2 = 0.9994), and *Spinal_cord* is a Chesler-Cram maximal function (R^2 = 0.9478).

Ilickas, Mindaugas. Kairiosios krūties be limfmazgių atvejo panašumo ir dozimetrijos duomenų kintamumo analizė. Magistro baigiamasis projektas / vadovė doc. dr. Jurgita Laurikaitienė; Kauno technologijos universitetas, Matematikos ir gamtos mokslų fakultetas.

Studijų kryptis ir sritis (studijų krypčių grupė): Medicinos technologijos, Sveikatos mokslai.

Reikšminiai žodžiai: panašumo charakteristikos, kairės krūties vėžys, kontūravimas, lyginamoji analizė.

Kaunas, 2022. 118 p.

Santrauka

Baigiamasis magistro projektas orientuotas į etaloninio kontūravimo plano pagal Europos spindulinės onkologijos draugijos (ESTRO) rekomendacijas naudojimą, kairiosios krūties be limfmazgių su didelio laipsnio polimorfizmu „in situ“ invazine latakų karcinoma sergančiam pacientui. Krūties vėžys yra pagrindinė vėžiu sergančių moterų mirties priežastis (87,2 moterys 100000 gyventojų), nors daugumai pacienčių diagnozuojamas neišplitęs į kitus organus piktybinis navikas. Šiuolaikinis spindulinės terapijos gydymo modeliavimas yra sudėtinga procedūra. Vėžio diagnozei yra naudojami ultragarso, mamografijos, magnetinio rezonanso (MRT) ir krūties biopsijos, naudojant vaizdinimo priemones, tyrimai, o gydymui pasitelkiamas operacinis gydymas, hormonų terapija, chemoterapija, biologinė terapija bei spindulinė terapija, kuri gali būti taikoma atskirai, o norint pasiekti geresnių išgyvenamumo rezultatų, skirtingi gydymo metodai yra derinami tarpusavyje.

Įgyvendinat baigiamąjį projektą buvo naudoti spindulinės terapijos skyriaus vadovo (LSMU Kauno klinikų Onkologijos ir hematologijos klinika) dr. Laimono Jaruševičiaus su kitais 15 onkologais-radioterapeutais, dirbančiais skyriuje, sukurti planai. Šie planai vertinti su etaloniniu kontūravimo planu (sukurtu pagal ESTRO rekomendacijas) naudojant gydymo planavimo sistemą „Eclipse“ bei atvirojo kodo programą „EvaluateSegmentation“. „Eclipse“ programa įvertinti klinikinių struktūrų – *CTV_WB, PTV_WB* ir *PTV_WB_dvh* bei kritinių organų – *Heart, Lung_ipsilat* ir *Spinal_cord* tūriai. „Eclipse“ ir „EvaluateSegmentation“ programomis rastas *DICE* panašumo koeficientas. Naudojantis „Origin 2021b“ rasti matematiniai modeliai.

Atlikus baigiamąjį magistro projektą, rasti struktūrų tūriai – *CTV_WB* (641,0 – 834,0 cm^3), *PTV_WB* (934,4 – 1381,4 cm^3), *PTV_WB_dvh* (761,4 – 908,3 cm^3), *Heart* (399,7 – 636,5 cm^3), Lung_ipsilat (1879,4 – 2057,3 cm^3), Spinal_cord (26,3 – 48,5 cm^3). Skirtumas tarp *CTV_WB* ir *PTV_WB* tūrių gali būti paaiškintas *PTV/CTV* santykiu, kuris kinta intervale 1,34 – 1,85 sant. vnt. Nustatyta, kad *DICE* koeficiento vertės yra šios: *CTV_WB* (0,88 – 0,96 sant. vnt. (programa) | 0,91 – 0,96 sant. vnt. („Eclipse“)), *PTV_WB* (0,86 – 0,96 sant. vnt. (programa) | 0,85 – 0,97 sant. vnt. („Eclipse“)). Pastebėta, kad su „EvaluateSegmentation“ programa gaunami labai panašūs rezultatai kaip ir „Eclipse“. Tačiau „EvaluateSegmentation“ programa (skirtingai nei „Eclipse“) galima apskaičiuoti ne tik *DICE* koeficientą, bet ir kitus panašumo koeficientus, kaip Jaccard‘o koeficientą, plotą po ROC kreivę, *Cohen Kappa* koeficientą, *Rand* indeksą ir pakoreguotą *Rand* indeksą. *PTV_WB_dvh* apsemiamo tūrio vertė, kai klinikinis tikslas – $V24{,}70 \geq 95\%$, yra 75,30 – 96,18%, *Heart* tūrio vertė 6,35 – 18,31% (V1,50 <30%), *Lung_ipsilat* tūrio vertė 14,39 – 15,75% (V8,00 <15%), *Spinal_cord* dozės vertė 1,38 – 1,77 Gy (D_{max} < 23,64 Gy). *PTV_WB_dvh* tūrio apsiėmimo priklausomybė nuo struktūros tūrio yra 8 eilės daugianaris (R^2=0,6504), *Heart* yra atvirkštinis daugianaris su centru (R^2=0,9511), *Lung_ipsilat* turi linijinę priklausomybę (R^2=0,9994), o *Spinal_cord* yra *Chesler-Cram* maksimumo funkciją (R^2=0,9478).

Table of contents

List of figures

List of tables

Introduction

Mammary cancer is the primary tumour–linked death in women, even though the most women are diagnosed with non-metastatic malignancy. Oncology tries to enhance patient outcomes by minimising procedure discomfort and improving the quality of life, not just survival [1]. In radiation therapy planning, contouring of organs-at-risk (OARs) and target volumes is critical [2]. Tumour contouring usually is done manually in clinical practice, which is time-consuming and subject to interobserver variability. As a result, precise automatic segmentation is needed [3]. However, the quality of contouring and the amount of time spent contouring are highly dependent on the radiation oncologist's experience [2]. The volumetric Dice Similarity Coefficient (*DICE*) or Hausdorff distance (*HD*), which are commonly used to assess automatic contours, have been demonstrated to be good indicators of geometric similarity, but they do not always correspond with the clinical application of the contours, or the time required to alter them [2].

Planning is a sensitive to investigator subjectivity related to human opinion, knowledge, and competence; target delineation is the cornerstone and the most vulnerable aspect of the treatment planning process [4]. Variations in the target volume delineation in mammary cancer have been extensively reported in the literature [5, 6], with significant consequences for tumour response and toxicity. Previous researches show considerable differences in proving target sizes for breast radiotherapy [7-13]. Hurkmans et al. (2001) [8] reported that the clinical target volume (breast volume) specified based on computed tomography (CT) by numerous examiners varied by 17.5% in a single systematic and analytical investigation. Struikmans et al. (2005) [12] discovered that the two sizes drawn by different researchers overlapped on average by 87% or 56% for breast and boost volumes, respectively, in another single systematic and analytical investigation. According to Stieb et al. (2019) "MRI is also of great importance for target definition, especially in cases when CT provides poor imaging contrast between the tumor and surrounding tissues" [14]. The idea of different volumes obtained by medics for the same patient is *relevance* to this topic. Also, based on Stieb et al. (2019) "Efforts to reduce observer variations in target definitions include improved imaging techniques, the use of contouring guidelines and atlases, standardization of training, auto contouring and peer review" [14].

Auto-segmentation techniques, such as atlas-based methods and deep-learning algorithms based on convolutional neural networks, have been developed in recent decades [3], which is good example of *novelty* in this field. These techniques have the potential to reduce inter- and intra-observer variability while also accelerating the contouring process. Although several studies show time savings compared to full manual contouring, the bulk of automatically generated contours still require manual modifications to make them clinically acceptable [2]. For computer vision techniques like automatic segmentation, convolutional neural networks (CNNs) are regarded as the current state of the art. Different tumour sites, such as the brain, lung, liver, and rectum, have shown encouraging outcomes for tumour segmentation [3].

It has been observed that the majority of publications examining the similarity of images are devoted to MRI images, and CT imaging studies are limited. The results of the similarity of breast cancer structures produced throughout the final project are intended to contribute to quicker image processing utilising CT data, and it would be the beginning of artificial intelligence usage in LSMU Kaunas Clinics for treatment planning and contouring process, which is *importance* of our work.

The goal of this final project was to use a reference delineation plan, created according to the European Society of Radiotherapy and Oncology (ESTRO) recommendations, for a left breast cancer

patient without lymph nodes who had a diagnosis of a high-grade nuclear polymorphism in situ part of infiltrative ductal carcinoma. Using the "Eclipse" treatment planning system, as well as the open-source software "EvaluateSegmentation", which can calculate various similarity characteristics, this reference plan would be compared to other medical plans to assess the similarity characteristics of different clinical structures (*CTV_WB* and *PTV_WB*) – benchmarking would be done. The impact of various structure volumes on the final treatment plan and its outcome in evaluating DVH curves and dose constraints are also considered.

The aim is to analyse the similarity characteristics of the treatment structures contoured manual by different radiation-oncologists and to evaluate the main dosimetry data of the planned treatment plans.

Tasks:

1. To perform segmentation process for different radiation-oncologists delineated structures in computed tomography images;
2. To analyse the similarity characteristics of target structures and organs at risk defined by different radiation-oncologists using the treatment planning system "Eclipse" and the open-source software "EvaluateSegmentation";
3. To evaluate and compare the volumes of investigated target structures and organs at risk using the treatment planning system "Eclipse";
4. To investigate the main dosimetry data of planned treatment plans for the different volumes of the delineated structures, using the treatment planning system "Eclipse".

1. Literature review

This part of the master's thesis presents statistics on breast cancer in Lithuania and the world. The types of breast cancer, their detection, and treatment methods are reviewed, as well as the methodology of radiation therapy treatment, and the different positioning of patients are introduced. The volumes of treatment and their importance in treatment planning, optimisation, and ESTRO recommendations are briefly conferred. Furthermore, dose limits for breast cancer, different dose fractionation options, the concept of DVH, computed tomography, image segmentation, threshold value concepts, types of decision errors, image compression types, and similarity characteristics calculation programs are demonstrated.

1.1. Statistics on breast cancer

Based on data from the World Health Organization (WHO), more than 17,000 oncological diseases were reported in Lithuania in 2020 [15], and almost half of these cases (8,421) accounted for women. The dynamics of cancer cases in Lithuania in 2010-2020 are presented in Table 1. The most significant increase in cases was in 2015-2017 and amounted to 23,000-25,000 cases per year, whereas in the following and previous years, the number of cases was 14,000-18,000. Due to COVID-19 disease in 2020, the number of cases could have been higher because many women did not have access to family doctors as some of the hospitals were closed. According to the WHO, breast, *colorectum*, *corpus uteri*, *cervix uteri*, and lung cancer are the most frequent types of cancer among women [15]. The classification of cancer cases in women of all ages is demonstrated in Figure 1. The most common type of cancer is breast cancer, which is one-fifth of all cases.

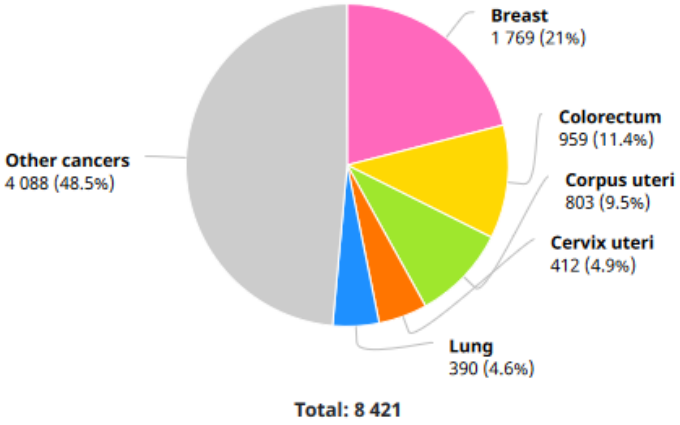

Fig. 1. Number of new cases in 2020, females, all ages [15]

Table 1. Number of cancer cases in Lithuania in 2010-2020 [15-17]

Year	2010	2011	2012	2015	2016	2017	2018	2020
Cases	17810	17862	17734	23751	24265	25346	16351	17073
Cases (for females)	8719	8742	8656	9883	10009	10098	10635	8421
Incidence per 100 000, females	522.5	535.4	537.1	630.7	646.9	662.7	706.6	253.0
Mortality per 100 000, females	222.6	232.9	227.2	236.6	237.3	236.7	239.5	87.2

The World Cancer Research Fund (WCRF) states: "There were an estimated 18.1 million cancer cases around the world in 2020. Of these, 9.3 million cases were in men and 8.8 million in women" [18]. Tumour is the leading cause of death worldwide; about 10 million people died in 2020. WHO statistics show that: "The most common in 2020 (in terms of new cancer cases) were breast (2.26 million cases), lung (2.21 million cases), colon and rectum (1.93 million cases), prostate (1.41 million cases), skin (non-melanoma) (1.20 million cases) and stomach (1.09 million cases)" [19].

Skučaitė et al. (2021) argue that over the recent decades, breast cancer has become the leading cause of cancer-related death in women across the globe, including Lithuania. Cancer is the second major cause of death among women after cardiovascular disease [20]. Examination of the document "Health Statistics of Lithuania 2018" [17], prepared by the Lithuanian Ministry of Health Information Centre, shows that cancer accounted for 18% of all the mortality cases and that the leading cause of death was a cardiovascular disease with a 63% rate. Cancer still is perceived by the general public as a deadly, life-threatening condition. Fortunately, due to the medical breakthroughs, the survival rate following the diagnosis can be relatively high, especially if the condition is detected early / at an early stage [20]. As a result, it is critical to evaluate cancer, and patient survival rates, and establish whether there are substantial disparities between patients diagnosed at various stages.

1.2. Types of breast cancer

Cancer is a condition marked by an inequality between the number of cells replicating in the body and their responses, resulting in aberrant cell proliferation or a tumour. [21]. Halim et al. (2021) state: "The tumour is classified as non-cancerous (benign) or cancerous (malignant). Benign tumours do not invade nearby tissues or spread to other areas of the body (metastasise)" [21]. A malignant tumour is composed of cancer cells that can penetrate and damage surrounding tissues and other regions of the body. Tumour cells can affect other organs, resulting in a variety of structural problems [21]. The mammary is mainly comprised of fatty tissue, with women's breasts having more glandular tissue than men. Female breasts are made up of 12-20 lobes that are also subdivided into tiny lobules. Milk ducts join these lobes and lobules [22].

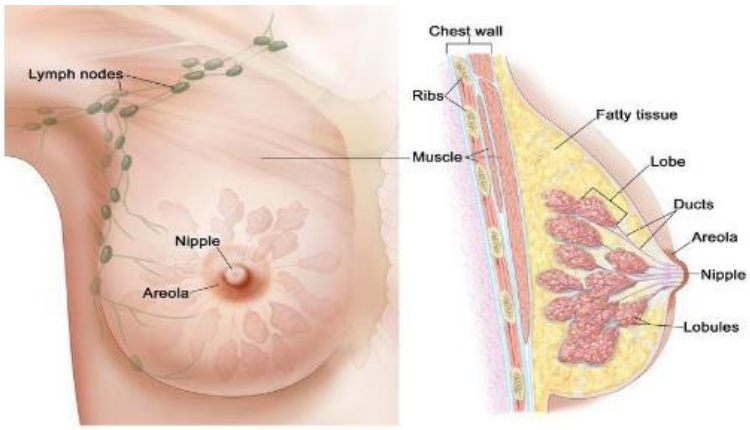

Fig. 2. Common cancer's locations in women's breasts [21]

Common locations of cancer incidence in female breasts are shown in Figure 2. Early diagnosis of tumour cells is a key step in the prevention of cell spread to other regions of the body and is a crucial step in preventing cancer cells from spreading [17]. Moreover, early identification can be accomplished by usual self-exam (once a month) and, more precisely, through early screening at local government health and private health facilities (annual check-ups) before the onset of a much more severe cancer sign [21]. According to the research, breast tumours can be either benign or malignant [22].

1.2.1. Non-malignant breast cancer

Non-invasive breast cancer is defined as a tumour that has not spread outside the lobules or ducts where it has been discovered. Ductal carcinoma *in situ* is one type of non-invasive breast tumour. Ductal carcinoma *in situ* occurs when malignant cells grow in the milk ducts but do not disseminate towards neighbouring structures or the exterior. "In situ" is a term meaning "locally". Even if atypical cells do not spread further than lobes or ducts, they can cause malignant breast tumours [22]. Here are some types of non-malignant breast cancer according to Akram et al. (2017):

- "*Lobular carcinoma in situ (LCIS)* is a kind of breast cancer that develops into breast lobules. Breast cancer has not extended exterior to the lobules into the breast tissue. Lobular carcinoma in situ is usually identified as non-invasive breast cancer" [22].
- "*Ductal carcinoma in situ (DCIS)* is the most general kind of non-invasive breast cancer and is limited to the breast duct. An example of ductal carcinoma in situ is ductal comedocarcinoma" [22].

1.2.2. Malignant breast cancer

Cancer occurs when aberrant cells from the fascicles and milk channels spread into the breast tissue. Breast cancer can spread from the mammary to many other areas of the body via the immune response or the circulatory system. It can migrate throughout the early phases of tumour growth as well as later stages. Invasive breast tumour is the most common kind of carcinoma in females. Furthermore, metastatic breast cancer is a malignant breast tumour that has spread to certain other areas of the body. The skeleton, lungs, brain, and liver are the most frequent tissues into which these cells move. These cells detach and rebuild unevenly, resulting in the formation of new tumours. Although new cells are being produced in many body regions, breast cancer still occurs [22]. Here are some forms of malignant mammary cancer according to Akram et al. (2017) work:

- "*Infiltrating lobular carcinoma (ILC)* is also recognised as invasive lobular carcinoma. ILC originates in the milk glands (lobules) of the breast but frequently extends to other areas of the body" [22].
- "*Infiltrating ductal carcinoma (IDC)* is also recognised as invasive ductal carcinoma. IDC originates in the milk ducts of the breast and extends to the duct wall, invading the breast fatty tissues and probably other parts of the body" [22].
- "*Medullary carcinoma* is an invasive breast cancer that designs a discrete margin between normal tissue and medullary tissue" [22].
- "*Mucinous carcinoma* is an uncommon breast cancer created by the mucus-forming cancer cells. Females with mutinous carcinoma usually have an improved prediction than females with additional general kinds of invasive carcinoma" [22].
- "*Tubular carcinomas* are a particular kind of invasive breast carcinoma. Females with tubular carcinoma usually have improved prospects than women with additional general kinds of invasive carcinoma" [22].
- "*Inflammatory breast cancer* in the form of swollen breasts with dimples and/or broad ridges due to cancer cells blocking lymph vessels or channels in the skin over the breast" [22].
- "*Paget's disease* of the breast. It is an uncommon type of breast cancer that usually shows visible changes to the nipple of the breast. Its symptoms include red itchy rashes involving the nipple, and then it can sometimes spread to the normal skin as well" [22].

1.3. Stages of breast cancer

The stage of mammary cancer depends on the size and type of tumour and the depth to which the cancer cells penetrate the breast tissue. Stage 0 cancers are non-invasive, while stage 4 cancers are invasive [18]. The phases of cancer in Akram et al. (2017) publication are described as follows:

- "*Stage 0* is the non-invasive stage of tumour which indicates that both cancerous and non-cancerous cells are within the boundaries of that part of the breast in which the tumour begins to grow" [22].
- "*Stage 1* describes the invasive breast carcinoma <…> 1A describes the tumour which measures up to 2 cm, and none of the lymph nodes is involved in it, while stage 1B describes a small group of cancer cells larger than 0.2 mm found in lymph nodes" [22].
- "*Stage 2A* describes that the tumour is found in axillary lymph nodes or sentinel lymph nodes, but no tumour is found in the breast. <…> Stage 2B describes that the tumour could be larger than 5 cm but can not reach the axillary lymph nodes" [22].
- "*Stage 3A* describes that no tumour is found in the breast, but it can be found in 4–9 axillary lymph nodes or sentinel lymph nodes" [22]. Stage 3B defines that cancer can be of any size and can have spread to "9 axillary lymph nodes or sentinel lymph nodes" [22]. Lastly, "stage 3C describes the spread of tumour up to 10 or more than 10 axillary lymph nodes, and it also has involved the lymph nodes above and below the clavicle" [22].
- "*Stage 4* is the advanced and metastatic stage of cancer, and this stage describes the spread to other organs of the body that is lungs, bones, liver, brain etc" [22].

1.4. Methods of detection of breast cancer

Body imaging and microwave imaging methods are two types of breast cancer screening technology [21]. Body imaging-based technologies, such as magnetic resonance imaging, mammography, and ultrasound, allow clinicians to assess and analyse breast structure. Most healthcare facilities have this equipment [21]. There is also image-guided breast biopsy [23], which is the fourth type. Microwave imaging technology can be used to replace expensive infiltration screening processes. The technology is also safe, long-lasting, and free of ionising radiation, lowering the risk to users. Microwave imaging and radio scanning are two approaches used in microwave imaging [21]. Only the first way of breast cancer screening technology is considered in this work.

1.4.1. Ultrasound (ultrasonography)

Ultrasound imaging is a medical instrument that uses high-frequency sound waves to take real-time photographs of the body's internal structures or identify disturbing nodular structures without the use of ionising radiation. Ultrasonography is a non-invasive and low-cost technique; it has two crucial functions: inside body diagnostics and pregnancy detection. The frequency range used in medical ultrasound imaging is 2–18 MHz, or hundreds of times higher than the human hearing range. During an ultrasound, a transducer rubs the patient's skin over the region being studied. Figure 3 shows examples of ultrasound breast images classified into three categories: normal, benign, and cancerous [21].

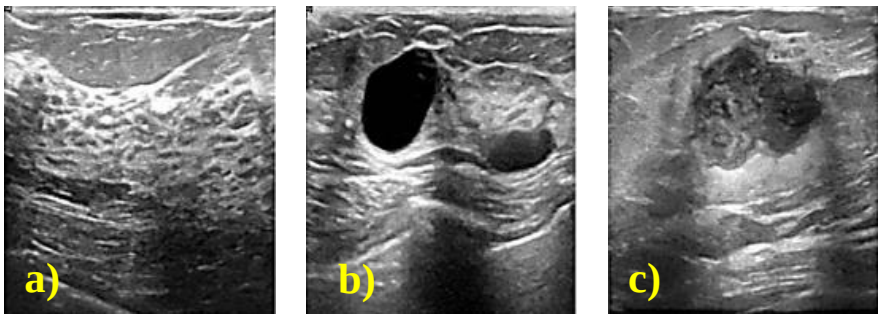

Fig. 3. Samples of ultrasound breast image: a) Normal; b) Benign; c) Malignant [21]

1.4.2. Mammography

Mammography is a low-energy X-ray process used to create mammary images. It can be used to check or diagnose patients who have symptoms or do not have symptoms of the disease. For two views of each breast, the usual radiation dose is roughly 0.4 mSv or 30 kVp. 2D mammography merely compresses the breast and gives pictures from the front and side. 3D mammography creates X-ray pictures of the breast by obtaining many views in an arc over the breast. The mammary is pressed between two rough surfaces during the treatment to separate overlapping mammary tissue and minimise breast thickness. Then, as illustrated in Figure 4, an X-ray scan of the breast produces a black-and-white image projected on a computer monitor and evaluated for cancer symptoms by a radiologist. Women with larger breasts should avoid mammography since it is more prone to produce random errors due to the overlaps of healthy fibroids [17].

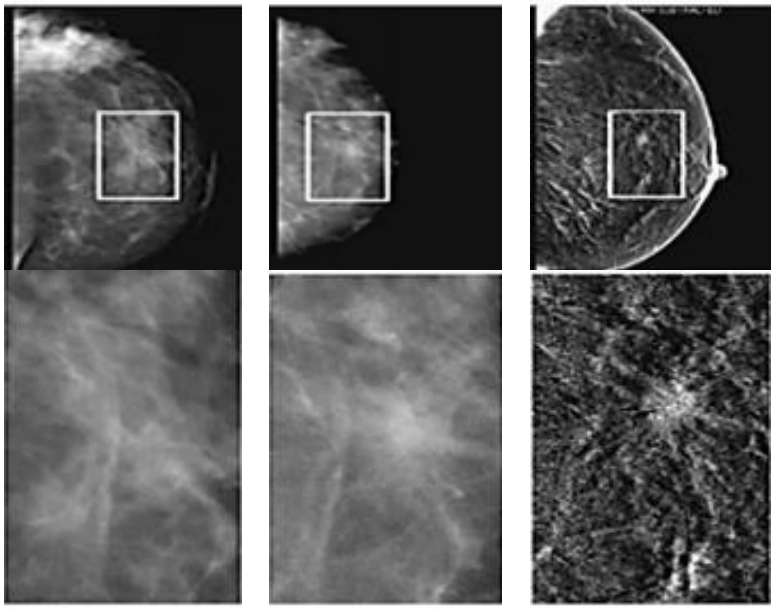

Fig. 4. Conventional mammogram of breast cancer [21]

1.4.3. Magnetic resonance imaging (MRI)

Halim et al. (2021), in publication, state that "Magnetic Resonance Imaging (MRI) is a medical imaging technique that records changing strong magnetic fields and radio waves to produce detailed images of the organ and soft tissues of the human body" [21]. MRI is the most effective imaging technique for identifying structural abnormalities in the body, with high precision and sensitivity. However, magnetic resonance imaging is a costly technique with a long waitlist. Magnetic resonance imaging is a radiological treatment that does not employ the dangerous ionising radiation of X-rays; it generates a powerful magnetic field and binds the body's protons (p^+) to the magnetic field. According to Halim et al. (2021), "A radio-frequency current is pulsed through the patient's body that disrupts the proton and forces it into 90-degree or 180-degree realignment with the static magnetic field. The scanner can identify the energy signal from the patient's body when the radio frequency is switched off" [21]. On the monitor, the algorithms used to generate the final image as shown in Figure 5. The highest sensitivity was achieved by combining mastography, magnetic resonance imaging, and specific clinical procedures – 94.4% [21].

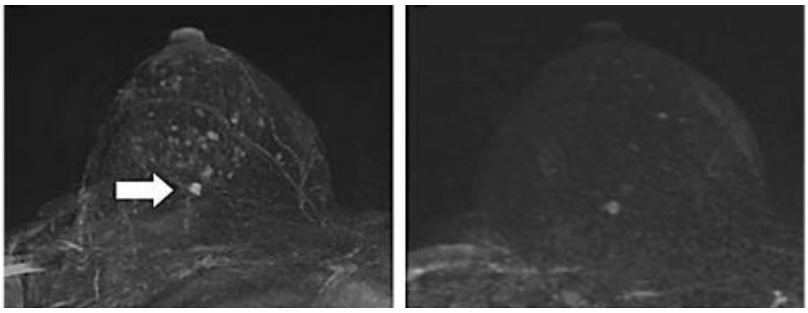

Fig. 5. A typical finding of breast cancer (arrow) detected on MRI [21]

MRI is a unique way of testing high-risk patients for mammary cancer, analysing the severity of the condition in patients with such a new diagnosis, carcinoma of the unidentified primary artery, evaluating response to neoadjuvant chemotherapy, and detecting native re-occurrence in people undergoing breast preservation regimen due to its sensitivity [24]. In Magnetic resonance imaging examination, structures that are invisible in CT scans, for example, brachial plexus and blood veins. According to Li et al. (2010), "Because of its increased soft-tissue contrast and multiplanar capability, MR imaging is well suited for evaluating the brachial plexus in its entirety, from the ventral rami to the peripheral nerve branches at the axillary level" [25].

1.4.4. Image-guided breast biopsy

Percutaneous needle biopsy guided by visual images is essential in the treatment of painful breast lesions detected by screening or clinical abnormalities. This is a safe and not-expensive process of enabling accurate diagnosis, which is necessary for proper decision-making and treatment planning. Diagnostic surgical excision, linked with a prolonged hospital stay, higher expenses, and potential dangers, has almost been replaced with non-invasive mammary imaging-guided biopsy. On a visual basis, mammary biopsy and localisation procedures are available, each with its benefits and drawbacks. Radiologists select the best acceptable procedure for each case [26]. A view of the biopsy procedure is shown in Figure 6.

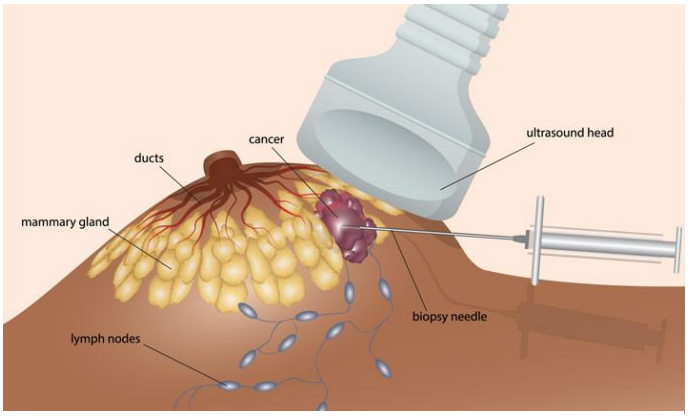

Fig. 6. Biopsy procedure using ultrasound imaging possibility [26]

1.5. Types of breast cancer treatment

When diagnosing breast cancer, it is important to choose the right treatment tactics. The earlier a modern and appropriate treatment is administered, the greater the chance of recovery [27]. The following treatments for breast cancer are available: surgical treatment, hormone therapy, chemotherapy, biological therapy, and radiation therapy.

1.5.1. Surgical treatment

Surgical therapy is a procedure that removes a tumour on a local level. The surgical approach is determined by the disease's size, location, and stage. Surgical treatment options include the following [27]:

- During *breast-sparing surgery*, the tumour is removed, along with a certain amount of surrounding tissue and axillary lymph nodes. The goal of this procedure is to remove as little healthy tissue as possible. Radiation treatment is used after surgery to remove any leftover cancer cells. Mammary preservation surgery can only be performed if mammary cancer is detected early.
- If the tumour is large or cancer cells are found in various parts of the breast, then *mastectomy* is the most appropriate treatment. Lymph nodes are usually removed during any breast cancer operation. To ensure that mammary cancer does not spread beyond the mammary, it is necessary

to remove lymph nodes from the armpits and choose the most appropriate alternative treatment tactics. In exceedingly small mammary tumours, their spread is rare, and there is enough to remove a so-called “protective” lymph node on the armpit.

1.5.2. Hormone therapy

In the progression of mammary cancer, a woman’s hormonal or endocrine system plays a critical role. Female estrogen and progesterone hormones affect breast cancer growth and spread. To apply hormonal therapy, it is necessary to determine whether the tumour has hormonal receptors. The more receptors the tumour has, the better the results of hormone therapy. The target of such treatment is to lower the number of female sex hormones or prevent them from attaching to cancer cell receptors. The growth slows or stops during hormone treatment [27].

1.5.3. Chemotherapy

Chemotherapy is a specific cancer drug that destroys mammary cells. Whether chemotherapy is used alone or in combination with other techniques (such as surgery, radiation, hormone therapy, etc.), the type of cancer determines it. Chemotherapy treatment lasts 3-6 months and takes the form of cycles. After chemotherapy, the number of cancer cells is reduced, and their growth rate and spread are stopped [27].

Chemotherapy is used: as an adjunctive treatment (other therapy that is utilised in conjunction with the primary treatment.) after surgery or as radiation therapy, as neoadjuvant therapy before surgery if the tumour is detected at a later stage. After chemotherapy, the size of the tumour decreases so that the tumour can be removed surgically. Chemotherapy is continued after the operation, in the case of advanced disease, when other organs are damaged. Cytotoxic drugs act on cells that divide quickly, especially cancer cells. Unfortunately, anticancer drugs also affect normal cells. Headache, vomiting, diarrhoea, loss of hair, oral ulcers, and anaemia are among some of the side effects. Although side effects during treatment can be profoundly serious, they usually disappear after treatment is stopped [27].

1.5.4. Biological therapy

Biotherapy is a new way of treating advanced mammary cancer. During this treatment, the patient’s immune system is used to kill cancerous cells. In individuals with a HER2 gene mutation, biological treatment using monoclonal antibodies is employed. This kind of breast cancer is more aggressive and resistant to normal therapy. Monoclonal antibodies (antibodies produced by a single cell clone) are proteins that are synthesised artificially that target cancer cells in the body. Healthy cells are not at risk. Combining biological treatment with chemotherapy can have positive results [27].

1.5.5. Radiation therapy

After surgery, radiation therapy is often used, i.e., irradiation to kill any remaining cancer cells. If only part of the breast is removed, the rest is usually irradiated. Radiotherapy after breast surgery is necessary only if some tumour cells remain in the chest after the surgery. In this case, there is a risk that they may cause the tumour to grow in the same place again. Sometimes an irradiation procedure is performed before surgery. This is usually done to reduce the tumour so that it can be removed surgically. Radiotherapy also treats metastases, such as bone metastases [27]. There are two types of radiation therapy [27]:

- *External radiation therapy* – ionising rays are directed to the tumour at a certain distance from the body surface. This type of radiation is used more frequently.
- *Internal radiation therapy* – ionising radiation sources are near to cancer (attached to the tumour or inserted into the cancer tissue).

High doses of ionising radiation damage or kill cells, inhibiting their growth and proliferation. Tumour cells are more sensitive to radiation because they grow and multiply faster than the cells in the surrounding healthy tissues. Normal cells recover faster and better after irradiation. The treatment plan is designed to minimise damage to surrounding healthy tissues. One treatment session lasts for a brief time, during which the patient does not feel any pain. The duration of the entire treatment depends on the type and size of the tumour. Side effects may occur during treatment. Exposure can cause temporary weariness, weight loss, and hair loss, notably in the armpits [27].

1.6. Methodology of radiation therapy treatment

Following breast-conserving surgery, the typical treatment is adjuvant radiation. According to a meta-analysis, added, conventional 3D radiation lowers the risk of subsequent exposure and consequently improves long-term survival by 5-10%. Body parts such as the lungs, heart, and breast, on the other hand, are unintentionally exposed in the opposite direction. Irradiation of the left breast has long-term repercussions, such as an elevated risk of heart disease and the formation of secondary malignancies [28].

According to Karpf et al. (2019): "The first step in planning a radiation therapy treatment is the accurate definition of the target volume. Multiple overlapping beams are then used to create a brick-shaped central region of high dose distribution" [29]. Volume-modulated arc therapy (VMAT), intensity-modulated radiotherapy (IMRT), and deep inspiration breath-hold (DIBH) are examples of modern radiation techniques that have been designed to boost target volume extent while reducing exposure to normal tissues [28].

Karpf et al. (2019) state that: "IMRT is an advanced form of three-dimensional conformal radiotherapy. It is of particular value for target volumes with concave or complex shapes with proximity to radiosensitive normal structures" [29].

Even with adjuvant radiation therapy for mammary cancer, a few planning research findings have shown enhanced dose distribution, a higher index of compliance, and homogeneity when using incorporated enhancement (a method that allows multiple targets to be irradiated at different doses during the same treatment session while maintaining healthy organs) [30].

Buwenge et al. (2017) say: "VMAT is a form of IMRT in which the dose of radiation is applied to the tumour by continuous 360º rotation of the treatment unit. The dose distribution is precise with the shaping and adaptation of the dose to the form of the tumour" [31]. VMAT concentrates radiation on the tumour while sparing healthy tissues. Each VMAT treatment takes less than two minutes to complete. Faster treatments enhance radiation delivery accuracy while improving patient comfort and quality of life [32]. A comparison of different treatment systems is presented in Figure 7.

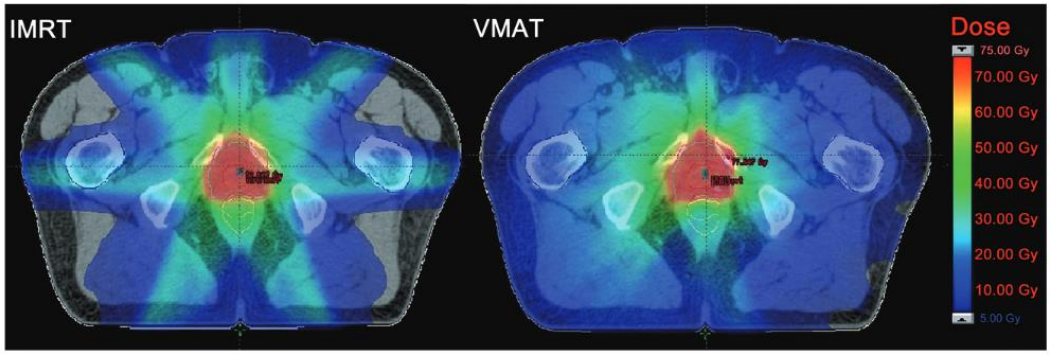

Fig. 7. Isodose diagram for IMRT (left) and VMAT (right) [33, 35]

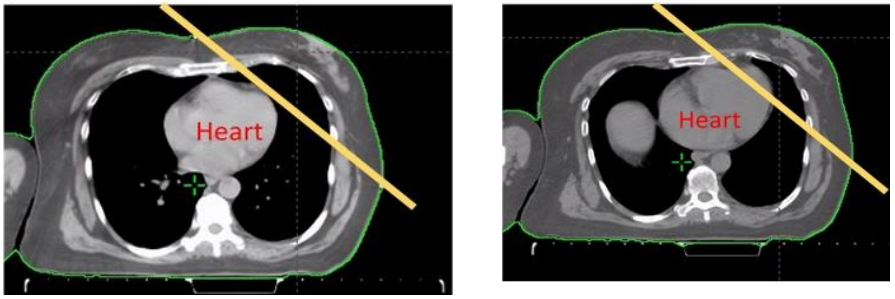

Fig. 8. Comparison of respiratory gating and DIBH with free-breathing [34]

Stony Brook University Cancer Center says: "Gating is a system that tracks a patient's normal respiratory cycle with an infrared camera and chest/abdomen marker. The system is coordinated to only deliver radiation when the tumour is in the treatment field" [34]. DIBH is a radiation approach for treating breast cancer that reduces doses in the heart and lungs. Radiation is only injected during the DIBH process at a specified point in the patient's respiratory cycle, during the inspiration and expiration cycles. Concerning the Stony Brook University Cancer Center: "This, in turn, will limit the amount of the heart and lung that is exposed to the radiation beam, since taking a deep breath in will allow these organs to move out of the treatment field" [34] (see Figure 8). DIBH could also be used to keep internal organs, including the stomach, pancreas, and liver, from moving freely [34].

1.7. Positioning for Breast Cancer Treatment

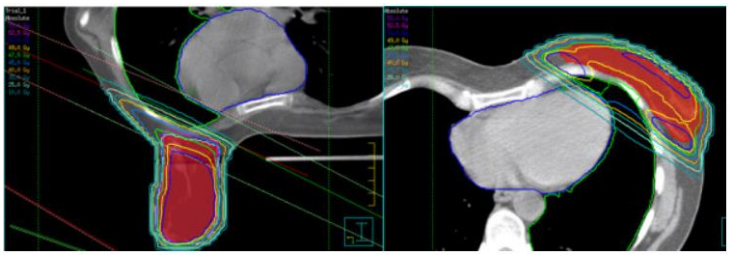

Fig. 9. Treatment strategies in laying forward (right) and laying backwards (left) positions [36]

Several patients with acute mammary cancer are candidates for mammary conservation accompanied by whole-breast irradiation (WBI), commonly done lying horizontally with the face and torso facing up (see Figure 9). However, the supine WBI has serious disadvantages, including lateral mammary movement, highlighting the inframammary fold, and incorporating the lung and heart into the therapeutic plan. Based on the Cooperman Barnabas Medical Center: "In particular, irradiation after breast-conserving surgery (BCS) in women with large and/or pendulous breasts is a challenge for radiation oncologists. Increased radiation-related toxicity and worse cosmetic outcome were found in patients with large breasts and/or increased body mass index (BMI)" [36].

Patients lie on a specially constructed table (see figure 10) that allows females to lie comfortably on their stomachs with their breasts dangling away from their bodies. Radiation is delivered to the tumour while lying in a prone posture, reducing exposure to the surrounding organs and tissues, particularly the heart and lungs. Radiation delivered through the prone breast has a consistent and exact radiation dose [37]. Boute et al. (2017) write: "The radiation is distributed evenly, accurately, and directly to avoid lung and heart tissues. For the larger-breasted patient, this method has been proven to reduce skin toxicity and improve long-term cosmetic outcomes" [37].

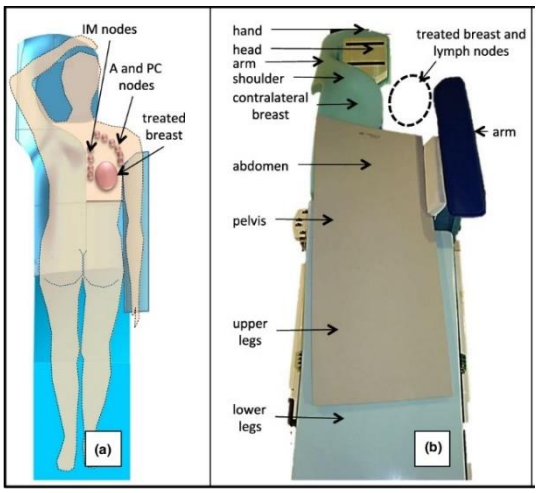

Fig. 10. a) The crawl placement device's asymmetric fork form is visible from above through a semi-transparent depiction of a patient; b) Right-side irradiation photograph taken from above the crawl Breast couch's caudal end [38]

1.8. ESTRO consensus guideline

The weakest link in the radiation therapy quality chain is currently target volume delineation. Lymph nodes, mammary, and chest walls are all identified differently in this location. Several guidelines for defining the target volume in acute-stage mammary cancer have been released to help with this. There have also been suggestions for cardiac atlases, and algorithms for auto-segmentation of target volumes to aid radiation therapy planning have recently been developed. The majority of these parameters result in more enormous therapeutic volumes than typical model-based radiotherapy [38]. To solve this problem, guidelines of the European Society of Radiotherapy and Oncology were submitted. The target volume covers the entire glandular breast tissue, and the boundaries are often invisible.

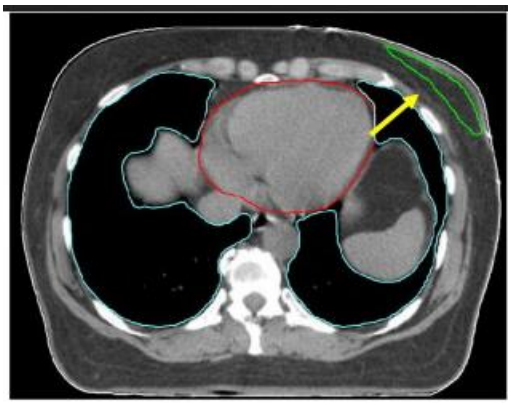

Fig. 11. Due to fatty tissue, the CTV_p breast is positioned more centrally in the caudal portion of the breast in obese patients [38]

Table 2. The guidelines of the ESTRO on the characterisation of the target volume for the choice of radiation treatment in acute-stage mammary cancer [38]

Borders	CTV_p breast
Cranial	The upper margin of palpable/visible breast tissue, up to the inferior boundary of the sternoclavicular joint
Caudal	Most caudal CT slices with visible breast
Ventral	5 mm beneath the skin surface
Dorsal	Major pectoral muscle or costae and intercostal muscles where no muscle
Medial	Lateral to the medial perforating mammalian vessels; maximally to the edge of the sternal bone
Lateral	Lateral breast fold; anterior to the lateral thoracic artery

Birgitte et al. (2015), in their work, write: "Before CT scanning, two circles of radio-opaque wires were placed around the breast representing the palpable/visible CTV breast (the inner circle) and the

provisional field borders (outer circle) to aid in target volume delineation. The scans were made under free-breathing conditions and with 2.5 mm thick sections" [38] (see Table 2).

The dorsal border of the breast can be adjusted ventrally/ventrolaterally in the caudal breast, especially in obese patients with a thick layer of the submucosa, because subcutaneous fat extend from the abdomen wall and does not enter the CTV. In left-sided situations, this can reduce the dose reaching the heart [38] (see Figure 11).

1.9. The treatment volume and its optimisation

The Reports of the International Commission on Radiation Units and Measurements (ICRU), specifically ICRU Report 50 [39], developed many volume ideas (see Figure 12):

- Clinical target volume (CTV).
- Gross tumour volume (GTV).
- Planning target volume (PTV).
- Internal target volume (ITV).
- Planning organ at risk volume (PRV).
- Organs at risk (OARs).
- Irradiated volume (IV).
- Treated volume (TV).

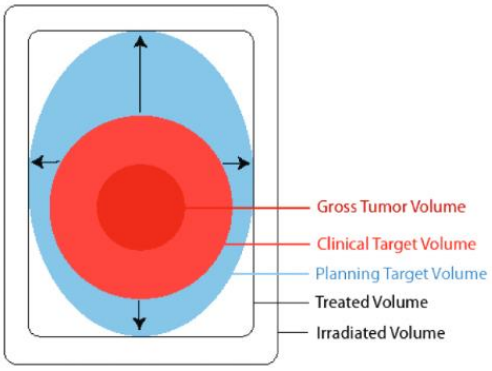

Fig. 12. Visualization of various volumes as stated in the ICRU 50 report [40]

Only GTV, CTV, and OARs are tissue representation concepts; the others are geometric notions that do not adequately depict tissues or organs' volume.

Based on Berthelsen et al. (2007) publication: "The *gross tumour volume (GTV)* is the gross palpable or visible/demonstrable extent and location of the malignant growth. The GTV may consist of the primary tumour (GTV-T), metastatic lymphadenopathy (GTV-N), or other metastases (GTV-M)" [40]. In malignant growth zones, GTV is usually invariably linked to the greatest density. Because of the dense population of cancerous cells in the GTV, radical treatment necessitates. Based on delivering a significant dosage to the whole GTV to achieve tumoral control. If the tumour has already been removed, for example, by previous surgery, no GTV can be seen. To establish the form and size, clinical examination and imaging methods may be employed. No GTV can be observed if the tumour has previously been removed, for example, by earlier surgery. Depending on the screening method, the size and form of the GTV might vary significantly. As a result, radiologists and oncologists must explain how they assessed and defined GTV for each patient. The image format, such as the DICOM standard, should allow the integration of data from many imaging devices. Cross-servers are likely to change because GTV imaging is often subjective during a radiotherapy planning scan. GTV may or may not exceed typical organ or tissue limits [40].

According to Berthelsen et al. (2007) publication: "The *clinical target volume (CTV)* is a tissue volume that contains a demonstrable GTV and/or is considered to contain microscopic, subclinical extensions at a certain probability level. This volume thus has to be considered for therapy and, if included, should be irradiated adequately to achieve cure" [40]. The requirements are based on the concept that tumour cells may exist at certain probability levels in anatomically recognised tissues or organs, even if they are not visible. Clinical experience collected through well-documented therapy and follow-up determines the degree of probability. When treatment is not properly treated in

"subclinical" scenarios, the frequency of the risk of symptoms being detected in the future (risk of failure) can be described for a therapeutic prescription [40].

Based on Berthelsen et al. (2007) work: *"*The *internal target volume (ITV)* consists of an internal margin added to the CTV to compensate for internal physiological movement and variations in size, shape, and position of the CTV" [41].

PTV is a geometric idea whereby guarantees that CTV receives the radiation dose which is specified. It is a volume that is connected to the linear accelerator rather than the anatomy of the patient. As a result, PTV may spread beyond anatomical boundaries, such as bony edges and even beyond the body. In ICRU's 62nd report, a margin was proposed to be adjusted to the change in the size, shape, and location of the CTV about the anatomical reference point. The internal margin was the name given to this volume. PTV and, in rare situations, CTV may need to be decreased to limit the dose to a neighbouring vital normal tissue, according to ICRU 62 Report. This is an important concept to grasp, especially when higher radiation doses are attempted [42].

Berthelsen et al. (2007) state: "The Radiation Therapy Oncology Group (RTOG) recommended that the margin from CTV to PTV be a uniform 7 mm in the 1304 protocol" [43]. However, most centres agree on the 0.5 cm to 1.5 cm margin between CTV and PTV [44]. It is still unclear whether the uniform buffers required by the protocol around the CTV have been effectively adjusted for setup errors. Because the level of setup mistakes varies with patient parameters and tumour core location, the uncertainties must be addressed with greater caution. Furthermore, derived from these patient data, prognostic indications for the severity of setup errors, such as age, tumour location [43], the "body mass index (BMI), chest circumference (CC) and breast volume (BV), may help to establish appropriate margins during treatment planning" according to Berthelsen et al. (2007) [43].

When a tissue volume is suspected to contain tumour cells, and a choice has been taken to try to cure the patient with radiation, the targeted volume should be optimised. The optimisation procedure is crucial to the effectiveness of the treatment, and it must ensure that the targeted tissue volume is always included in the volume that receives a high absorbed dosage (treated volume), while healthy organs are kept as far away as possible from receiving a considerably high dose (irradiated volume). The process of optimising external beam radiation should account for geometric changes in the location of the target and OARs along the treatment chain by establishing a planning target volume (PTV) and one or more planned organ at risk volumes (PRVs). Geometric changes in the radiation treatment chain determine the size of the margin surrounding the tissue volume where a high dose is required (such as organ movements and variations in patient set-up variations). To build a precise and safe margin, it is critical to detect and quantify these variances [45].

Berthelsen et al. (2007) say: "*Organs at risk (OARs)* are normal tissues whose radiation sensitivity may significantly influence treatment planning and/ or prescribed dose" [41]. OARs, like CTVs, are susceptible to both deliberate and accidental mistakes. In this case, the margin of the PTV around the CTV must be added to OAR to produce PRV. On the other hand, adding PRVs around OARs can significantly increase normal tissue structure volume and raise concerns about the radiation dose to the target. Fortunately, this is only required in a few cases. It is helpful to construct a PRV around an OAR whose damage is exceptionally severe, especially if the loss of a small amount of normal tissue as a result of radiation damage might result in a severe clinical presentation. It is important to

understand that some interaction between the PTV and a PRV may be required, and that this interaction may impact the recommended dose and dose distribution of radiation [42].

The *volume of planning organs at risk (PRV)* was included in ICRU report no. 62 to consider the mobility of internal organs and the uncertainty surrounding the definition of the outermost regions. PRV has OAR, as well as safety margins around OAR, like the planning target volume (PTV), used to keep track of geometric variance around a clinical target volume (CTV). PRV can be valuable in RT planning, especially inverse intensity-modulated radiotherapy (IMRT) planning and may increase the predicted value of dose and volume data [46].

Due to the limitations of radiation technology and in certain clinical environments, the amount of radiation received may not be exactly consistent with the PTV; it can be larger (sometimes much larger) and simpler. The term „*treated volume*“ (TV) was created. The treatment planning is decided when the beam design and all other radiation parameters are selected. The TV denotes the volume of tissue that will receive at least one dose deemed appropriate by the radiation oncologist to achieve the treatment goal, such as palliation or eradication of the tumour. Consequently, the volume treated is defined as volume limited by the isotope surface of the isotope of the dose level. Another challenge is determining the effect of PTV on normal tissues outside the treatment volume. To create the necessary correlations, imaging was required during the follow-up period. In terms of normal tissue tolerance, an *irradiated volume (IV)* is a tissue volume that is administered in massive quantities. If the amount of radiation is provided, the significant dose must be reported in relative quantity (in Gy) or the percentage of the required dose. The IV is determined by the treatment approach [40].

1.10. Limits of treatment planning for breast cancer

According to the Winship Cancer Institute of Emory University: “Radiation can harm both cancerous and normal tissues; with radiation therapy, the goal is to maximise the damage done to cancer cells and minimise the damage to normal tissues” [47]. Radiotherapy is based on the idea that rapidly evolving cells (such as cancerous cells) are more sensitive to radiation damage than regular structures, and that tumour cells recover less from radiotherapy damage than healthy tissue. The kind, size, location, and treatment goals of cancer determine the radiation technique employed. All types of radiation therapy incorporate pre-treatment visual information (such as CT, MRI, PET-CT, and 4D-CT) – this phase is known as a simulation in external radiation. The scans are frequently “fused” to give clinicians a comprehensive picture of the tumour’s size and surrounding organs. A computer application is used to construct 3D representations of the tumour and surrounding organs. The patient’s treatment plan is then created by a group of physicists, dosimeters, and clinicians who work together to optimise radiation exposure to the tumour while minimising damage to normal tissues [47].

The LSMU Oncology and Haematology Clinic uses the Fast-Forward trial protocol v5.1 of the National Institute of Health Research [48], which specifies the critical dose-volume requirements to be protected. These requirements are shown in Table 3.

Table 3. Dose-volume requirements for the organs to be protected depending on the prescribed dose [48]

Organ	40.5 Gy through 15 fractions on days I-V of the week	26 Gy through 5 fractions on days I-V of the week
Same side lung	V30.0 < 17% V12.0 < 15%	V8.0 < 15%
Heart	V2.0 < 30% V10.0 < 5%	V1.5 < 30% V7.0 < 5%

"Eclipse" is Varian's 3D treatment planning technology (which is commercial). "Eclipse" is used for treatment planning in Kaunas Clinics; clinical goals for 40.5 Gy and 26 Gy plans from this program are presented in Table 4. The structure names will be explained in the methodology part.

Table 4. The clinical goal of the "Eclipse" program

Structure	40.5 Gy through 15 fractions on days I-V of the week	26 Gy through 5 fractions on days I-V of the week
PTV_WB_dvh	V38.05 ≥ 95%	V24.70 ≥ 95%
	V42.05 < 5%	V27.30 < 5%
	V42.85 < 2%	V27.80 < 2%
	D_{max} < 44.05 Gy	D_{max} < 28.60 Gy
Heart	V10.00 < 5%	V7.0 < 5%
	V2.00 < 25%	V1.50 < 30%
Lung_ipsilat[1]	V12.00 < 15%	V8.00 < 15%
Spinal cord	D_{max} < 37.00 Gy	D_{max} < 23.64 Gy

1.11. Dose fractionation

The target point for radiotherapy depends on the type of plan. A single beam prescription point is a maximum dose point (d_{max}) or depth. On the recommendation, the total dose, dose per portion, number of fractions, and length of treatment should all be specified [50]. There are several different fractionation regimes to choose from based on Ajithkumar et al. (2011) publication:

- "*Conventional fractionation* – delivers 1.8–2 Gy single fraction per day, 5 times weekly" [50].
- "*Accelerated fractionation* – aims to shorten the treatment time by delivering larger than standard size fractions five times weekly or more than five fractions per week of 2 Gy. Multiple fractions may also be given daily. The acute toxicity is greater with this, and late toxicity is either the same as or greater than conventional fractionation. It is useful for tumours with a rapid growth rate" [50].
- "*Hyperfractionation* – aims to improve tumour control probability with the same late effects as conventional fractionation. It delivers a larger number of smaller than conventional dose fractions per day, and the total dose is 10–20% higher than standard fractionation while total treatment time remains the same. It is useful for tumours with slow growth" [50].
- "*Accelerated hyperfractionation* – combines the principles of hyperfractionation and accelerated fractionation" [50].

[1] **Lung_ipsilat** – "On the same side, as opposed to contralateral" [49]

- "*Continuous accelerated hyperfractionation (CHART)* – treatment is given as 1.5 Gy per fraction, three times daily, 6 hours apart for 12 continuous days. Proved to improve local control in lung cancer" [50].
- "*Hypofractionation* – delivers more than 2 Gy per fraction and less than five fractions per week" [50].

1.12. Dose-volume histograms

According to the Encyclopaedia of Radiation Oncology, the Dose Volume Histogram (DVH) is: "A graphical representation of the dose received by normal tissues and target volumes within a 3D radiation therapy plan. They provide information on the volume of a structure receiving a given dose over a range of doses" [51].

There are several ways to compare competitive radiation programs. DVH (see Figure 13) is a widely used method for evaluating competitive programs. Integrating substantial amounts of information into a 3D radiation dosing array is quite complex. The dose-volume histogram translates this huge data into easy-to-understand 2D graphics. Differential and cumulative DVHs are the two most prevalent forms of DVHs [52]. Regarding Sharkey and Selvaraj's (2012) work: "The differential DVH represents the percentage or absolute volume <…> receiving dose in the corresponding dose bin, whereas the cumulative DVH represents the percentage or absolute volume receiving greater than or equal to the value in the corresponding dose bin" [52]. Other radiobiological strategy parameters, like the chance of tumour control (TCP) and the chance of normal tissue compliance (NTCP), are determined by these DVHs [52].

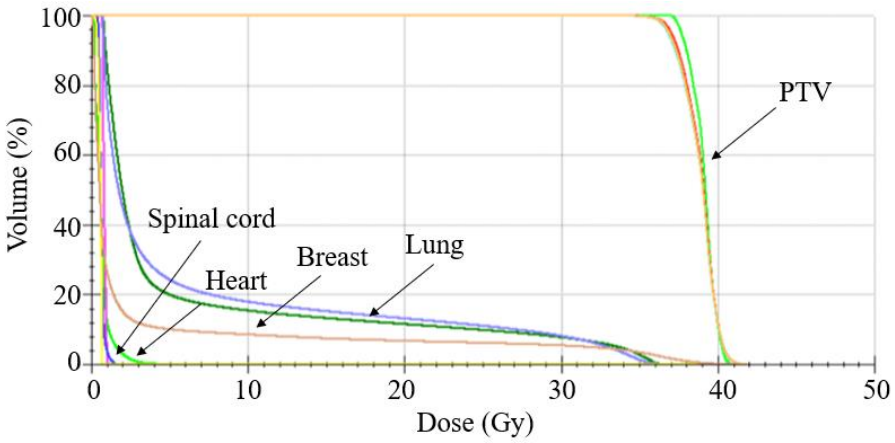

Fig. 13. DVH for breast cancer patients [53]

DVH can be utilised in the planning phase to see if the dosage is sufficient and homogeneous for the target volume, or if there are areas and sizes of healthy tissue nearby. DVHs may be used as a preliminary step for analysing treatment protocols or as a screening instrument to select the best or least acceptable plan from a range of plans before looking at more comprehensive data in the form of 2D or 3D isodose representations [54].

1.13. Computed tomography (CT)

The term "computed tomography" or CT refers to a computerised X-ray imaging system whereby an X-ray boundary column is aimed at a continuous body and spins rapidly around the body to create impulses processed by a machine computer to generate cross-sectional pictures or "sections". These slices yield tomographic images, which are more detailed on a point-by-point basis than standard X-rays. After the system's unit gathers multiple progressive cuts, they can be "stacked" together to

generate a 3D representation of the cuts, making it easier to spot facts and critical structures, as well as probable tumours or anomalies [55]. Figure 14 shows the CT scanning method. CT scanning is one of the most accurate ways to detect and measure the size and location of some cancers. CT scans are painless, rapid, non-invasive, and exact. Internal bleeding and injuries can be detected quickly enough in an emergency to save lives [57].

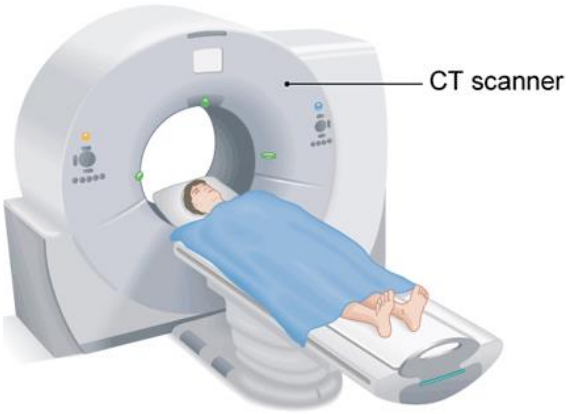

Fig. 14. CT scanning procedure [56]

Caldemeyer and Buckwalter (1999), in their publication, state: "As X-rays pass through the patient, they are attenuated. The amount of attenuation depends on the type of tissue through which the X-ray beam passes" [58]. Changes in attenuation between neighbouring tissues provide contrast in X-ray examination [58]. Based on Caldemeyer and Buckwalter's (1999) work: "The higher the attenuation of the X-ray beam, the brighter the tissue on CT images, and the lower the attenuation, the darker the tissue on CT images. Therefore, bone and calcification that significantly attenuate the X-ray beam are white" [58]. The X-ray beam is greatly reduced by white bone and calcification. Because fat contains more carbon, which effectively attenuates X-rays, it is more transparent than oxygen-containing water. As a result, fat appears on CT to be darker than water. The air is incredibly dark and has no X-ray attenuation (see figure 15). Increased (white) or reduced (black) attenuation or density will be labelled in areas or local deviations from the conventional CT picture [58].

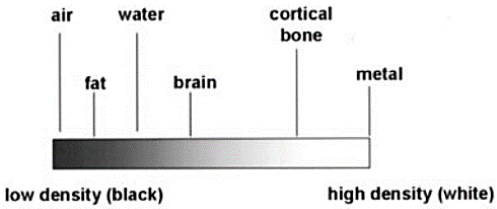

Fig. 15. Relative CT density of structures [58]

The underlying premise of CT is that the density of tissue examined by X-rays may be calculated using the attenuation coefficient computation. Using 2D slices perpendicular to the acquisition program's axis, this approach is utilised to rebuild the body's mass [59].

Bell (2021), in his publication, states: "The CT X-ray tube (typically with energy levels between 20 and 150 keV) emits N photons (monochromatic) per unit of time. The emitted X-rays form a beam that passes through a layer of biological material of thickness Δx" [59]. The detector is $N + \Delta N$ photon close to the sample selection exit test, with ΔN less than 0. The dataset, as well as the X-ray pulse attenuation parameters used for a three-dimensional model of the inspected element, are preserved. The photoelectric and Compton effects are the 2 most common absorption phenomena. Regarding Bell's (2021) work: "In the particular case of the CT, the emitter of X-rays rotates around the patient, and the detector, placed on the diametrically opposite sides, picks up the image of a body section. A CT scanner measures the transmission of a thin beam (1-10 mm) of X-rays through a full scan of the body. The image of that section is taken from different angles, and this allows to retrieve information on depth" [59]. The depth data can be obtained by taking segments from different angles (in 3D). To make person tomography images from data from "raw" scans, computers employ strong, complex algorithms to reconstruct images. The attenuation coefficients of irradiated tissue volumes may be computed using conventional X-ray absorption equations in the area if X-rays are transformed to monochromatic or quasi-monochromatic when the tube leaves using the correct filter [59]:

$$I = I_0 e^{-\mu x} \quad (1)$$

Where I is the intensity of the X-ray beam travelling through the thickness x of the material, I_0 is the initial intensity of the X-ray beam, μ is the linear absorption coefficient of the researched material in cm^{-1}, and x is the thickness of the studied material.

The Hounsfield unit is calculated using the formula [60]:

$$HU = \left(\frac{\mu_x - \mu_{water}}{\mu_{water} - \mu_{Air}}\right) \cdot 1000 \quad (2)$$

Various Hounsfield units are shown in Table 5.
To rebuild the image of the section irradiated by X-rays of objects, many measurements of attenuation coefficients are needed. It captures all the detection data, as well as the fundamental amounts of content. The basic surfaces of the image reconstructed from the reconstruction project of the data matrix are displayed on the computer, controlled by the damping coefficient.

Table 5. Various Hounsfield unit values [59]

Material	**Value, HU**
Air	-1000
Fat	-60 to -120
Water	0
Compact bone	+1000

Each voxel (volume element) in the CT scanner image depicts the tissue of the patient, which is a computer image made up of square element (pixel) matrices. Based on Bell's (2022) work: "Measurement made by a detector CT is proportional to the sum of the attenuation coefficients. The typical CT image is composed of 512 rows, each of 512 pixels, i.e., a square matrix of 512 × 512 = 262,144 pixels (one for each voxel)" [59]. In imaging, the attenuation coefficient of every voxel correlating to all these pixels is crucial. Each point in the image is encircled by a halo-shaped circle, which reduces contrast and blends the subject's edge. A filtered back-projection approach is employed to avoid this. The decreasing trend of the negative value of the filter function is eliminated when the purified projection is reflected backwards, yielding an image that is a replica of the original object. The CT scan compensates for the attenuation of the X-ray attenuation as it travels through the body. It differs from traditional radiography in several ways, including using a large number of attenuation coefficients to reconstruct the image [59].

1.14. Image segmentation and threshold

Image segmentation analysis is a technique for examining image shapes and regions, particularly their edges. It is used in various fields, including medical imaging, computer vision, and ecological studies [61]. In medical image analysis, 3D image segmentation is a critical image processing stage. The main goals of surgical preparation are high accuracy (including high repeatability) and minimal bias segmentation techniques, as they have a direct influence on outcomes. Detection and documentation of development [62].

Depending on the size of the bodily component portrayed and the picture quality, medical 3D images are specified on 3D grids. Grid size ($w \times h \times d$) is represented by the width, height, and depth of a 3D picture. A voxel is a three-dimensional grid point. Binary segments may be thought of as segments that classify the voxels of an image as components of an anatomical feature. White matter, grey matter, brain lesions, body organs, and are all anatomical features. Segmentation assessment is the task of finding the difference or similarity between two segmentations by comparing them, where one

is the segmentation to be measured, and the other is the comparable segmentation of the ground reality [62].

Concerning Taha and Hanbury's (2015) publication: "Medical segmentations are often fuzzy, meaning that voxels have a grade of membership in [0, 1]. This is e.g., the case when the underlying segmentation is the result of averaging different segmentations of the same structure annotated by different annotators" [62]. The segmentation of voxels representing a variety of groups might be deemed plausible in this regard. Pure segmentation is a method of estimating ambiguous segmentation by limiting the number of binary pictures to a certain value. Thresholding, on the other hand, is a tentative estimate that is not always accurate. Furthermore, the difficulty of deciding on a threshold endures because the test's outcomes are dependent on it. This is why measurements that can compare fuzzy segmentations without losing data have been included. Another common interpretation of fuzzy partial volume fuzzy segmentation is that the voxel value refers to the percentage of the voxel that belongs to the class [62].

In the 3D segmentation of medical images, several quality parameters are created, depending on the type of segmentation error that could be specified. The measures are expected to identify these errors, according to information and segmentation. Quantity (number of segments), area of segmented objects, outline (degree of edge matching), and content are four forms of image segmentation errors based on four main categories of failures (added areas, additional context, internal holes, and border holes). Two quality aspects were defined under the first category (accuracy): boundary delineation (contour) and scale (volume of the segmented object). When segmented elements are very tiny, orientation, which describes the general direction of the divided element, may be more essential than size and contour [62].

Metric sensitivities are another difficulty in identifying measurements. Sensitivity to certain attributes may prevent or lead to overestimation or underestimating specific mistakes. Metrics are influenced by outliers (small segments outside the major objective), class mismatches (object sizes relative to the backdrop), and multiple segments. Another form of sensitivity is the inability to cope well with a chance agreement. This is associated with baseline levels, which should ideally be zero when executed at random, showing no resemblance [62].

There is a need for a standardised medical image segmentation evaluation approach that standardises not only the metrics to be employed but also the meaning of the metrics. There are significant measurements, such as theoretical knowledge metrics, statistical metrics like distance from Mahalanobis, and chance correction metrics such as Cohen Kappa and modified Rand index [62].

The thresholding approach is the most fundamental image segmentation technique. In this procedure, a threshold value is used to transform a grayscale image into a binary image. A major aspect of the system is the option to select threshold values [63]. The threshold method [64] is described as:

$$T = T[x, y, p(x, y), f(x, y)] \tag{3}$$

T is the threshold, *x* and *y* are the threshold value's coordinates, and *p(x, y)* and *f(x, y)* are the image's grey-scale pixels. *g(x, y)* is the threshold image and is defined as [64]:

$$g(x,y) = \begin{cases} 1 \; if \; f(x,y) \geq 1 \\ 0 \; if \; f(x,y) \leq 0 \end{cases} \tag{4}$$

By assigning all grey levels underneath the threshold value to black and those just above the threshold value to white, or vice versa, picture attributes may be reconstructed from the background using a threshold technique [63]. This method, however, has flaws and can result in insufficient picture signals and noise reductions [65]. Too high a threshold leads to data loss, while too low results in distracting background clutter. Examining a given image's grey-level histogram is a typical way to automatically find a threshold at which to segment it. Many image analysis tasks rely on the threshold, including computerised word recognition, either typewritten or handwritten, radiography image improvement in the medical field, and nuclear physics, whereby particle trails and impacts in the bubble chamber must be enhanced [66].

1.15. Decision errors

Hypothesis testing is not without flaws [67]. According to the online glossary, "Decisions Errors refer to the probability of making the wrong conclusion when doing hypothesis testing" [68]. Consider the legal system: innocent people are occasionally wrongfully condemned, and the guilty are sometimes let go. Similarly, data might lead to incorrect conclusions. What separates statistical hypothesis tests from a court system, however, is that the framework allows for measurement and regulates how frequently the evidence leads to an erroneous conclusion. There are two competing hypotheses in a hypothesis test: the null and the alternative.

Table 6. Four different scenarios for hypothesis tests [67]

Truth	**Test conclusion**	
	Reject null hypothesis	Fail to reject the null hypothesis
The null hypothesis is true	Type 1 Error	Good decision
An alternative hypothesis is true	Good decision	Type 2 Error

At the end of a hypothesis test, the researcher declares whether the null hypothesis is true or false (leaving the alternative hypothesis as the only other option), but he may choose incorrectly. Table 6 shows the four probable outcomes of a hypothesis test [67]. Based on Çetinkaya-Rundel and Hardin's (2021) work: "A Type 1 Error is rejecting the null hypothesis when H_0 is actually true. <…> A Type 2 Error is failing to reject the null hypothesis when the alternative (H_A) is actually true" [67].

1.16. Data compression and digital image file types

Compressing data is a method of reducing data size without losing information. Data compression methods are divided into two types: lossy and lossless compression [69]. "The main difference between the two compression techniques is that the lossy compression technique does not restore the data in its original form, after decompression; on the other hand, lossless compression restores and rebuilt the data in its original form, after decompression" [69].

To keep file sizes as minimal as possible, lossy compression discards as much data as possible. This is accomplished by focusing on data that are regarded as less obvious, such that the file itself retains a high degree of similarity to the original. The lower the quality of a file, the more compressed it is [70]. The most common lossy compression image type is JPG, and lossless are PNG and DICOM, which are used in hospitals.

JPG files are raster[2] images stored in the JPEG (Joint Photographic Experts Group) format, which is widely used to save digital images and graphics made by image-editing software. JPEG employs lossy compression to reduce image size while maintaining image quality, and it can handle up to 256^3=16 777 216 colours. The compression mechanism of the format removes some data from the original image to reduce the overall file size and make it more easily transmissible, which is particularly important on the Web. Although the removal of the picture data lowers overall image quality, the difference is usually undetectable [71].

A *PNG* (Portable Network Graphics) file is a lossless compression raster image file format. According to file format information: "The PNG file format offers lossless image compression making it popular among its users. PNG has grown into one of the most extensively used image file formats over time" [73].

Based on file info: "A DICOM file is an image saved in the Digital Imaging and Communications in Medicine (DICOM) format" [74], which using lossless compression [75]. It includes a clinical scan image, such as an ultrasound or magnetic resonance imaging. DICOM documents can also include patient personal data, allowing an image to be connected to a specific individual [74].

All current imaging tools, accessories, web servers, workstations, printers, and picture archiving and communication systems (PACS) from diverse vendors may use the DICOM standard. This communication standard has achieved extensive adoption among radiography equipment manufacturers over the years due to its ease of integration and ongoing expansion. DICOM image files that conform to DICOM Part 10 are known as "DICOM Format Files" or "DICOM Files" and are recognised by the extension ".dcm" [76].

1.17. The programs are used to calculate similarity characteristics

This section will present two non-commercial, open-source programs for calculating various image similarity characteristics – the DSCImageCalc and EvaluateSegmentation software.

According to Lawton (2017), the DSCImageCalc software was: "designed to calculate similarity coefficients for different segmentations of the same image, to analyse the performance of segmentation algorithms or human ratters" [61]. The program was developed for research of human ratter segmentation of the brachial plexus cross-section on an ultrasound image to compute similarity coefficients. Colour is used to denote segments; the use of assorted colours allows for the definition of several segments in a single image. The software offers a graphical user interface (GUI) that allows to choose files, coefficient types, and segment colours, as well as view results. Photos are replaced with two-colour images; anything not included in the study segment under study is obscured, and diagnostic information is presented as a percentage of the segment's pixels and image percentage [61].

Based on Taha and Hanbury's (2015) work: "EvaluateSegmentation is a tool that compares two segmentations of volumes using 22 different metrics. These metrics were selected as a result of comprehensive research into the metrics used for evaluating medical volume segmentations" [62]. It

[2] "**Raster graphics**, also called **bitmap graphics**, are a type of digital image that uses tiny rectangular pixels, or picture elements, arranged in a grid formation to represent an image" [72]

was created to compare whole-body volume segments and is meant to be efficient and interchangeable.

1.18. Justification and objectives of the master's thesis

Summarising the literature review of the master's thesis, it can be stated that breast cancer is one of the leading causes of death in women. A variety of cancer diagnoses and treatments possibilities have been developed, the choice of which depends on the stage of the patient's disease. The volumes of treatment and their importance in the planning process, as well as the recommendations of ESTRO, according to which these volumes are obtained, were introduced. Dose limits for breast cancer were demonstrated, different dose fractionation options and the concept of DVH were introduced, as well as computed tomography, image segmentation, threshold value concepts, types of decision errors, image compression types, and similarity characteristics calculation programs.

It has been observed that in the medical environment, image analysis is performed mainly with the brain data using only MRI images, and CT images are rarely used. It is expected that the results of the similarity of breast cancer structures obtained during the final project will contribute to a faster image analysis using CT data and will be the first step to the usage of artificial intelligence (AI).

Not all commercial programs have the ability to calculate a *DICE* similarity coefficient, e.g., Elekta "Monaco" does not have this feature and in Varian "Eclipse" program is available only in the latest version. Open-source software "EvaluateSegmentation" would be a useful tool for other institutions to evaluate the similarity of images if the effectiveness of this program will be demonstrated during this master thesis.

This master's thesis is the first step toward the use of artificial intelligence in daily clinical practice at LSMU Kaunas clinics. In the future, the work is expected to be used for semi-contouring or auto-contouring assessment. For geometric similarity, not only the *DICE* similarity coefficient but also Hausdorff distance would be used. Artificial Intelligent created plans are a new future. Contour delineation, a crucial process in radiation oncology, is time-consuming and inaccurate due to inter-observer variation has been a critical issue in this process. An atlas-based automatic segmentation would improve the delineation efficiency and reduce inter-observer variation. But putting it to use requires extra work to create a database that uses artificial intelligence to contour and plan.

2. Materials and methods

In this section of the master's thesis, information about the left breast cancer patient without lymph nodes, target, and organs at risk delineation on CT images performed by different radiation-oncologists in LSMU Kaunas clinics, preparation of CT images for measurements, investigated clinical volumes, "EvaluateSegmentation" software, and development of treatment plan with treatment planning system (TPS) "Eclipse", is presented.

2.1. Information about the left breast cancer patient without lymph nodes and practical task in LSMU Kaunas Clinics

Dr Laimonas Jaruševičius, Head of the Radiation Therapy Department, Clinic of Oncology and Haematology, Kaunas Clinics, Lithuanian University of Health Sciences, autumn of 2021, prepared a practical task in the Hospital of Lithuanian University of Health Sciences Kaunas Clinics, which was done by 15 radiation-oncologists. They were analysing delineation of a breast cancer patient without lymph nodes case. A patient with a breast infiltrative ductal carcinoma (high-grade nuclear polymorphism in situ component) was examined. The patient underwent all the cancer detection methods listed in the literature – ultrasound, mammogram, magnetic resonance imaging, and biopsy until confirmation of cancer diagnosis. During this task, the treatment volumes (*CTV_WB*[3], *PTV_WB*, *PTV_WB_dvh*), critical organs (*Heart*, *Lung_ipsilat*, *Breast_contralat*[4], *Spinal_cord*) and other structures (*Body, Bones)* were drawn by the doctors and only treatment volumes and part of critical organs (*Heart, Lung_ipsilat*, and *Spinal_cord*) are examined in this work. The data used were depersonalised during the competition; therefore, the recommendations of the Lithuanian Bioethics Committee's panel "On the observance of ethical principles in non-biomedical research, the object of which is human health" [77] are not violated.

2.2. General Electric medical system LightSpeed RT16 CT scanner

General Electric (GE) medical system LightSpeed RT16 CT scanner was used to scan the patient. CT scanner is located in the Hospital of Lithuanian University of Health Sciences Kaunas Clinics, Radiotherapy department.

According to GE Healthcare: "The CT Scanner System is composed of a gantry, patient table, operator console, power distribution unit (PDU), and interconnecting cables. The system includes image acquisition hardware, image acquisition and reconstruction software, and associated accessories" [79]. Figure 16 shows the GE LightSpeed RT16 CT scanner.

Fig. 16. CT scanner GE LightSpeed RT16 [80]

Based on Medallion Medical Technologies: "The CT scanner has been designed with LightSpeed technology that provides thin, high 2D and 3D resolution and high-quality images" [81]. The gantry may revolve at up to 0.5 s each rotation and take 16

[3] **WB** – whole breast

[4] **Contralateral** – "Occurring on or acting in conjunction with a part on the opposite side of the body" [78]

data slices in the axial direction, reaching a maximum of 20 mm. Based on GE Healthcare: “The system can be operated in Axial, Cine, Helical, Fluoro, and Gated acquisition modes” [79].

The CT scanner parameters during the scanning process of the left breast cancer patient without lymph nodes were as follows: X-ray tube voltage – 120 kV; X-ray tube current – 120 mA; slice thickness – 1.25 mm; image size – 512 × 512 px. The patient was scanned in the supine position. 110 cross-sectional images of the patient were acquired in the helical scanning mode; only the 67th image was used in this work.

2.3. Preparation of clinical images of investigated treatment volumes

The treatment volumes delineated during the practical task were presented using the Varian company treatment planning system (TPS) “Eclipse” (see Figure 17) in DICOM format. Screenshotted images (see Figure 19 a) saved in .png format were created using the Snipping Tool in the Windows operating system (Windows 10 Pro 64-bit).

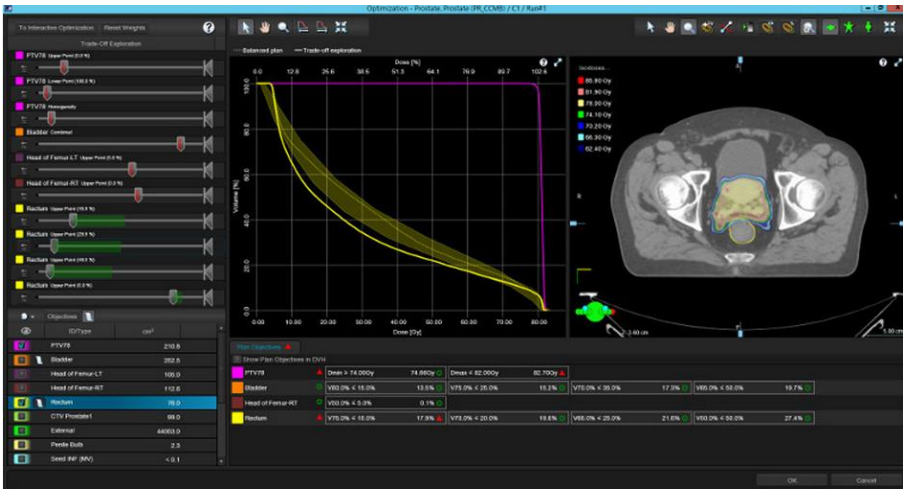

Fig. 17. Varian “Eclipse” program window screenshot [82]

Screenshotted images were cropped to fit the original DICOM image size of 512 × 512 px using the online tool “Crop IMAGE” [83] (see Figure 18 and Figure 19 b). On this webpage .jpg, .png, and .gif format images can be cropped. Width and height were selected at 512 px; the position of X was between 252-254 px; the position of Y was between 190-208. The variation in values is due to the varying initial size of the photos. The correct X and Y coordinate points were checked, creating a series of images starting from the reference photo.

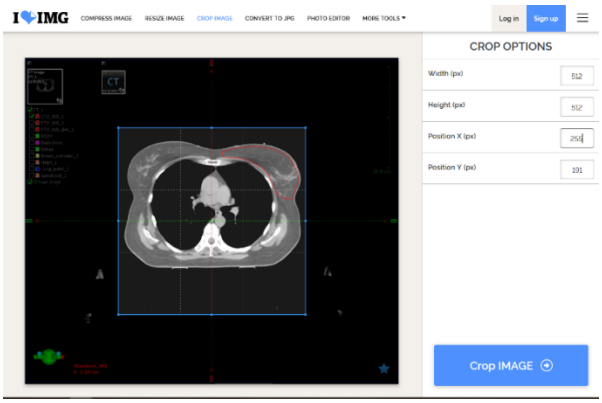

Fig. 18. Webpage Crop IMAGE window screenshot [83]

The Magic Wand Tool in "Adobe Photoshop 2020" performed an image contouring (edge detection) process to make *CTV_WB* and *PTV_WB* volume definition boundaries into solid one colour areas (see Figure 19 c). The red colour (255 0 0 in RGB colour scheme) for contouring was used. According to Photoshop essentials: "The Magic Wand Tool <…> is one of the oldest selection tools in Photoshop. Unlike other selection tools that select pixels in an image based on shapes or by detecting object edges, the Magic Wand selects pixels based on tone and colour" [84].

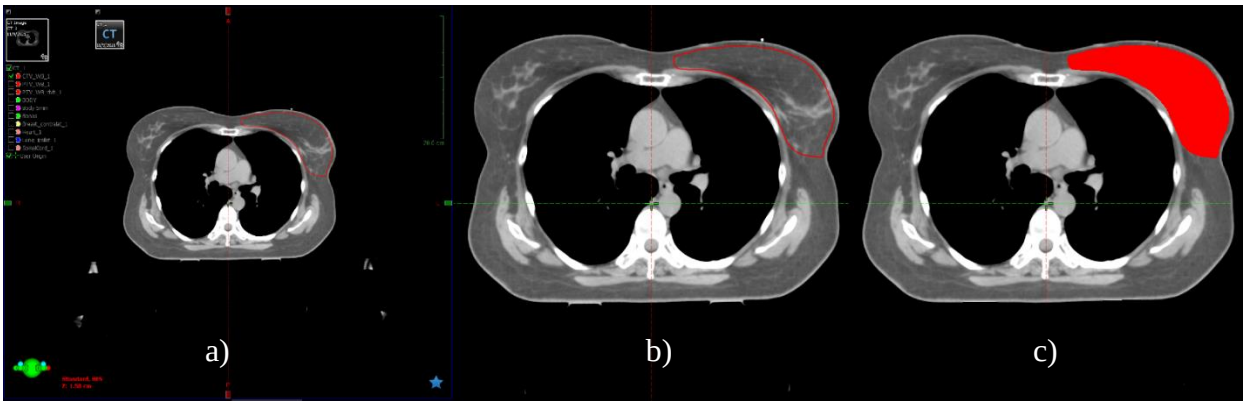

Fig. 19. Image preparation process: a) Screenshotted image from "Eclipse" program; b) cropped image with "Crop IMAGE" webpage; c) contoured image with "Adobe Photoshop 2020" program. All images are shown from the z-direction

Simplified work scheme for the master's final degree project is presented in Appendix 1.

2.3.1. Investigated target volumes

Two different target volumes were investigated in this work – *CTV_WB* (obtained by adding a 0.5 cm margin to the *GTV_WB*), *PTV_WB* (obtained by adding a 0.4-1.0 cm margin to the *CTV_WB*), and *PTV_WB_dvh* (the structure was obtained by cutting 0.5 cm from the body surface and 0.5 cm from the chest/lungs) is shown, which is created to evaluate target coverage for the planned treatment plan. All different investigated target volumes are shown in Figure 20.

The used reference plan is developed by dr. Laimonas Jaruševičius and dr. Evelina Koleibnikova, based on ESTRO guidelines. This plan is used as a reference and the results obtained are compared with this plan.

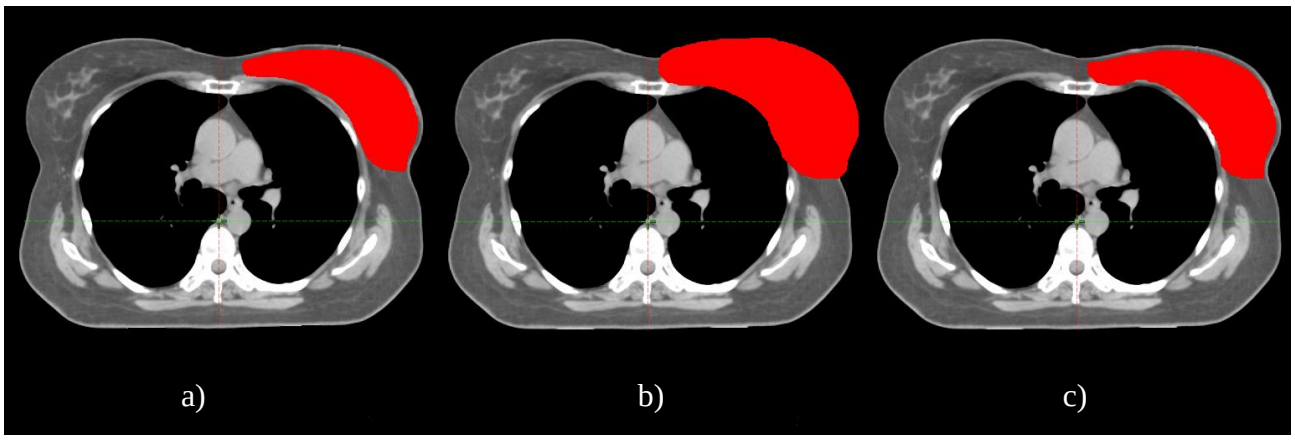

Fig. 20. Different treatment volumes: a) *CTV_WB*; b) *PTV_WB*; c) *PTV_WB_dvh*

All similarity calculations with "EvaluateSegmentation" software were done for images obtained in z-direction, other directions (x and y) were shown in the results section only for visualisation purposes. Beside the target volumes analysis, also were analysed and organs at risk (OARs).

2.4. "EvaluateSegmentation" software

The VISCERAL (Visual Concept Extraction Challenge in Radiology) team developed the software. The "EvaluateSegmentation" [85] utility compares two-volume segments using 22 distinct factors. These metrics were chosen following a thorough examination of the metrics used to estimate medical volume segments [86]. According to VISCERAL, "It is specifically optimised to be efficient and scalable, and hence can be used to compare segmentations on full-body volumes" [86]. The program is written in C++ language and is a command-line[5] gadget. Based on Taha and Hanbury's (2015) publication: "The command line has a mandatory part specifying the two images being compared and an optional path with arguments used to control the metric calculation. The command line has the following syntax: EvaluateSegmentation ground-truth path, segmentation path *[-thd threshold] [-use DICE,JAC,HD,...] [-xml xmlpath]*" [62]. Unless other criteria are supplied utilising ambiguous comparisons, the image's binary is compared by default by lowering to the specified threshold if a picture threshold *-thd* is set. All parameters are evaluated if *-use* defines the number of metrics to analyse [62]. An overview of metrics, which can be used in "EvaluateSegmentation" software, is presented in Table 7.

Table 7. Overview of the metrics available in the program [62, 88]

Criteria	Symbol	Category	Fuzzy
Dice Coefficient	DICE	Spatial overlap-based	yes
Jaccard Coefficient	JAC	Spatial overlap-based	yes
True-positive rate (Sensitivity, recall)	TPR	Spatial overlap-based	yes
True-negative rate (Specificity)	TNR	Spatial overlap-based	yes
False-positive rate (Fallout)	FPR	Spatial overlap-based	yes
False-negative rate (Sensitivity)	FNR	Spatial overlap-based	yes
F-Measure	FMS	Spatial overlap-based	yes
Global Consistency Error	GCE	Spatial overlap based	no
Volumetric Similarity Coefficient	VS	Volume-based	yes
Rand Index	RI	Pair counting-based	yes
Adjusted Rand Index	ARI	Pair counting-based	yes
Mutual Information	MI	Information theoretic-based	yes
Variation of Information	VOI	Information theoretic-based	yes
Interclass correlation	ICC	Probabilistic-based	no
Probabilistic Distance	PBD	Probabilistic-based	yes
Cohen Kappa	KAP	Probabilistic-based	yes
The area under ROC Curve	AUC	Probabilistic-based	yes
Hausdorff distance	HD	Spatial distance-based	no
Average distance	AVD	Spatial distance-based	no
Mahalanobis Distance	MHD	Spatial distance-based	no

[5] **Command-line interface (CLI)** – "A text-based user interface (UI) used to run programs, manage computer files, and interact with the compute" [87]

The six categories are available depending on the link between the properties of the measurements and their definitions:

- "*Spatial overlap-based (Category 1).* These are metrics defined based on the spatial overlap between the two segmentations being compared, namely the four basic overlap cardinalities – true positives (TP), true negatives (TN), false positives (FP) and false negatives (FN)" [88].
- "*Volume-based (Category 2).* Metrics from this category are based on comparing the volume of the segmented region, i.e., they aim to measure the number of voxels segmented compared with the number of voxels in the true segmentation" [88].
- "*Pair counting-based (Category 3).* Metrics from this category are based on $\binom{n}{2}$ tuples[6] that represent all possible voxel pairs in the image" [88].
- "*Information theoretic-based (Category 4).* Metrics of this category are based on basic values of information theory such as entropy and mutual information" [88].
- "*Probabilistic based (Category 5).* These metrics consider the segmentations being compared as two distributions. Under this consideration, the metrics are defined based on the classic comparison methods of statistics of these distributions" [88].
- "*Spatial distance-based (Category 6).* These metrics aim to summarise distances between all pairs of voxels in the two segmentations being compared, i.e., they provide a one-value measure that represents all pairwise distances" [88].

2.4.1. Spatial overlap-based metrics

Sørensen-Dice coefficients (DICEs) are the most commonly used measurement method for validating medical volume segmentation [62]. The name *DICE* was already in use in the 1890s by Sir Francis Galton in his publication "Dice for Statistical Experiments" [90], but it is now known definition was developed by Sørensen-Dice in the 1950s. Based on Zou et al. (2004) work: "The value of a *DICE* ranges from 0, indicating no spatial overlap between two sets of binary segmentation results, to 1, indicating complete overlap" [91]. In addition to directly comparing the automatic and ground truth segments, *DICE* is often used to evaluate repeatability (replication). The Sørensen-Dice coefficient is defined by this formula:

$$DICE = \frac{2TP}{2TP+FP+FN} \tag{5}$$

also, it can be calculated using the *JAC*, which will be explained later:

$$DICE = \frac{2JAC}{1+JAC} \tag{6}$$

Concerning Taha and Hanbury's (2015) publication: "The Jaccard index (*JAC*) between two sets is defined as the intersection between them divided by their union" [62]. *JAC* is defined by the formula:

$$JAC = \frac{TP}{TP+FP+FN} = \frac{DICE}{2-DICE} \tag{7}$$

[6] **Tuple** – "A generalization of ordered pairs, such as (-3, 4), and ordered triples, such as (0, -3, 5), in any dimension. An n-tuple is an ordered list of n numbers and can represent a point in n-dimensional space" [89]

Like the Sørensen-Dice coefficient, the Jaccard index values vary in the range [0, 1]. These two coefficients show the same statistical aspects and do not provide any new additional information [62].

TPR is a metric that measures the percentage of positive voxels in the ground truth that are also labelled as positive by the segmentation in the issue. *TNR*, also known as Specificity or Similarly, evaluates how many negative voxels (background) in the ground truth segmentation are also recognised as negative by the classification in the issue. These two metrics are not often employed as assessment measures in clinical image segmentation because of their sensitivity to segment size [62]. They are stated as:

$$Sensitivity = Recall = TPR = \frac{TP}{TP+FN} \tag{8}$$

$$Specificity = TNR = \frac{TN}{TN+FN} \tag{9}$$

Two further measures, the FPR and the FNR [62], are linked to these measurements. Formulas used to define them are:

$$Fallout = FPR = \frac{FP}{FP+TN} = 1 - TNR \tag{10}$$

$$FNR = \frac{FN}{FN+TP} = 1 - TPR \tag{11}$$

Equations 10 and 11's equivalence means that one of the two possible measures should be approved, not both, i.e., FPR or TNR and corresponding FNR or TNR. Another related metric is PPV, which is used to construct the F-measure. It is not typically used to assess medical data but is used to compute the F-measure [62]. The formula is as follows:

$$Precision = PPV = \frac{TP}{TP+FP} \tag{12}$$

F_β-Measure is an agreement between *PPV* and TPR. F_β-Measure is defined by the formula:

$$FMS_\beta = \frac{(\beta^2+1)\cdot PPV \cdot TPR}{\beta^2 \cdot PPV + TPR} \tag{13}$$

When β = 1.0, it means that *TPR* and *PPV* are both essential, it is an example of F-Measure. The harmonic mean, often known as F-Measure, is defined by the formula:

$$FMS = \frac{2PPV+TPR}{PPV+TPR} \tag{14}$$

As stated by Taha and Hanbury's (2015) publication: "The *FMS* is mathematically equivalent to *DICE*; this follows from a trivial substitution for *TPR* and PPV" [62].

GCEs are faults that occur when several segmentation methods are not aligned. It is expressed by the formula [62]:

$$GCE = \frac{1}{n} min\left[\frac{FN(FN+2TP)}{TP+FN} + \frac{FP(FP+2TN)}{TN+FP} + \frac{FP(FP+2TP)}{TP+FP} + \frac{FN(FN+2TN)}{TN+FN}\right] \tag{15}$$

where: *n* in this formula is several observations [62].

2.4.2. Volume-based metric

As described by Taha and Hanbury's (2015) publication: "The name implies, volumetric similarity (*VS*) is a measure that considers the volumes of the segments to indicate similarity. The Volumetric Similarity (*VS*) is defined as 1 – *VD*, where *VD* is the volumetric distance" [62]. That is defined by the formula:

$$VS = 1 - \frac{|FN-FP|}{2TP+FP+FN} \tag{16}$$

VS is not considered an overlap-based measure because it is defined using the four cardinalities, [62] since based on Taha and Hanbury's (2015) publication: "The absolute volume of the segmented region in one segmentation is compared with the corresponding volume in the other segmentation. This means that the overlap between the segments is absolutely not considered" [62].

2.4.3. Pair counting-based metrics

As mentioned in Taha and Hanbury's (2015) work: "In this section, pair-counting measures, such as the Rand index and its expansions, are defined. The four main pair-counting cardinalities, namely *a*, *b*, *c*, and *d* for crisp and fuzzy segmentation, will be specified first, followed by the metrics based on these cardinalities" [62]. These cardinalities are defined below:

$$a = \frac{1}{2}[TP(TP-1) + FP(FP-1) + TN(TN-1) + FN(FN-1)] \tag{17}$$

$$b = \frac{1}{2}[(TP+FN)^2 + (TN+FP)^2 - (TP^2 + TN^2 + FP^2 + FN^2)] \tag{18}$$

$$c = \frac{1}{2}[(TP+FP)^2 + (TN+FN)^2 - (TP^2 + TN^2 + FP^2 + FN^2)] \tag{19}$$

$$d = \frac{n(n-1)}{2} - (a+b+c) \tag{20}$$

The *RI* is a measure of clustering similarity. One of its key characteristics is that it is not label-based, therefore. It can be used for assessing both clustering and classifications. *RI* is defined by the formula:

$$RI = \frac{a+b}{a+b+c+d} \tag{21}$$

where *a*, *b*, *c*, and *d* are the cardinalities defined in Equations 17–20.

Concerning Taha and Hanbury's (2015) work: "The Adjusted Rand Index (*ARI*) is a modification of the Rand Index that considers a correction for chance" [62]. The *ARI* can be defined by using four cardinalities:

$$ARI = \frac{2(ad-bc)}{c^2+b^2+2ad+(a+d)(c+b)} \tag{22}$$

2.4.4. Information theoretic-based metrics

The *MI* among parameters indicates how much one variable has information about the other. Or, to put it another way, the lowering in the uncertainty of one parameter when the other is known. The MI is equivalent to the mixed entropy $H(S_1, S_2)$, and the border entropy $H(S)$ of pictures is specified as [62]:

$$H(S) = -\sum_i p(S^i) \log p(S^i) \tag{23}$$

$$H(S_1, S_2) = -\sum_{ij} p(S^i, S^j) \log p(S^i, S^j) \tag{24}$$

as stated by Taha and Hanbury's (2015) work: "Where $p(x, y)$ is a joint probability, S^i are the regions (segments) in the image segmentation, and $p(S^i)$ are the probabilities of these regions that can be expressed in terms of the four cardinalities *TP*, *FP*, *TN*, and *FN*, which are calculated for the fuzzy segmentation (S_g and S_t)" as follows [62]:

$$p(S_g^1) = (TP + FN)/n \tag{25}$$

$$p(S_g^1) = (TN + FN)/n \tag{26}$$

$$p(S_t^1) = (TP + FP)/n \tag{27}$$

$$p(S_t^1) = (TN + FP)/n \tag{28}$$

where $n=TP+FP+TN+FN$ stands for the total number of voxels, S_g stands for ground truth segments, and S_t stands for test segmentation. Because *TN*, *TP*, *FN*, and *FP* are cardinalities of disconnected sets that split the volume by nature, the joint probability might be changed as follows [62]:

$$p(S_1^1, S_2^1) = \frac{TP}{n} \tag{29}$$

$$p(S_1^1, S_2^2) = \frac{FN}{n} \tag{30}$$

$$p(S_1^2, S_2^1) = \frac{FP}{n} \tag{31}$$

$$p(S_1^2, S_2^2) = \frac{TN}{n} \tag{32}$$

The *MI* is therefore defined as follows:

$$MI(S_g, S_t) = H(S_g) + H(S_t,) - H(S_t, S_g) \tag{33}$$

The *VOI* is a measure of the quantity of data lost (or gained) while switching from one variable to another. The *VOI* is calculated using entropy and mutual information and is defined as [62]:

$$VOI(S_g, S_t) = H(S_g) + H(S_t,) - 2MI(S_t, S_g) \tag{34}$$

2.4.5. Probabilistic-based metrics

The *ICC* is a measurement of relationships among observed values that do not have to be ordered or clearly labelled. Between analysts, the *ICC* is commonly used as a measure of conformity. *ICC* is defined as follows [62]:

$$ICC = \frac{\sigma_S^2}{\sigma_S^2 + \sigma_\epsilon^2} \tag{35}$$

where σ_S indicates variance caused by variations between the segmentations and σ_ϵ stands for variance caused by variations among the points in the segmentations [62].

According to Taha and Hanbury's (2015) work: "The Probabilistic Distance (*PBD*) is a measure of distance between fuzzy segmentation. Given two fuzzy segments, *A* and *B*" [62]. *PBD* is defined as follows:

$$PBD(A,B) = \frac{\int |P_A - P_B|}{2 \int P_{AB}} \tag{36}$$

where P_A and P_B are the segmentation likelihood probabilities, and P_{AB} is their joint distribution function [62].

The *KAP* is an indicator of population consistency. *KAP* has a benefit over other metrics in that it considers consensus produced by chance, making it more robust. *KAP* is represented as [62]:

$$KAP = \frac{P_a - P_c}{1 - P_c} \tag{37}$$

where P_a is the sample consistency and P_c is the hypothetical likelihood of random consistency. To simplify the calculation, the same may be represented in terms of frequency [62]. It is defined as:

$$KAP = \frac{f_a - f_c}{N - f_c} \tag{38}$$

where *N* stands for the number of measurements. The variables in Equation 38 can be written in terms of the four cardinalities that overlap – *TP*, *TN*, *FN*, and *FP* [62]. f_a and f_c are expressed as:

$$f_a = TP + TN \tag{39}$$

$$f_c = \frac{(TN+FN)(TN+FP)+(FP+TP)(FN+TP)}{N} \tag{40}$$

The plot of the *TPR* against the *FPR* is known as the *ROC* curve. In medical diagnostics, the *AUC* is a measure of accuracy. The *ROC* curve, which is a plot of *TPR* vs *FPR*, usually implies many measurements. The size of the trapezoid is specified by the measurement point, and the lines *TPR = 0* and *FPR = 1* in the scenario when a test segmentation is evaluated to a ground truth segmentation (one measurement) [62]. The *ROC* is defined as:

$$AUC = 1 - \frac{FPR+FNR}{2} = 1 - \frac{1}{2}\left(\frac{FP}{FP+TN} + \frac{FN}{FN+TP}\right) \tag{41}$$

2.4.6. Spatial distance-based metrics

As dissimilarity indicators, spatial distance-based metrics are commonly used in picture segmentation analysis. They are advised when the total precision of the segmentation, such as the border outline (contour), is important. In this part, three distance metrics will be presented: the Hausdorff distance (*HD*), the Average distance (*AVD*), and the Mahalanobis distance (*MHD*) [62].

The *HD* is the largest range from the picture pixel to the closest edge pixel. In general, *HD* is sensitive to outliers. Since noise and abnormalities are widespread in clinical segmentations, using *HD* directly is not suggested [62].

The *AVD*, also known as the *HD*, is the *HD* averaged across all locations. The *AVD* is more dependable and less susceptible to anomalies than the *HD* [62].

The *MHD* is the number of common errors from the average distribution that an observation deviates from [62].

2.5. The Halcyon™ (V3.1) treatment system

The Halcyon™ system is a completely new cancer therapy technology. Halcyon™ is a clinical workflow revolutioniser that simplifies and improves practically every aspect of IMRT/VMAT radiation. This innovative treatment approach aims to provide access to high-quality cancer care around the world and save the lives of millions of cancer patients [92]. The Halcyon™ treatment machine is shown in Figure 21.

Halcyon™ is a stationary 6 MV-FFF beam linear accelerator in a ring configuration with a carbon fibre bore positioned opposite a beam stopper. There is no usage of a bending magnet. Halcyon beam is shaped by stacked and staggered dual-layer separately operating latest generation multi-leaf collimators (MLCs). MLC's design allows for more effective treatment and less interleaf leaking. The distal and proximal MLC banks are spaced by 0.5 cm from each other, and every leaf is 1.0 cm in length extended at the isocenter. As a result, at the isocenter, the effective resolution of leaf length is 0.5 cm. There are 29 couples of leaves in the proximal layer and 28 couples in the distal layer. Halcyon MLCs have a top speed of 5 cm/s. The distance between the external laser centre and the actual radiation isocenter is constant. This shift can be validated using the Machine Performance Check (MPC), which is required to be completed daily before any procedure [94].

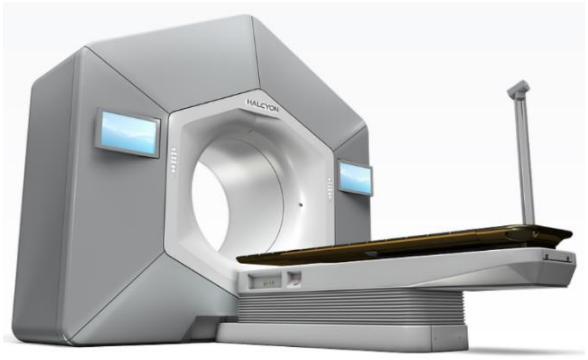

Fig. 21. The Halcyon™ treatment system [93]

Halcyon™ treatment system key features:

- "Fast – beam-on time could be as fast as 1 minute plus" [95];
- "Accurate – the unique design of a dual-layer multi-leaf collimator (MLC) enables accurate radiation dose delivery to the tumour" [95];
- "Reduces unwanted radiation dose – the reduction in interleaf leakage helps to reduce unwanted radiation dose to critical structures, thus, minimising side effects" [95];
- "Alleviates anxiety – a quick and quiet treatment helps to reduce anxiety in patients" [95];
- "Maximises comfort – a spacious 100 cm diameter bore with integrated ambient lighting puts claustrophobic patients at ease. The couch descends low to the ground for easy loading and unloading of the patient" [95];
- "Improved safety – the integrated couch-mounted camera travels with the patient, enabling the radiographer to monitor the patient during the treatment" [95].

2.6. Planning process with treatment planning system "Eclipse"

Varian's "Eclipse" software optimises a radiation therapy treatment plan depending on a physician's dose recommendations and details regarding the size, shape, and location of cancer to be cured with

irradiation. It is used in over 3400 cancer treatment facilities across the world. The treatment plan serves as the foundation for electronic instructions that tell the radiation equipment how to give the treatment: which angles to employ, how much dose to give from every angle, and how to bend the treatment beam to fit the form of cancer [96].

Eclipse software includes planning guidelines and simple optimisation devices that make complex treatments for cancer like IMRT, IGRT, and RapidArc® radiotherapy easier and faster to prepare. It provides therapists with a collection of treatment plan models that make generating a customised plan for the patient much more accessible [96].

The main parameters used in the planning process are given in Table 8, and the arrangement of the fields is shown in Figure 22.

Table 8. Main parameters in the planning process

Field number	Gantry rotation, °	x, cm	y, cm	z, cm	Calculated SSD, cm	MU, a. u.	Dose per fraction, Gy	Number of fractions	Total dose, Gy	Treatment percentage, %
1	300	10.97	-10.60	1.51	91.7	447.6	5.2	5	26.0	100
2	330				94.6	286.5				
3	0				95.6	357.9				
4	30				95.6	387.5				
5	60				94.9	296.6				
6	90				93.9	319.6				
7	120				92.6	471.1				

Table 8 shows that only three values change in the planning process – gantry rotation, SSD distance and monitor unit value.

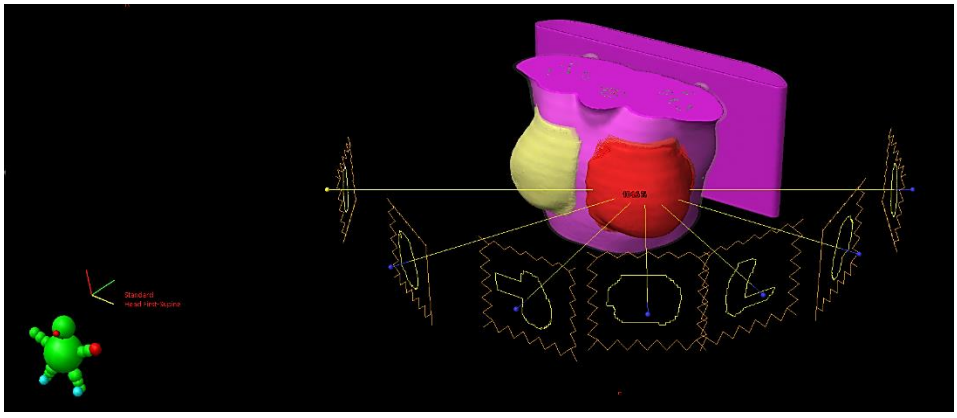

Fig. 22. The arrangement of the fields in the planning process

It can be seen from Figure 22 that the fields are arranged from the left edge of the left breast clockwise to the right edge of the left breast. The angles used change from 120° to 300° counterclockwise every 30°.

3. Results

This chapter examines and analyses the main results related to the volumes of the studied structures (*CTV_WB, PTV_WB, PTV_WB_dvh, Heart, Lung_ipsilat* and *Spinal_cord*) obtained by the treatment planning system "Eclipse", the similarity characteristics of the structures (*CTV_WB* and *PTV_WB*) received in the treatment planning system "Eclipse", and "EvaluateSegmentation" software and the influence of different structure volumes on the resulting treatment plan and its outcome in evaluating DVH curves and dose constraints are analysed.

3.1. Volume analysis of treatment volumes and critical organs

At the beginning of the work, the information on radiotherapy developed by the participating radiation-oncologists in the "Eclipse" treatment planning system was systematised in Table 9.

Table 9. Primary information about treatment plans from the treatment planning system "Eclipse"

Plan name in the system	Site	Fractions	Prescription template	Imaging frequency	Gating	Margin, cm
zzBreast_WB_ref	Breast, Left	5	Breast_26Gy/5fr	Every treatment	DIBH	0.5
zzBreast_WB_1	Bronchus, Left	5	Breast_26Gy/5fr	Every treatment	DIBH	1.0
zzBreast_WB_2	Breast, Left	5	Breast_26Gy/5fr	Every treatment	DIBH	0.5
zzBreast_WB_3	Bronchus, Left	5	Breast_26Gy/5fr	Every treatment	DIBH	0.4
zzBreast_WB_4	Breast, Left	5	Custom	Not-specified	DIBH	0.4
zzBreast_WB_5	Breast, Left	5	Breast_26Gy/5fr	Every treatment	-	0.7
zzBreast_WB_6	Breast, Left	5	Breast_26Gy/5fr	Every treatment	-	0.5
zzBreast_WB_7	Breast, Left	5	Custom	Every treatment	DIBH	0.5
zzBreast_WB_8	Breast, Left	5	Custom	Every treatment	DIBH	0.5
zzBreast_WB_9	Breast, Left	5	Breast_26Gy/5fr	Every treatment	-	0.5
zzBreast_WB_10	Breast, Left	5	Breast_26Gy/5fr	Every treatment	-	0.5
zzBreast_WB_11	Breast, Left	5	Breast_26Gy/5fr	Every treatment	DIBH	0.5
zzBreast_WB_12	Breast, Left	5	Breast_26Gy/5fr	Every treatment	DIBH	0.5
zzBreast_WB_13	Breast, Left	5	Custom	Every treatment	DIBH	0.5
zzBreast_WB_14	Breast, Left	5	Breast_26Gy/5fr	Every treatment	DIBH	0.5
zzBreast_WB_15	Breast, Left	5	Breast_26Gy/5fr	Every treatment	DIBH	0.5

Table 9 shows that 13 radiation-oncologists chose the left side of the breast, and 2 medics chose the left side bronchi according to what treatment should be modelled. In all cases, radiotherapy was chosen, which is performed in 5 fractions, irradiating the entire breast with a dose of 26 Gy. This dose choice corresponds to a type of fractionation called hypofractionation. According to the Murray Brunta et al. (2020) trial study: "The 26 Gy dose level is similar to 40 Gy in 15 fractions in terms of patient-assessed normal tissue effects, clinician-assessed normal tissue effects, and photographic change in breast appearance, and is similar to normal tissue effects expected after 46–48 Gy in 2 Gy fractions" [97]. It is also seen from Table 9 that 14 radiation-oncologists selected the frequency of imaging daily before each treatment and only one physician as optional. 11 radiation-oncologists

chose to use the deep inspiration breath-hold (DIBH) system, and 4 decided not to use it, also 11 radiation-oncologists chose margin as 0.5 cm, 2 as 0.4 cm and 1 as 1.0 cm and 0.7 cm.

Yoshimura et al. (2021) state that the optimal *CTV-PTV* margin for the DIBH system, calculated according to the van Herk margin formula [98], should be 6-8 mm [99], but it should be borne in mind that concerning Carmen et al. (2018) publication: "A 3 mm threshold of DIBH position uncertainty is usually applied in the surface tracking systems" [100]. Using IGRT technology, the CTV margin is 10-15 mm, and the PTV is 3-5 mm [101]. Based on Hlavka et al. (2018): "The PTV margin for daily online verification of the marker position in the breast" [103] applying IGRT technology is calculated using three components "intrafraction movement (*IF*), interobserver differences in setup correction (*IO*) and respiratory induced movement (*RM*) of the markers during free breathing. <…> The resulting margins in anteroposterior, craniocaudal and laterolateral directions were 4.7, 5.1, and 5.9 mm, respectively" [103].

After the systematisation of treatment information, it will be shown how the different structures (*CTV_WB, PTV_WB, PTV_WB_dvh, Heart, Lung_ipsilat* and *Spinal_cord*) delineated by the medics look on the *x, y,* and *z* axes (the coordinate of the images used is – *x =10.97 cm, y =-10.60 cm, z =1.51 cm*), these images are shown in Appendices 2-7. Later on, only z-axis images will be investigated.

It can be seen from Appendix 2 that the structures of *CTV_WB* drawn by the participating radiation-oncologists differ significantly from each other. The light green line shows the reference structure drawn by dr. Laimonas Jaruševičius and dr. Evelina Koleibnikova, according to ESTRO recommendations. Only a few structures are smaller than the reference size, while others are significantly larger, suggesting that the patient will receive a higher dose during radiotherapy treatment than would be required simply because the structure size is larger than the reference size. It can be seen from Appendix 3 the difference between the *PTV_WB* structures and the reference (light blue colour) structure is also different. In this case, the edges of the *PTV_WB* structure (left and right) are stiffer than in the case of *CTV_WB* (see Appendix 2). As in the case *of CTV_WB* (see Appendix 2), most of the structures are larger than the reference structure drawn according to the ESTRO recommendations. The difference between the *PTV_WB_dvh* structures and the reference (dark blue colour) structure is likewise distinct, as seen in Appendix 4. Most of the structures are smaller than the reference structure drawn according to the ESTRO recommendations, as in the examples of *CTV_WB* and *PTV_WB* (see Appendices 2-3). As shown in Appendix 5, the contrast between the Heart structures and the reference (light blue colour) structure is also noticeable. Most of the structures are smaller than the reference structure drawn by ESTRO guidelines. Appendix 6 shows images of the *Lung_ipsilat* structure. As can be seen from the images on the different axes, all the volumes of *Lung_ipsilat* are next to each other. Images of the *Spinal_cord* structure shown in Appendix 7, as in the case of *Lung_ipsilat* (see Appendix 6), do not show significant deviations. The *Lung_ipsilat* and *Spinal_cord* structures did not have a reference structure created.

After the systematisation of treatment information and visualisation of different structures, the treatment planning system "Eclipse" was used to evaluate the volume of the main structures (*CTV_WB, PTV_WB, PTV_WB_dvh, Heart, Lung_ipsilat* and *Spinal_cord*). For volume analysis, the mean, standard error, median, standard deviation, lowest and maximum values, and distribution range were founded. A boxplot was drawn to better visualise the change in values. The results are shown in Figures 23-29.

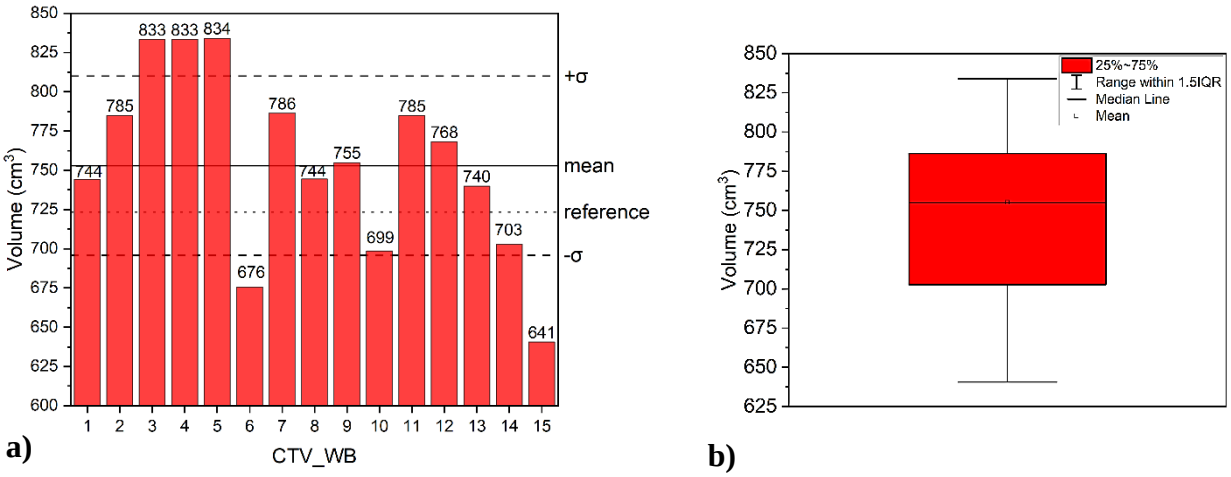

Fig. 23. Different *CTV_WB* volumes: a) histogram of volumes; b) boxplot

Figure 23 shows different *CTV_WB* volumes. It can be seen from Figure 23 a) that the value of the reference volume is 723.0 cm^3; compared to the other volumes, 4 plans (6th, 9th, 14th, 15th) are below reference volume, and 11 are above reference volume. Only the volume of the 10th, 13th, and 15th plans differs ≤ 20.0 cm^3, also mean value and standard deviation (σ) are shown. Figure 23 b) shows the boxplot. Based on Khan Academy: "A boxplot displays the five-number summary of a set of data. The five-number summary is the minimum, first quartile, median, third quartile, and maximum" [104], also, the mean value in the boxplot was presented. Galarnyk (2018) says: "Median (Q_2/50th percentile) is the middle value of the dataset. The first quartile (Q_1/25th percentile) is the middle number between the smallest number (not the minimum) and the median of the dataset. Third quartile (Q_3/75th percentile): is the middle value between the median and the highest value (not the maximum) of the dataset. Interquartile range (*IQR*): 25th to the 75th percentile" [105]. From the boxplot, it is seen that there are no outliers, and the median and mean values almost coincide. The mean value is 753.0 cm^3 which is 30.0 cm^3 higher than the reference value standard error (regarding Kelton's (2021) work: "The standard error is a statistical term that measures the accuracy with which a sample distribution represents a population by using standard deviation" [106]) is 14.0 cm^3, the median value is 750.0 cm^3, the standard deviation (Hargrave (2021) states, that: "The standard deviation is a statistic that measures the dispersion of a dataset relative to its mean and is calculated as the square root of the variance" [107]) is 57.0 cm^3, the minimum value is 641.0 cm^3, and the maximum is 834.0 cm^3, range between minimum and the maximum value is 193.0 cm^3.

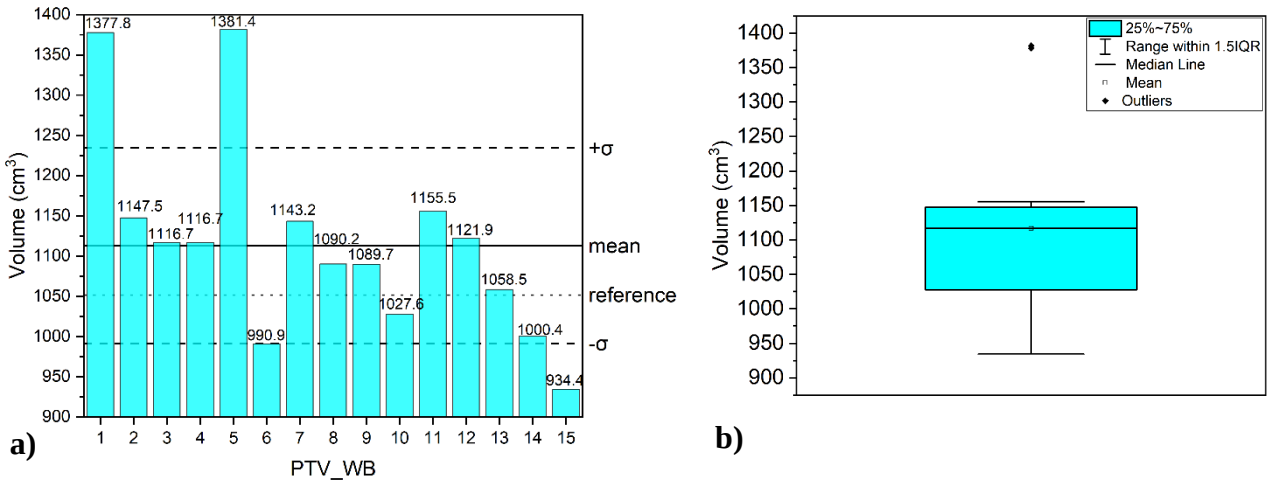

Fig. 24. Different *PTV_WB* volumes: a) histogram of volumes; b) boxplot

Different *PTV_WB* volumes are shown in Figure 24. Figure 24 a) shows that the reference volume is 1052.0 cm^3 and that 4 plans (6th, 10th, 14th, 15th) are below reference volume and 11 are above reference volume compared to the other volumes. Only the volume of the 10th and 13th plans differs $\leq$ 30.0 cm^3, also mean value and standard deviation (σ) are shown. The boxplot is shown in Figure 24 b). The boxplot reveals two outliers on the higher volume side, and the median and mean values are nearly identical. The median value is 1103.5 cm^3, the standard deviation is 121.3 cm^3, the minimum value is 934.4 cm^3, the maximum is 1381.4 cm^3, and the range between the minimum and the maximum value is 447.0 cm^3. The mean value is 1112.8 cm^3, which is 60.8 cm^3 greater than the reference value.

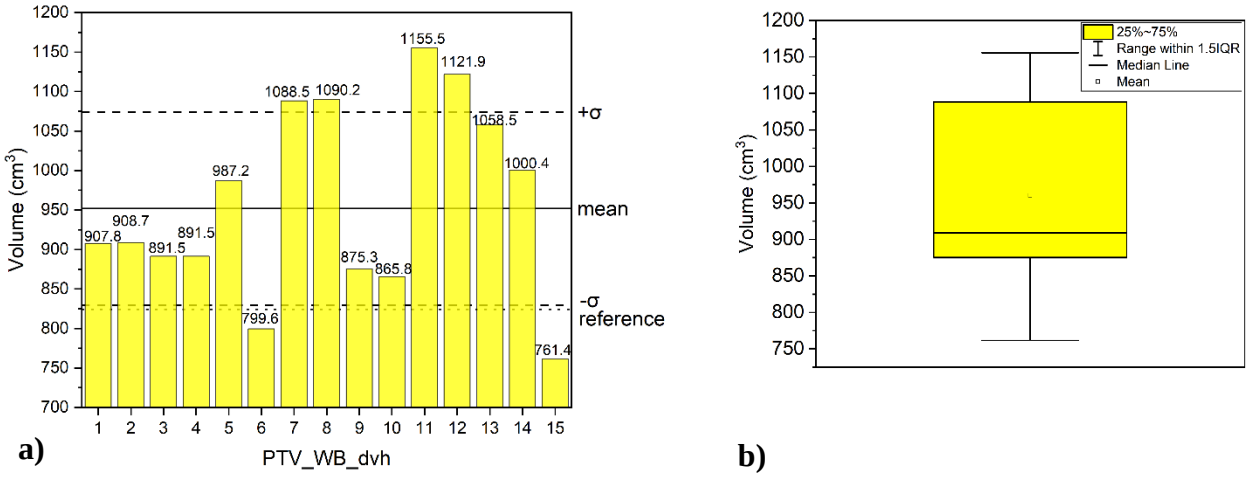

Fig. 25. Different *PTV_WB_dvh* volumes: a) histogram of volumes; b) boxplot

Different *PTV_WB_dvh* volumes are shown in Figure 25. Figure 25 a) shows that the reference volume is 824.4 cm^3, and all plans (except the 6th and 15th plans) are above the reference volume compared to the other volumes, also mean value and standard deviation (σ) are shown. The boxplot is shown in Figure 25 b). There are no outliers in the boxplot, and the median and mean values are different. The mean value is 951.8 cm^3, which is 127.4 cm^3 greater than the reference value, with a standard error of 30.5 cm^3, a median value of 908.3 cm^3, a standard deviation of 122.0 cm^3, a minimum of 761.4 cm^3 and a maximum of 1155.5 cm^3, and a range of 394.1 cm^3 between the minimum and highest values.

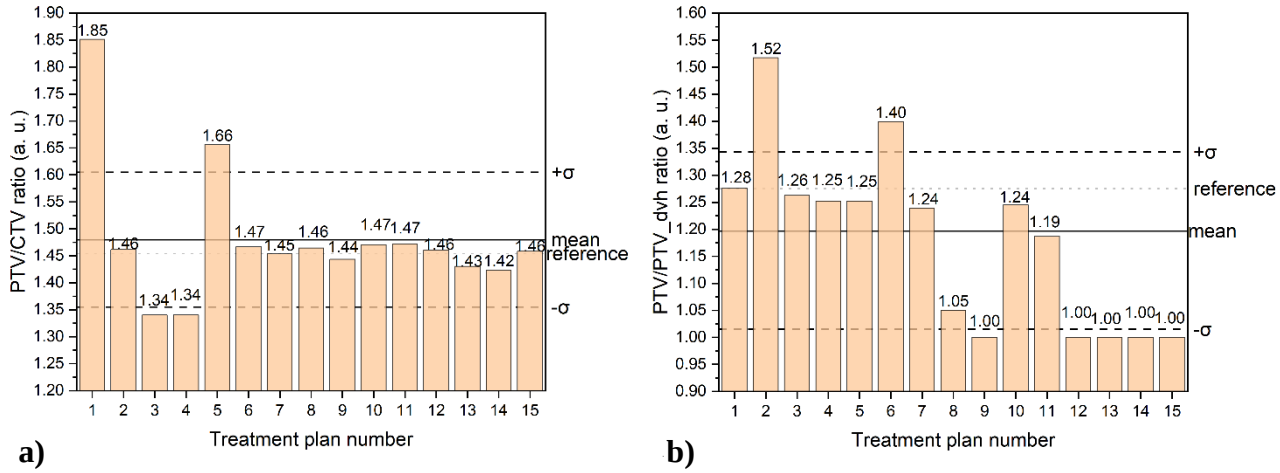

Fig. 26. Different ratios: a) *PTV/CTV*; b) *PTV/PTV_dvh*

Figure 26 depicts various *PTV/CTV* and *PTV/PTV_dvh* ratios. From Figure 26 a), the value of the reference plan ratio is 1.354 a. u., and 5 plans (3rd, 4th, 9th, 13th, and 14th) are below reference volume, and 10 are above reference volume compared to the other *PTV/CTV* ratios. Only the *PTV/CTV* ratios of the 2nd, 7th, 12th, and 15th plans differ ≤ 0.01 a. u. 1.480 a. u. is the average value, which is 0.026 a. u. greater than the reference value. The standard error is 0.032 a. u., the median value is 1.461 a. u., the standard deviation (σ) is 0.125 a. u., the minimum value is 1.340 a. u., and the maximum is 1.851 a. u., with a range of 0.511 a. u., between them. When the margin is 0.5 cm (see Table 9), the value obtained is close to 1.454 a. u., however, when the margin is different, various values are obtained (when the margin is > 0.5 cm, the PTV/CTV ratio is > 1.45 a. u., and when the margin is 0.5 cm, the *PTV/CTV* ratio is 1.454 a. u.). Compared to the other *PTV/PTV_dvh* ratios, the value of the reference plan ratio is 1.276 a. u., showing that all plans (except 1st, 2nd, and 6th plans) are below reference volume according to Figure 26 b). The *PTV/PTV_dvh* ratios of the 1st, 3rd, 4th, 5th, 7th, and 10th plans differ ≤ 0.04 a. u. The average value is 1.179 a. u., which is 0.097 a. u. higher than the reference value. The standard error is 0.042 a. u., the median value is 1.239 a. u., the standard deviation (σ) is 0.164 a. u., the minimum value is 1.000 a. u., and the maximum value is 1.518 a. u., with a range of 0.518 a. u., between them. In the 5 plans (9th, 12th-15th), the volume of *PTV* and *PTV_dvh* are the same.

After completing the analysis of clinical structures (*CTV_WB* and *PTV_WB*) and *PTV_WB_dvh*, which is developed for evaluation of the planned plan and calculations of *PTV/CTV* and *PTV/PTV_dvh* ratios, it was moved to analysis of critical organs (*Heart, Lung_ipsilat* and *Spinal_cord*) volumes.

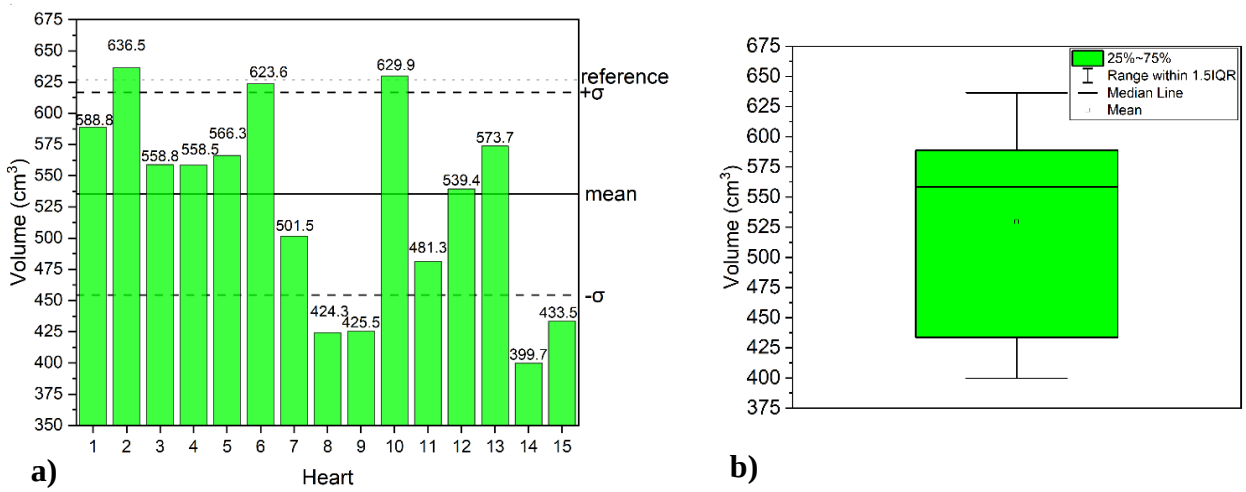

Fig. 27. Different *Heart* volumes: a) histogram of volumes; b) boxplot

Different *Heart* volumes are shown in Figure 27. Figure 27 a) shows that the reference volume is 626.5 cm^3, and 2 plans (2nd and 10th) are above reference volume, and 13 are below reference volume when compared to the other volumes. Only the 2nd, 6th, and 10th plans have a volume difference of ≤ 10.0 cm^3, also mean value and standard deviation (σ) are shown. The boxplot is shown in Figure 27 b). The boxplot has no outliers, and the median and mean values have changed. The mean value is 535.5 cm^3, which is 93.0 cm^3 less than the reference value, with a standard error of 20.3 cm^3, a median value of 558.7 cm^3, a standard deviation of 81.2 cm^3, a minimum of 399.7 cm^3, and a maximum of 636.5 cm^3, and a range of 236.5 cm^3, between them.

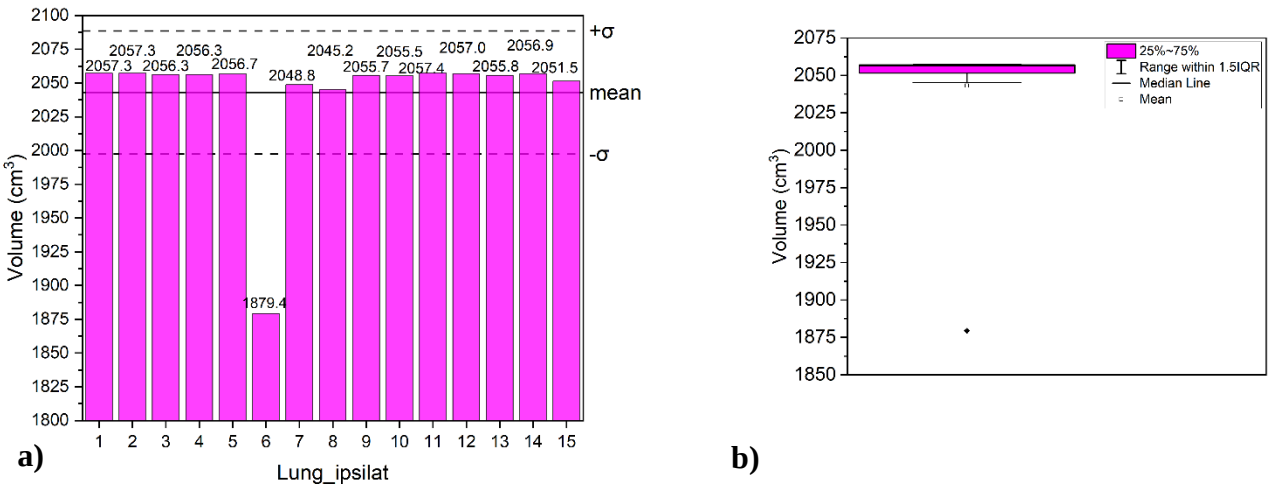

Fig. 28. Different *Lung_ipsilat* volumes: a) histogram of volumes; b) boxplot

Different *Lung_ipsilat* volumes are shown in Figure 28. Figure 28 a) shows that all volumes (except the 6th plan) are close to each other (the difference between volumes is < 10.0 cm^3), also mean value and standard deviation (σ) are shown. The boxplot is shown in Figure 28 b). The boxplot has one outlier (6th plan value), and the median and mean values are close to each other. The mean value is 2043.1 cm^3, a standard error of 11.7 cm^3, a median value of 2056.3 cm^3, a standard deviation of 45.5 cm^3, a minimum of 1879.4 cm^3, and a maximum of 2057.3 cm^3, and a range of 177.9 cm^3. This is the first structure when almost all volumes are close to each other.

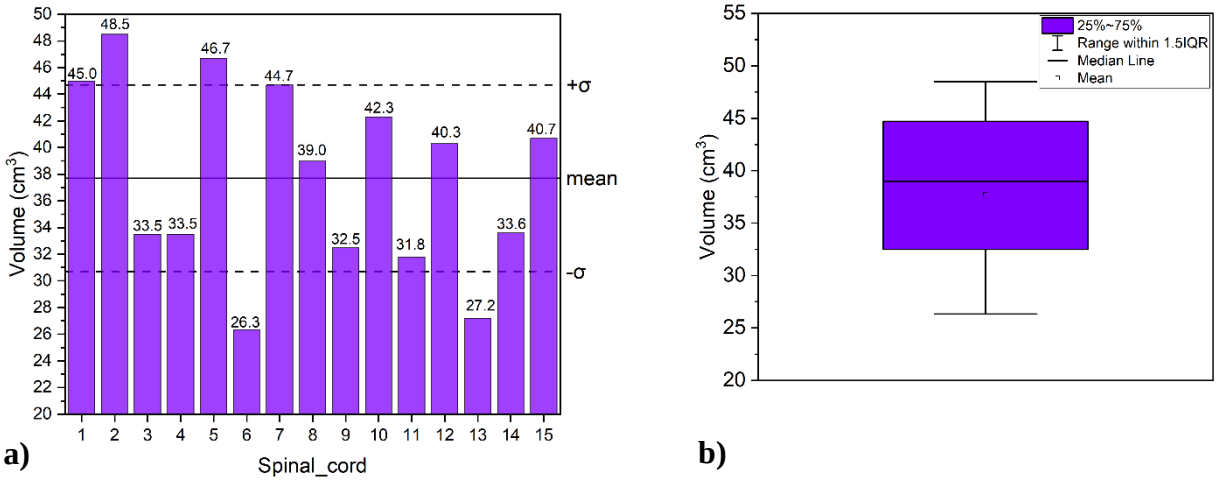

Fig. 29. Different *Spinal_cord* volumes: a) histogram of volumes; b) boxplot

Different *Spinal_cord* volumes are shown in Figure 27. Figure 27 a) shows that all volumes are in 25-50 cm^3 intervals, also mean value and standard deviation (σ) are shown. The boxplot is shown in Figure 27 b). The boxplot has no outliers, and the median and mean values are close to each other (differ < 1.5 cm^3). The mean value is 37.7 cm^3, a standard error of 1.8 cm^3, a median value of 39.0 cm^3, a standard deviation of 7.0 cm^3, a minimum of 26.3 cm^3, and a maximum of 48.5 cm^3, and a range of 22.2 cm^3.

The plan (two opposing fields) created by artificial intelligence (AI) was also compared with the reference plan. The volume of *CTV_WB* is found to be 735 cm^3, which is only 12 cm^3 different from the reference volume; *PTV_WB* is 1066.0 cm^3, which is 14 cm^3 different from the reference volume. The *PTV/CTV* ratio is 1.45 a. u., the same as for reference. *PTV_WB_dvh* is found to be 835 cm^3. In the plan developed by AI, the volume of the *Lung_ipsilat* is 2135.8 cm^3, the volume of the

Spinal_cord is 36.3 cm^3, and the volume of the *Heart* is 605.5 cm^3, which differs from the reference plan by 21.5 cm^3.

After analysing the volumes of the investigated structures (*CTV_WB*, *PTV_WB*, *PTV_WB_dvh*, *Heart*, *Lung_ipsilat* and *Spinal_cord*), it was found that when the margin is different from 0.5 cm, the resulting volumes begin to differ significantly from the reference volume. According to ESTRO recommendations, the best margin between *PTV* and *CTV* is 0.5 cm. It was seen that when the *PTV/CTV* ratio is 1.45 a. u., the values of the received plans are close to the reference value, and the margin used during the plan is 0.5 cm; therefore, by analysing the *PTV/CTV* ratio, the value of the margin used can be determined quite accurately. After the volume analysis of different structures, the study of similarity characteristics goes ahead.

3.2. Similarity characteristics analysis of *CTV_WB* and *PTV_WB* structures

After analysing the volumes of the structures (*CTV_WB*, *PTV_WB*, *PTV_WB_dvh*, *Heart Lung_ipsilat* and *Spinal_cord*), the calculations of the similarity characteristics for *CTV_WB* and *PTV_WB* will be performed. The images (*CTV_WB* and *PTV_WB*) used to calculate the similarity characteristics are given in Annexes 8-9. Annexe 8 shows *CTV_WB*, and annexe 9 shows *PTV_WB* images. Appendices 8-9 supply images of the plans developed by the 15 radiation-oncologists who participated in the practical task and a reference plan created by dr. Laimonas Jaruševičius and dr. Evelina Koleibnikova. Appendices 10-11 supply *CTV_WB* and *PTV_WB* reference images using a different threshold value (0.0-0.99) that is used in further calculations.

The calculated *CTV_WB* similarity characteristics with different threshold values are given in Annexes 12-26, and *PTV_WB* similarity characteristics are shown in Annexes 27-41. Volumetric Similarity Coefficient (*VS*), Hausdorff distance (*HD*) and Average distance (*AVD*) are not used in the analysis, as they are 3D characteristics. Accuracy (*ACU*) (Based on Cambridge dictionary: "Accuracy is also the agreement of a particular measurement with an accepted standard" [108]) and precision (*FPR*) (as stated in Cambridge dictionary: "Precision is also the level of agreement of a particular measurement with itself when it is repeated" [109]) is additionally calculated, also time (*TIME*) taken for the calculation is shown.

Figures 30-31 show the *CTV_WB* and *PTV_WB* structures' *DICE* values calculated by the "Eclipse" treatment planning system.

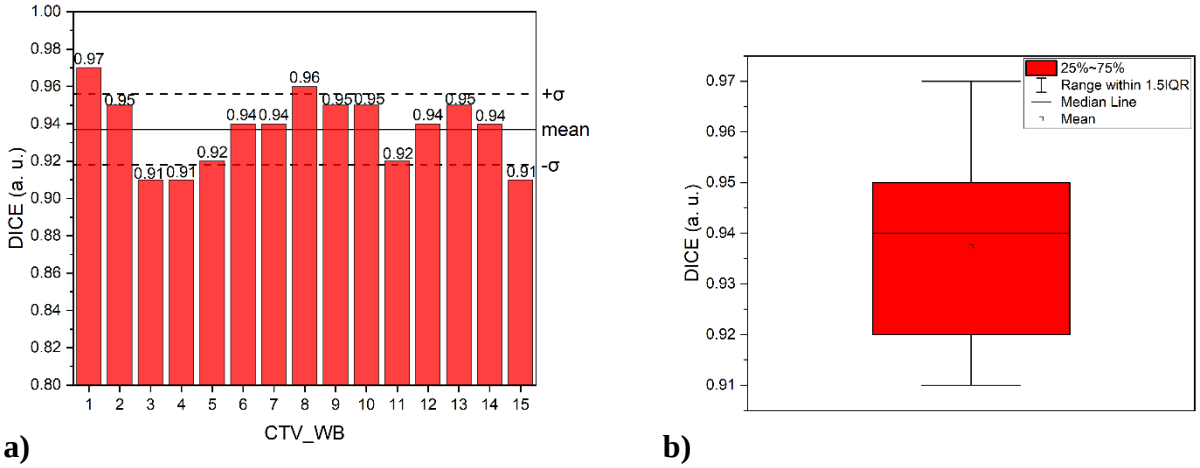

Fig. 30. Different *CTV_WB* similarity values: a) histogram of values; b) boxplot

DICE similarity values for the *CTV_WB* structure are shown in Figure 30. Figure 30 a) shows that the lowest similarity value is 0.910 a.u. and the highest is 0.970 a. u., also mean value and standard deviation (σ) are shown. The boxplot is shown in Figure 30 b). There are no outliers in the boxplot, and the median and mean values are nearly identical. The median value is 0.940 a. u., the mean value is 0.937 a. u., the standard deviation is 0.019 a. u., the minimum value is 0.910 a. u., the maximum is 0.970 a. u., and the range between the minimum and maximum value is 0.060 a. u.

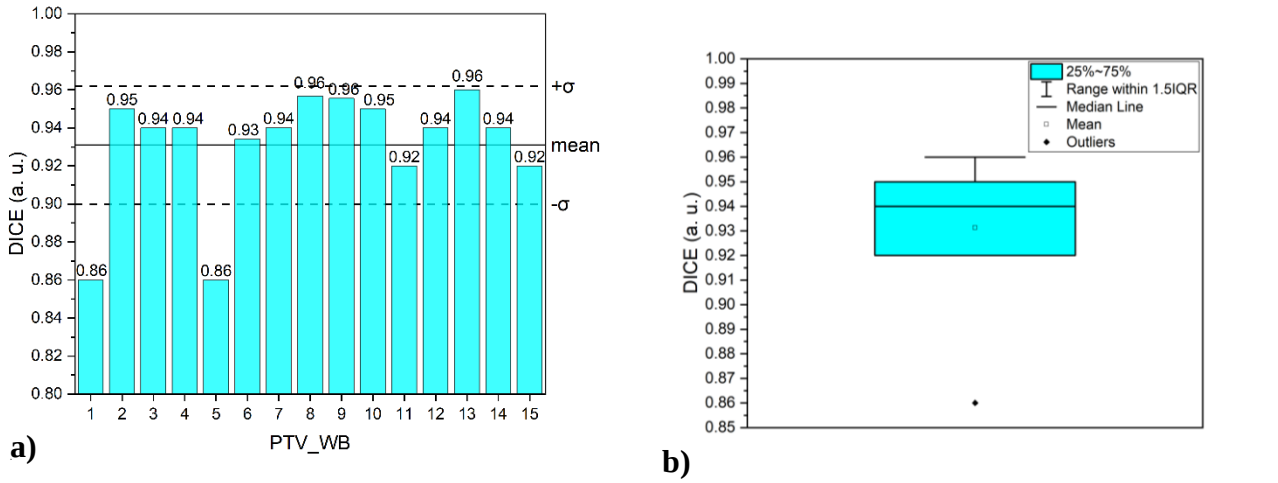

Fig. 31. Different *PTV_WB* similarity values: a) histogram of values; b) boxplot

The *DICE* similarity values for the *PTV_WB* structure are shown in Figure 31. The lowest similarity value is 0.860 a. u., and the highest is 0.960 a. u., also mean value and standard deviation (σ) are shown in Figure 31 a). Figure 31 b) depicts the boxplot. In the boxplot, there are outliers, and the median and mean values are practically equal. The standard error is 0.008 a. u., and the mean value is 0.931 a. u. The median value is 0.940 a. u., the standard deviation is 0.031 a. u., the minimum value is 0.860 a. u., the maximum is 0.960 a. u., and the range is 0.100 a. u.

Difference between *CTV_WB* (see Figure 30) and *PTV_WB* (see Figure 31) *DICE* similarity (according to the ESTRO recommendations [38], a specific, equal margin is added to the *CTV* structure, and a *PTV* structure is obtained, so the values should be the same), may be interpreted based on the *PTV/CTV* ratio at a value of 1.45 ± 0.02 a. u., the difference between the *CTV_WB* and *PTV_WB DICE* coefficients is ± 0.01 a. u. or there is no difference between *CTV_WB* and *PTV_WB*. The first plan states that the *PTV/CTV* ratio is 1.85 a. u. (see Figure 26 a), in this case, the *DICE* value differs by 0.11 a. u., in the 3rd and 4th plans, the *PTV/CTV* ratio is 1.34 a. u. (see Figure 26 a), and the value of the *DICE* coefficient differs by 0.03 a. u. In the 4th plan, the *PTV/CTV* ratio is 1.66 a. u. (see Figure 26 a), and it is obtained that the value of the *DICE* coefficient differs by 0.06 a. u.

After analysis, the threshold value used in the Eclipse" treatment planning system was found to be in the range of 0.2-0.4 a. u., but 0.4 a. u. was selected for further analysis. Appendices 42-43 provide similarity characteristics with the most likely threshold value that corresponds to the threshold value used in the "Eclipse" treatment planning system.

Figures 32-33 show the *DICE* similarity coefficient values calculated by the "EvaluateSegmentation" software.

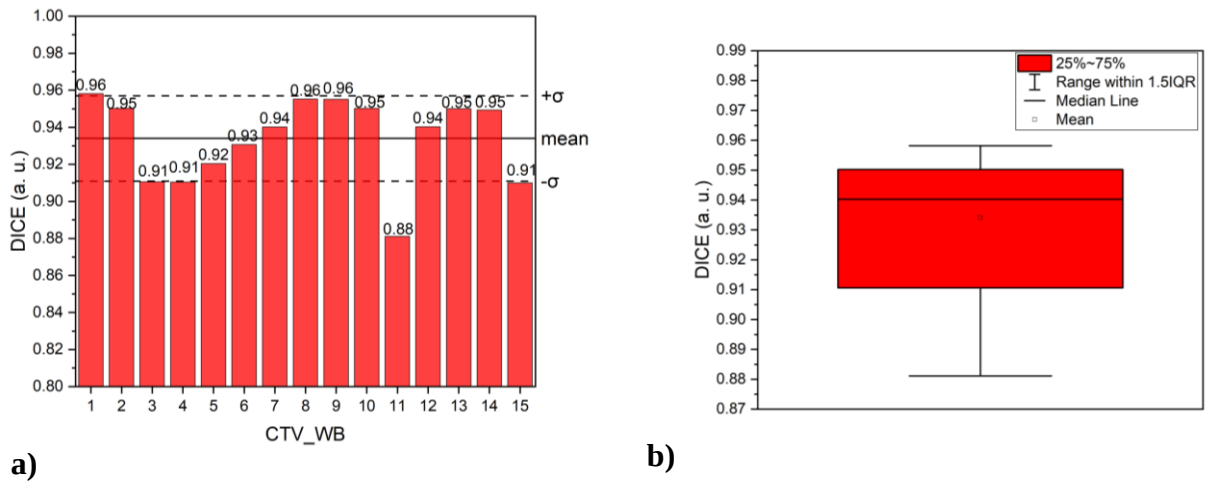

a) b)

Fig. 32. Different *CTV_WB* similarity values calculated with "EvaluateSegmentation" software: a) histogram of values; b) boxplot

Different *CTV_WB* structure *DICE* similarity values determined using the "EvaluateSegmentation" program are shown in Figure 32. The least similarity value is 0.880 a. u., and the highest is 0.960 a. u., also mean value and standard deviation (σ) are shown in Figure 32 a). The boxplot is shown in Figure 32 b). There are no outliers in the boxplot, and the median and mean values are different (differ less than 0.060 a. u.). The median value is 0.940 a. u., the standard deviation is 0.023 a. u., the minimum value is 0.880 a. u., the maximum is 0.960 a. u., and the range between the minimum and maximum value is 0.080 a. u.

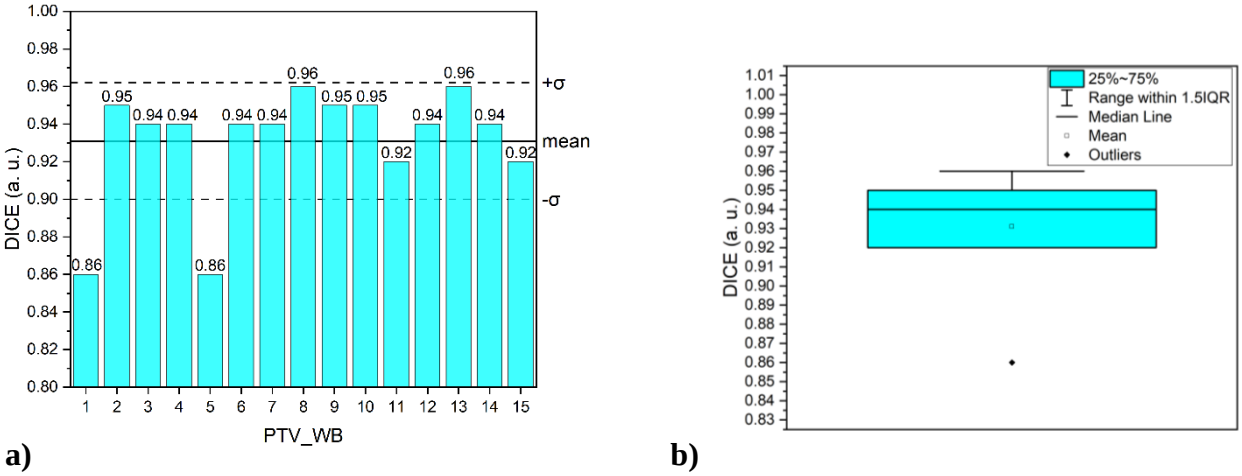

a) b)

Fig. 33. Different *PTV_WB* similarity values calculated with "EvaluateSegmentation" software: a) histogram of values; b) boxplot

Figure 33 displays the *DICE* similarity values for the *PTV_WB* structure generated with the "EvaluateSegmentation" software. Figure 33 a) shows that the lowest similarity value is 0.860 a. u. and the highest is 0.960 a. u., also mean value and standard deviation (σ) are shown. The boxplot is shown in Figure 33 b). There is one outlier (0.860 a. u.) in the boxplot, and the median and mean values are different. The mean value is 0.931 a. u., the standard error is 0.008 a. u., the median value is 0.940 a. u., the standard deviation is 0.031 a. u., the minimum value is 0.860 a. u., and the maximum is 0.960 a. u., and the range between the minimum and maximum value is 0.100 a. u.

Comparing the results obtained with *CTV_WB* (see Figure 32) and *PTV_WB* (see Figure 33), it can be argued that even if a margin other than the ESTRO recommendations (0.5 cm) is chosen for

physicians, the deviation from the reference plan is not significant and should not have a significant impact on the planning phase and its evaluation according to clinical goals.

Figures 34-35 compare the structures of *CTV_WB* and *PTV_WB* with the treatment planning system "Eclipse" and the non-commercial "EvaluateSegmentation" software and show how these programs differ from each other.

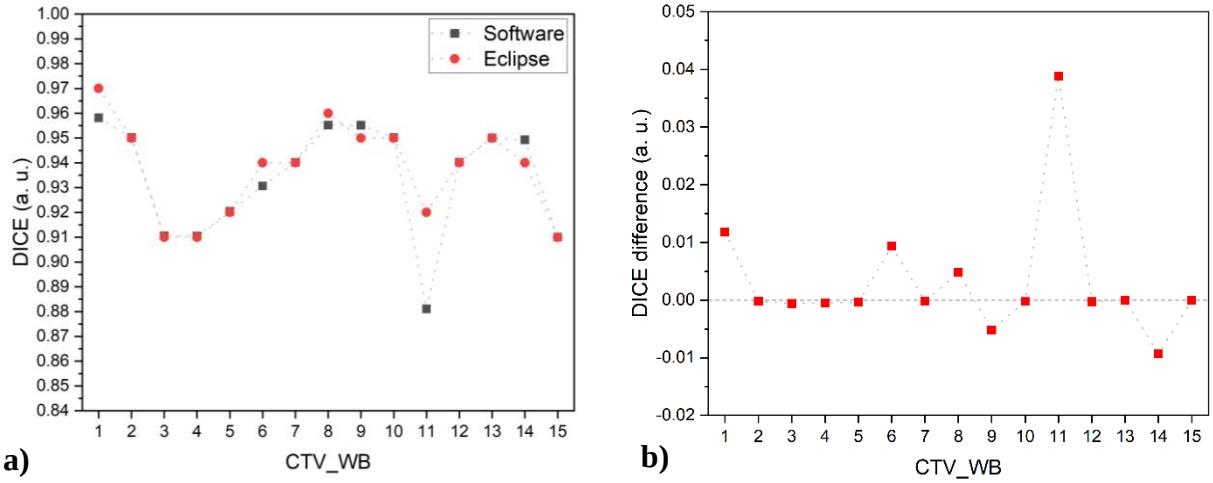

Fig. 34. *CTV_WB* structure *DICE* similarity coefficient calculated with "EvaluateSegmentation" software (black) and "Eclipse" program (red) comparison: a) calculated values; b) difference between values. Dot lines only for visualisation purposes

Figure 34 shows the *CTV_WB* structure *DICE* similarity coefficient values calculated with "EvaluateSegmentation" software and "Eclipse" program comparison. Figure 34 a) shows the comparison between the calculated *DICE* similarity coefficient with commercial ("Eclipse" program) and non-commercial ("EvaluateSegmentation" software) programs, and Figure 34 b) shows the difference between programs' calculated *DICE* similarity coefficient with commercial and non-commercial programs. The mean value with "EvaluateSegmentation" software is 0.934 a. u., which is 0.003 a. u. smaller than with the "Eclipse" program, the standard error is 0.006 a. u., which is 0.001 a. u. higher than with the commercial program. The median value in both cases is the same – 0.940 a. u. The standard deviation with the "EvaluateSegmentation" software is 0.023 a. u., which is 0.004 a. u. higher than with the "Eclipse" treatment planning program. The minimum value is 0.880 a. u., which is 0.030 a. u. smaller than with the treatment planning system "Eclipse", and the maximum value with the "EvaluateSegmentation" software is 0.960 a. u., which is 0.010 a. u. smaller than with the commercial program. Only the 11th plan *DICE* value differs > 0.04 a. u., this difference may be explained by a human error in the preparation of images for the measurement process with "EvaluateSegmentation" software. Pearson correlation coefficient [110] was used to evaluate the correlation between the data obtained from different programs (treatment planning system "Eclipse" and "EvaluateSegmentation"), it was found that $R = 0.8738$.

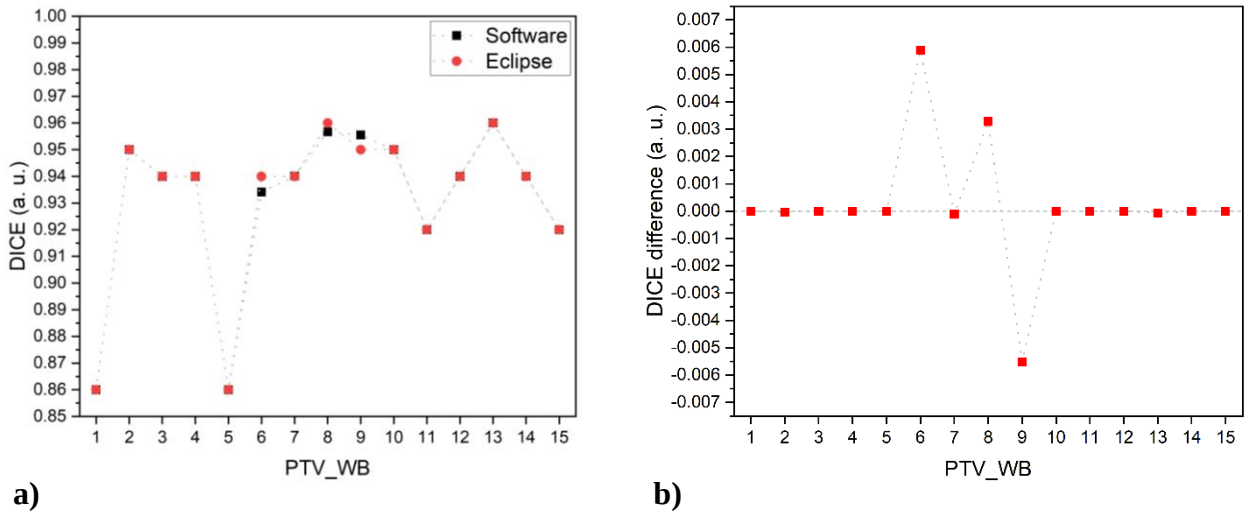

Fig. 35. *PTV_WB* structure *DICE* similarity coefficient calculated with "EvaluateSegmentation" software (black) and "Eclipse" program (red) comparison: a) calculated values; b) difference between values. Dot lines only for visualisation purposes

The *DICE* similarity coefficient values for the *PTV_WB* structure calculated with the "EvaluateSegmentation" software, and the "Eclipse" program are shown in Figure 35. Figure 35 a) shows the comparison of the calculated *DICE* similarity coefficient with commercial and non-commercial programs, and Figure 35 b) shows the difference in the computed *DICE* similarity coefficient between commercial and non-commercial programs. Both the "EvaluateSegmentation" software and the "Eclipse" application use the same primary parameters. The mean value is 0.931 a. u., the standard error is 0.008 a. u., the median value is 0.940 a. u., the standard deviation is 0.031 a. u., the minimum value is 0.860 a. u., and the maximum is 0.960 a. u., and the range between the minimum and maximum value is 0.100 a. u., although in two plans (6th and 9th, the value of *DICE* differs > 0.005 a.u.). Pearson correlation coefficient is $R = 0.9972$.

Figure 36 shows the similarity characteristics calculated in this work (Dice Coefficient (*DICE*), Jaccard Coefficient (*JAC*), The area under ROC Curve (*AUC*), Cohen Kappa (*KAP*), Rand Index (*RI*), Adjusted Rand Index (*ARI*), Mutual Information (*ICC*), Variation of Information (*VOI*), Global Consistency Error (*GCE*), Probabilistic Distance (*PBD*)), as well as statistical concepts (True-positive rate (Sensitivity, recall) (TPR), True-negative rate (Specificity) (*TNR*), Precision (Confidence) (*PRN*), F-Measure (*FMS*), Accuracy (*ACU*), False-positive rate (Fallout) (*FPR*).

Comparing commercial ("Eclipse" treatment planning system) and non-commercial ("EvaluateSegmentation" software) programs, it can be stated that the results obtained by them are similar, and "EvaluateSegmentation" software is dependable in assessing the similarity characteristics of medical images.

After calculating the *DICE* coefficient and evaluating its similarity, which is evaluated with commercial and non-commercial programs, it was switched to the calculation of other similarity characteristics with the "EvaluateSegmentation" software.

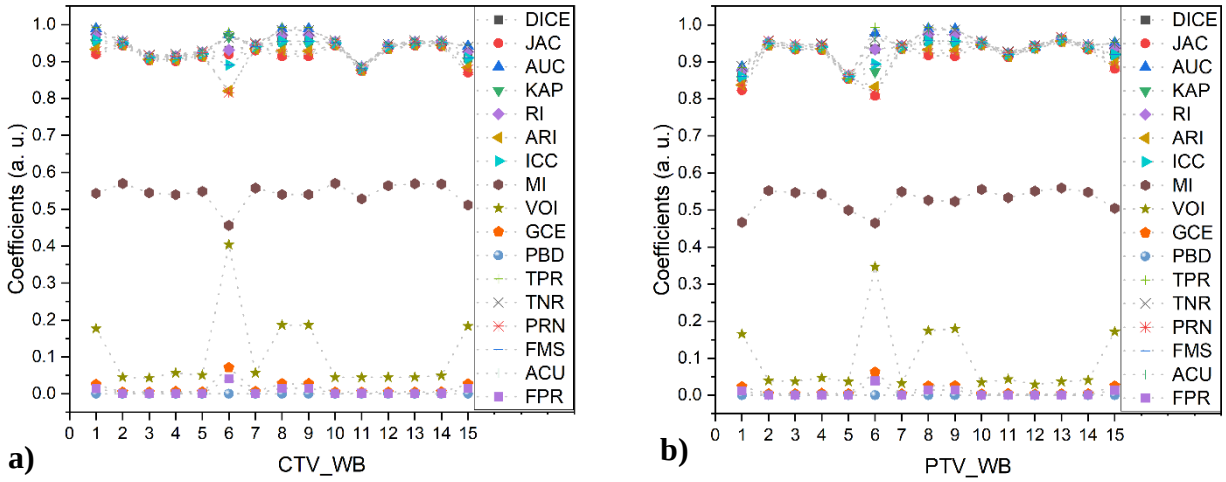

Fig. 36. Comparison of various characteristics of different structures: a) *CTV_WB*; b) *PTV_WB*. Dot lines only for visualisation purposes

Figure 36 shows that the coefficients can be divided into 3 groups: coefficients that follow or have a similar trend as Dice Coefficient (*DICE*) – Jaccard Coefficient (*JAC*), The area under ROC Curve (*AUC*), Cohen Kappa (*KAP*), Rand Index (*RI*), Adjusted Rand Index (*ARI*), Interclass Correlation (*ICC*), the coefficient corresponding to Dice Coefficient (*DICE*) multiplied by a specific coefficient – Mutual Information (*MI*) and coefficients not related to Dice Coefficient (*DICE*) – Variation of Information (*VOI*), Global Consistency Error (*GCE*), Probabilistic Distance (*PBD*). There are also statistical concepts that correspond to Dice Coefficient (*DICE*) – True-positive rate (Sensitivity, recall) (*TPR*), True-negative rate (Specificity) (*TNR*), Precision (Confidence) (*PRN*), F-Measure (*FMS*), Accuracy (*ACU*) and which does not meet Dice Coefficient (*DICE*) – False-positive rate (Fallout) (*FPR*).

Only one Dice Coefficient (*DICE*) can be calculated with the "Eclipse" treatment planning system, and with the "EvaluateSegmentation" software, Dice Coefficient (*DICE*) can be calculated, as well as 5 other coefficients – Jaccard Coefficient (*JAC*), The area under ROC Curve (*AUC*), Cohen Kappa (*KAP*), Rand Index (*RI*), Adjusted Rand Index (*ARI*), and when multiplied by a specific constant, 6th coefficient – a Mutual Information (*MI*), can be used.

The analysis of the similarity characteristics of the studied structures (*CTV_WB*, *PTV_WB* and *PTV_WB_dvh*) revealed that the results obtained with the treatment planning system "Eclipse" and the "EvaluateSegmentation" software are pretty similar, but with the "EvaluateSegmentation" software it is possible to calculate not only Dice Coefficient (*DICE*), but additionally – Jaccard Coefficient (*JAC*), The area under ROC Curve (*AUC*), Cohen Kappa (*KAP*), Rand Index (*RI*), Adjusted Rand Index (*ARI*), and with minimal adjustments also Mutual Information (*MI*), that are proportional to Dice Coefficient (*DICE*). After analysing the similarity characteristics, the study of treatment plans and clinical goals will be presented.

3.3. Analysis of planned treatment plans to assess the impact of structure volume

At the beginning of the analysis of the clinical goals of planned treatment plans and their dependence on structure volume, the arrangement of the used fields in different axes will be presented, when the parameters of the axes are *x =10.97 cm, y = -10.60 cm, z =1.50 cm*. These images are shown in Figure 37.

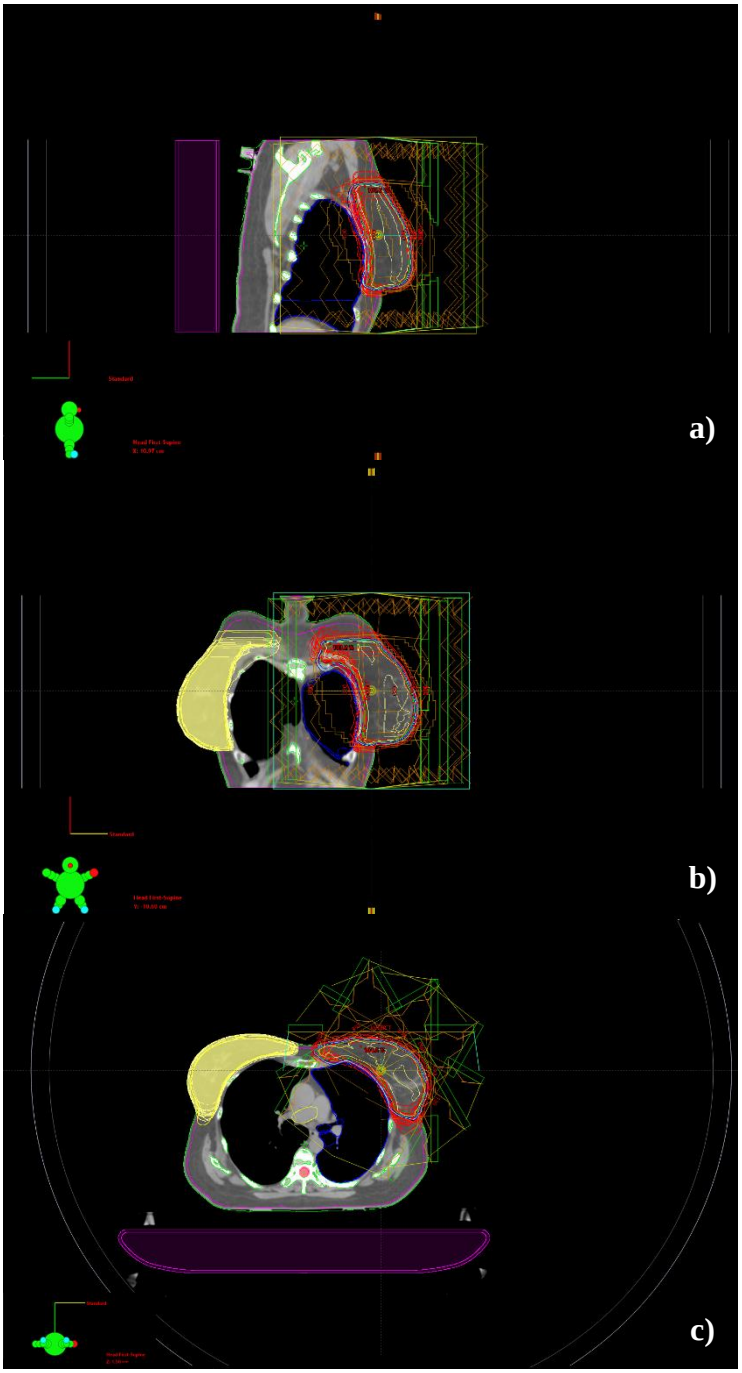

Fig. 37. Fields arrangement at different axis: a) transversal (x-axis); b) frontal (y-axis); c) sagittal (z-axis)

Figure 37 shows the different clinical structures and fields used. Looking at the patient images on the different axes, it can be seen that a multileaf collimator (MLC) is used (see Figure 37 b), that the clinical structures are of varied sizes (see Figure 37 a-c) and that the fields are arranged on different axes (see Figure 37 a-c).

After reviewing the fields used on the *x*, *y*, and *z* axes, it was shifted to examining the DVH curves and clinical goals of the plans. Table 10 shows the values of the clinical goals of the different plans. Figure 38 shows the DVH curves; the values are given in Table 10. Figures 39-42 show statistical analysis of *PTV_WB_dvh*, *Hear*t, *Lung_ipsilat*, and *Spinal_cord* structures.

Table 10. The clinical goals of different plans

Structure	**PTV_WB_dvh**				**Heart**		**Lung_ipsilat**	**Spinal_cord**
Dose limit	V24.70 ≥ 95%	V27.30 < 5%	V27.80 < 2%	D_{max} < 28.60 Gy	V7.0 < 5%	V1.50 < 30%	V8.00 < 15%	D_{max} < 23.64 Gy
REF	97.95	0.00	0.00	27.20	0.00	18.31	-	-
1	90.14*					16.67	14.39	1.52
2	90.14*					18.31	14.42	1.49
3	90.28*					14.68	14.40	1.40
4	90.28*					14.68	14.40	1.40
5	83.46•					13.79	14.40	1.49
6	95.91					18.83	15.75	1.47
7	78.57•					12.29	14.45	1.47
8	94.63*					10.60	14.48	1.39
9	92.34*					8.86	14.40	1.38
10	91.48*					17.08	14.40	1.46
11	88.09•					14.06	14.39	1.52
12	75.53•					12.23	14.39	1.43
12+	97.97			27.39		24.14	14.52	2.31
13	94.85*			27.20		16.12	14.40	1.77
14	96.18					6.35	14.39	1.39
15	96.25					9.39	14.44	1.41
AI	97.50					18.26	14.43	1.35

+The plan is created as completely new (only structures volumes are the same)

*Plan value differs <5% from recommended clinical goal (yellow colour in "Eclipse" TPS)

•Plan value differs >5% from recommended clinical goal (red colour in "Eclipse" TPS)

It can be seen from Table 10 that the volume uptake (V24.70 ≥ 95%) of only 3 plans (without reference plan, AI, and 12+) in the *PTV_WB_dvh* structure is satisfactory for the clinical goal (i.e., the value is higher than recommended), and the deviation of the 8 plans is < 5%, and a variation of 4 plans is > 5%. This difference could be explained by Figure 25 a) and Figure 26 b), the smaller the volume of *PTV_WB_dvh*, the higher the percentage, and conversely, the larger the volume, the lower the rate, e.g., the volume of the *PTV_WB_dvh* structure in plan 6th is 799.6 cm^3 (24.8 cm^3 less than the reference volume) and the *PTV/PTV_dvh* ratio is 1.40 a. u (0.046 a. u greater than the reference value), in the case of plan 12th the *PTV_WB_dvh* structure is 1121.9 cm^3 (297.5 cm^3 higher than the reference volume) and the *PTV/PTV_dvh* ratio is 1.00 a. u (0.354 a. u less than the reference value). The other volume uptake of the *PTV_WB_dvh* structure is equal to 0%, with a maximum dose of 27.20 Gy, corresponding to 104.6% of the prescribed dose. According to the ICRU 50 report [39], the prescribed dose should be -5% and + 7%, i.e., in the range of 95% to 107%. It can be seen from the *Heart* column that the values of the 2nd and 6th plans are in line with the reference value, also in the case of the plan created by artificial intelligence. The *Lung_ipsilat* column shows that the values for all plans (except plan 6th) are remarkably similar also for the AI plan. In the case of the

Spinal_cord structure, the difference between the maximum and minimum values is less than 0.20 Gy.

As with volume (see Section 3.1.), the clinical goals of the plan developed by AI were compared with those created by oncologists. It can be seen from Table 10 that the value *PTV_WB_dvh* volume is 97.50% or 0.45% lower than the reference volume, and the *Heart* volume is 18.26%, or only 0.05% lower than the value of the reference plan, so it can be stated that the AI program "RadForm" follows the ESTRO recommendations [38]. The *Lung_ipsilat* and *Spinal_cord* structures do not have reference plan values, so these values were compared to the mean value obtained. In the case of *Lung_ipsilat*, the volume value is 14.43% or only 0.07% lower than the average, and the dose received by *Spinal_cord* is 1.35 Gy and even 0.17 Gy lower than the average value. Comparing the plan developed by AI with oncologists' plans, it can be said that this technology is the future of treatment planning, but the final acceptance or rejection of the plan will be determined by the physician [109].

As can be seen in Table 10, a new plan 12 was created in addition (regardless of the size of the reference structures), which is denoted 12^{+}. The volume of the *PTV_WB_dvh* structure of plan 12 is 1121.9 cm^3 or even 387.5 cm^3 larger than the volume of the reference plan, but the clinical goal value ($V24.70 \geq 95\%$) is 0.02% greater than the value of the reference plan. The evaluated plans are developed according to the reference plan, therefore, their values are lower, if the plan is evaluated as a separate plan (without evaluating the reference structures), it should meet the table of clinical goals. The values of the clinical goals obtained with the 12^{+} plan is higher than the values of the 12 plan. *Heart* volume is higher almost 2 times, *Lung_ipsilat* is only 0.14% higher, and the dose obtained by *Spinal_cord* is 0.88 Gy higher, but all these values meet the clinical goal table (see Table 4) and do not cause any additional secondary lesions.

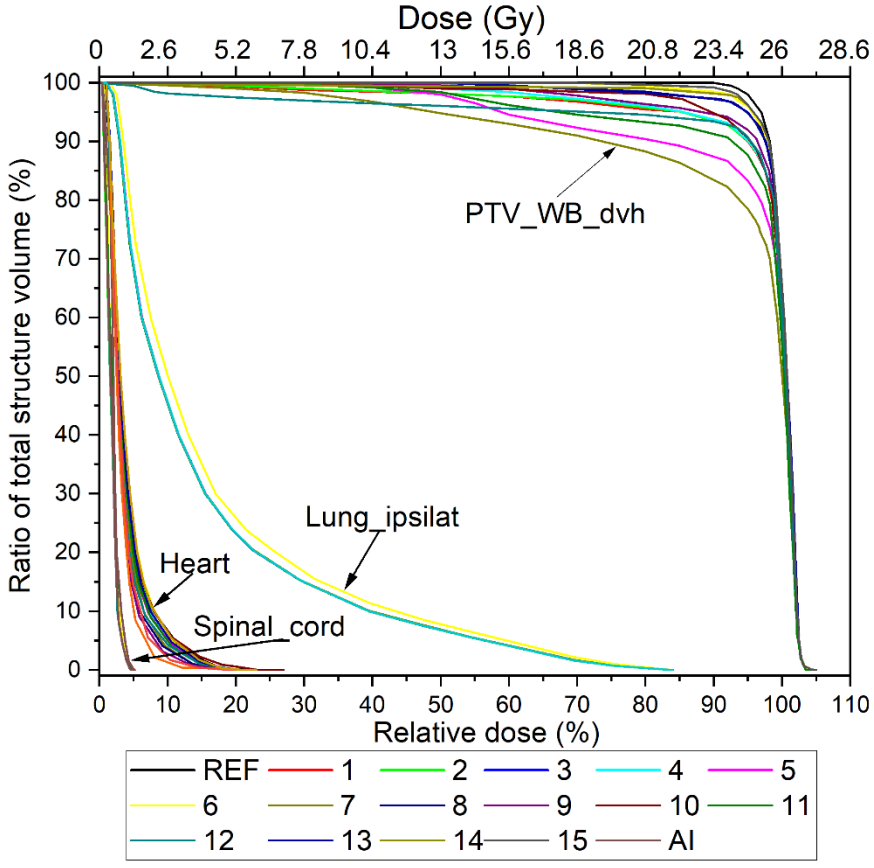

Fig. 38. Different DVH curves of *PTV_WB_dvh*, *Heart*, *Lung_ipsilat* and *Spinal_cord* structures

Figure 38 shows the treatment structure (*PTV_WB_dvh*) and the DVH curves of the three critical organs (*Heart, Lung_ipsilat* and *Spinal_cord*). When evaluating the *Spinal_cord* curves, all curves (except for the 13th plan) are adjacent to each other due to a slight difference in values (1.38-1.52 Gy). The dose value for *Spinal_cord* in plan 13th is 1.77 Gy, so this curve is slightly further to the right compared to the other plans. The *Heart* curves are distributed in ascending order (the 15th plane curve on the left is 6.35% by volume, and the 2nd and reference curves on the right are 18.31% by volume) from minimum to maximum. The *Lung_ipsilat* curves (except for the 6th plan) are the same (difference in values only 0.09%), only the 6th plan curve is slight to the right (compared to the other curves) due to the volume value of this plan being 15.75% or 0.16% more significant than the other largest plan 8th volume. When examining the *PTV_WB_dvh* curves, a clear dependence of the curves cannot be seen, as in the case of critical organs (*Heart, Lung_ipsilat,* and *Spinal_cord*). For example, the lowest is the plan 7th curve (volume value is 78.57%), although the lowest value should be plan 12th (volume value is 75.53%) and the highest in the reference plan curve (volume value is 97.95%). Curves 5th, 11th and 12th show a sharp decrease in value and then a steady decline again.

After examining the DVH curves, the statistical analysis of the *PTV_WB_dvh, Heart, Lung_ipsilat* and *Spinal_cord* structures were performed. The results of this analysis are shown in Figures 39-42. When analysing clinical goals, it should be noted that in the case of a larger volume, not only the tumour but also the additional tissues receive radiation (the dose given during treatment), which can lead to secondary factors – complications [111]. In the case of a smaller volume (drawn according to ESTRO recommendations [38]), the value of the clinical goal is higher, but in this way, adjacent tissues are protected, and additional complications are avoided.

According to a study [97] done by the University Hospitals of the North Midlands and the University of Keele in Stoke on Trent in the United Kingdom, in which 4110 women took part ("1361 received 40 Gy given in 15 treatments of 2.67 Gy over 3 weeks, 1367 females received 27 Gy in 5 treatments of 5.4 Gy over 1 week and patients received 26 Gy in 5 treatments of 5.2 Gy over 1 week" [97]). The researchers' analysis showed that persons who received 27 Gy of radiation were more likely to experience skin adverse effects 5 years later than those who received 40 Gy. When the outcomes of the 27 Gy over 1-week program were compared to the 26 Gy over 1-week schedule, the researchers discovered that the 26 Gy schedule was less likely to produce skin adverse effects and breast shrinkage.

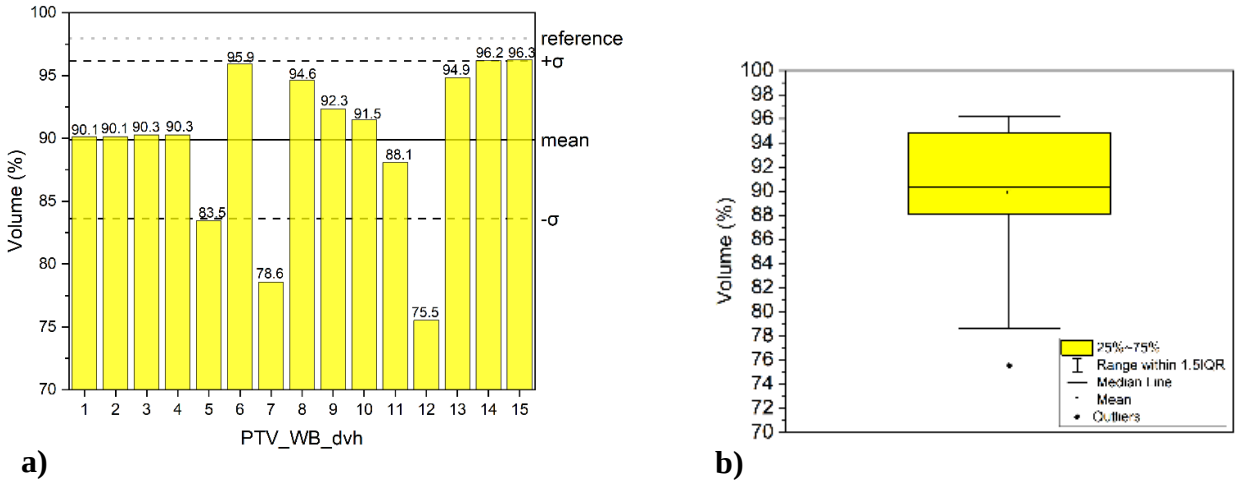

a) **b)**

Fig. 39. Statistical analysis of *PTV_WB_dvh* structure DVH curve values: a) histogram of values; b) boxplot

The DVH curve values for the *PTV_WB_dvh* structure are shown in Figure 39. The lowest DVH curve value is 75.30%, and the highest is 96.18% (1.77% smaller than the reference plan value), also mean value and standard deviation (σ) are shown in Figure 39 a). Figure 39 b) depicts the boxplot. The boxplot has one outlier (12th plan value), and the median and mean values are slightly different. The standard error is 1.62%, and the mean value is 89.88%. The median value is 90.28%, the standard deviation is 6.28%, the minimum value is 75.30%, the maximum is 96.18%, and the range is 20.65%.

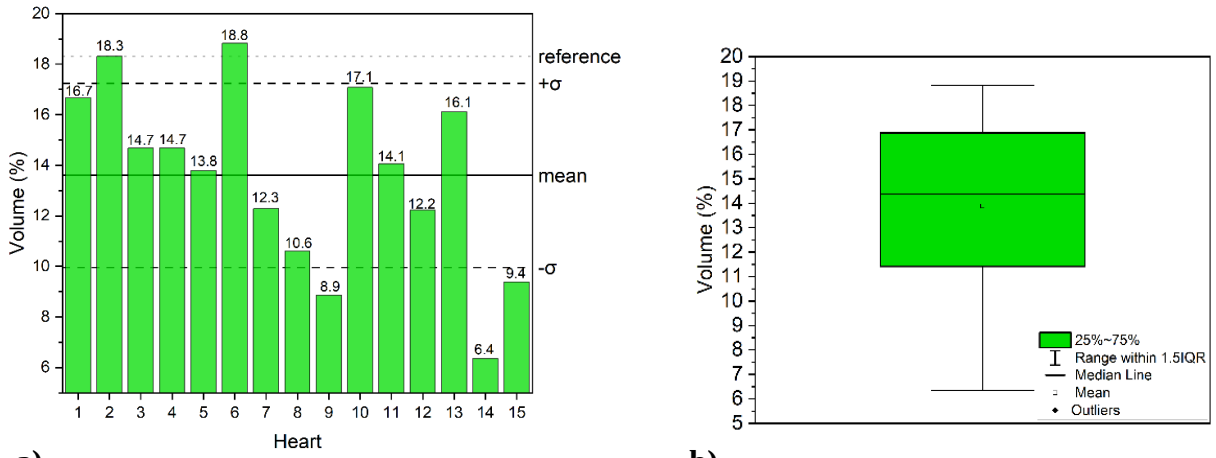

a) **b)**

Fig. 40. Statistical analysis of *Heart* structure DVH curve values: a) histogram of values; b) boxplot

Figure 40 shows the DVH curve values for the *Heart* structure. As presented in Figure 40 a), the lowest DVH curve value is 6.35%, and the greatest is 18.83% (0.52% larger than the reference plan value), also mean value and standard deviation (σ) are shown. The boxplot is shown in Figure 40 b). There are no outliers in the boxplot, and the median and mean values are different. The mean value is 13.60%, while the standard error is 0.94%. The median value is 14.06%, with a standard deviation of 3.64%, a minimum value of 6.35%, a maximum of 18.83%, and a range of 12.48%.

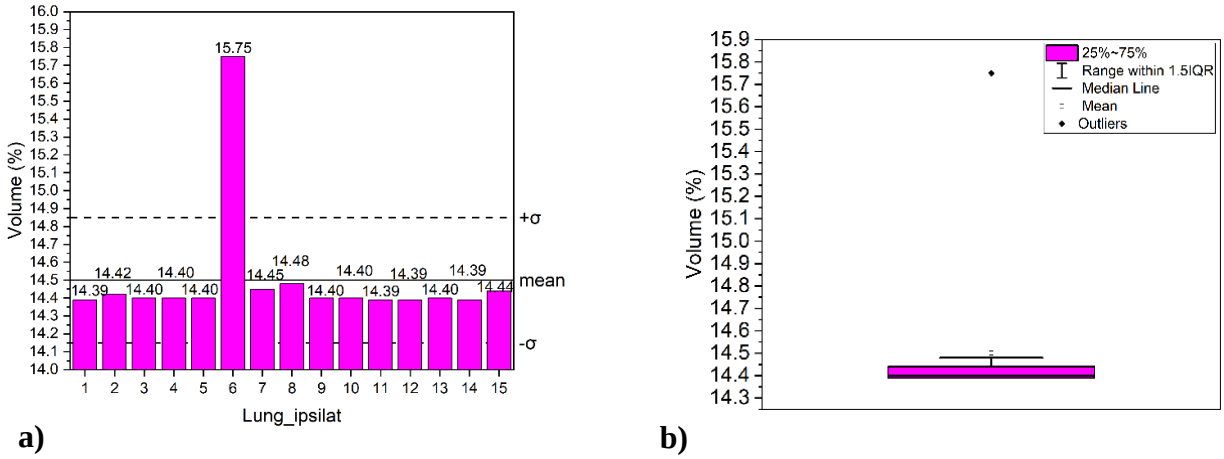

a) **b)**

Fig. 41. Statistical analysis of *Lung_ipsilat* structure DVH curve values: a) histogram of values; b) boxplot

Figure 41 shows the DVH curve results for the *Lung_ipsilat* structure. As indicated in Figure 41 a), the lowest DVH curve value is 14.39%, and the greatest is 15.75%, also mean value and standard deviation (σ) are shown. The boxplot is shown in Figure 41 b). The boxplot has one outlier (6th plan value), and the median and mean values are nearly identical. The mean value is 14.50%, while the standard error is 0.09%. The median value is 14.40%, with a standard deviation of 0.35%, a minimum of 14.39%, a maximum of 15.75%, and a range of 1.36%.

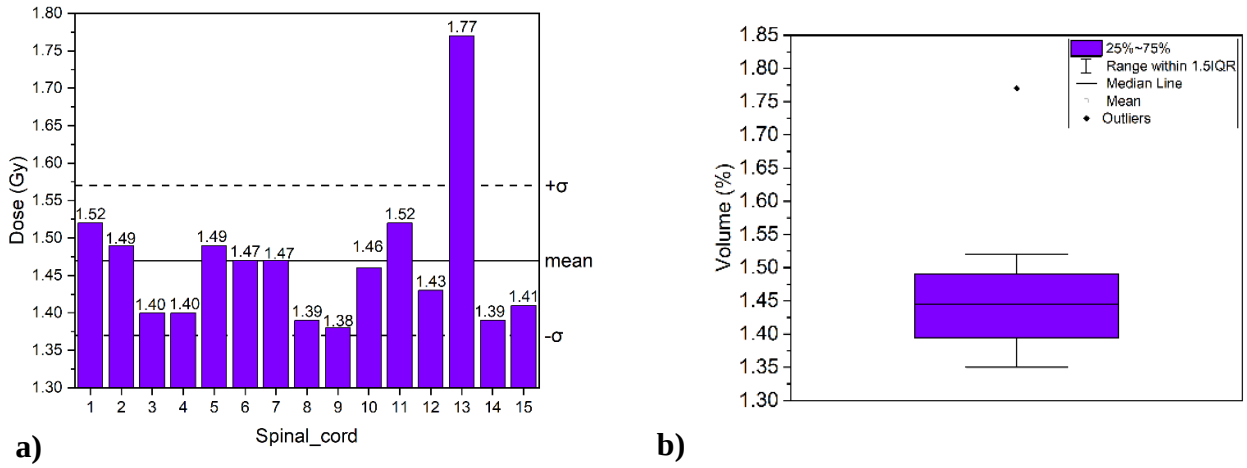

Fig. 42. Statistical analysis of *Spinal_cord* structure DVH curve values: a) histogram of values; b) boxplot

Figure 42 shows the DVH curve values for the *Spinal_cord* structure. As shown in Figure 42 a), the lowest DVH curve value is 1.38 Gy, and the greatest is 1.77 Gy, also mean value and standard deviation (σ) are shown. The boxplot is shown in Figure 42 b). The boxplot has one outlier (13th plan value), and the median and mean values are nearly equal. The mean value is 1.47 Gy, while the standard error is 0.03 Gy. The median value is 1.46 Gy, with a standard deviation of 0.10 Gy, a minimum of 1.38 Gy, a maximum of 1.77 Gy, and a range of 0.39 Gy.

At the end of the work, an attempt was made to develop mathematical models of *PTV_WB_dvh*, *Heart*, *Lung_ipsilat*, and *Spinal_cord* for their covered volume (dose) and structure volume relationship. The results are shown in Figure 43.

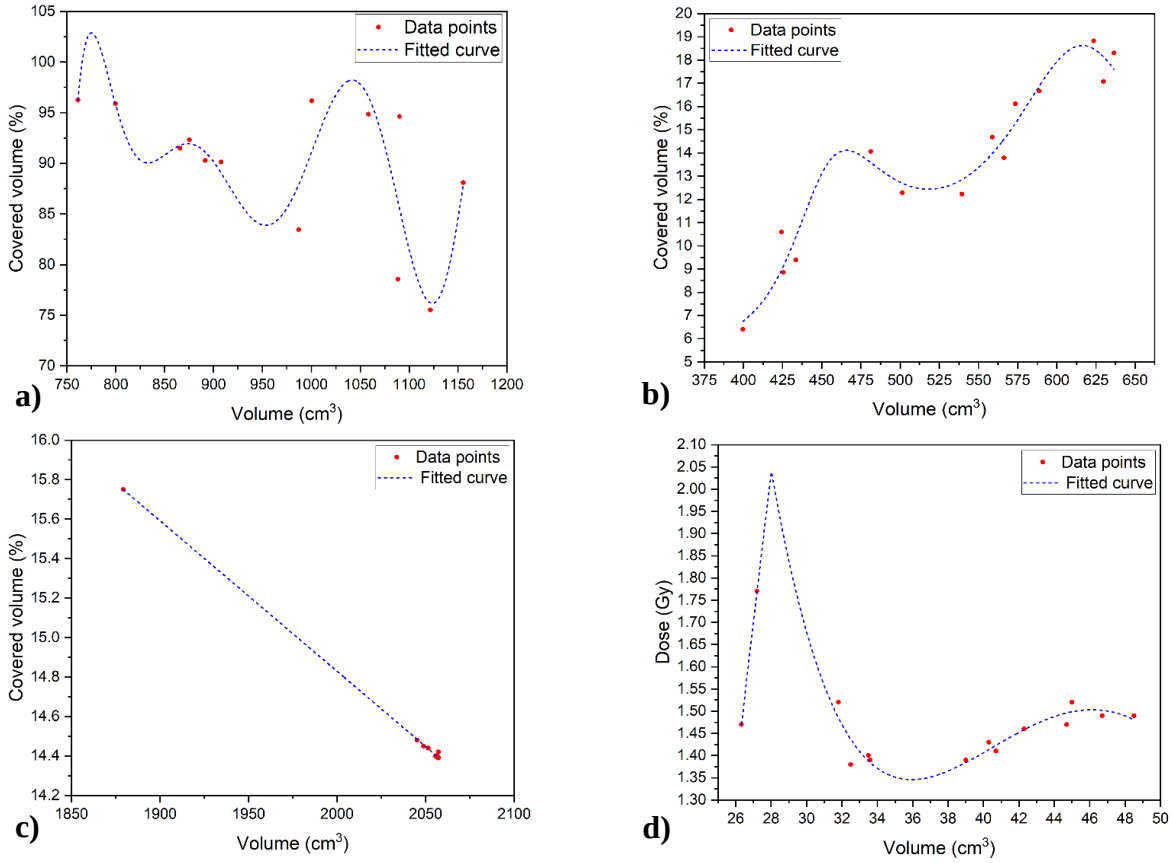

Fig. 43. Clinical goal value dependence on structure volume: a) *PTV_WB_dvh* structure; b) *Heart* structure; c) *Lung_ipsilat* structure; d) *Spinal_cord* structure. Red dots mean data points, and blue dotted line fitted curve

Mathematical models were developed using the "Origin 2021b" program to evaluate the dependence of clinical targets on structure volume. The dependence of the covered *PTV_WB_dvh* volume on the structure volume is found to be an 8-order polynomial [112], the dependence of the covered *Heart* volume on the structure volume is an inverse polynomial with centre [113], the dependence of the covered *Lung_ipsilat* volume on the structure volume is linear [114], *Spinal_cord* dose dependence on structure volume is the Chesler-Cram Peak Function [115].

The *PTV_WB_dvh* structure model is given by formula 42:

$$y = \sum_{i=0}^{8} a_i x^i \tag{42}$$

where – $a_0 = -1.115 \cdot 10^8$, $a_1 = 9.441 \cdot 10^5$, $a_2 = -3.458 \cdot 10^3$, $a_3 = 7.327 \cdot 10^0$, $a_4 = -9.590 \cdot 10^{-3}$, $a_5 = 8.011 \cdot 10^{-6}$, $a_6 = -4.167 \cdot 10^{-9}$, $a_7 = 1.234 \cdot 10^{-12}$, $a_8 = -1.593 \cdot 10^{-16}$.

The *Heart* structure equation is given by formula 43:

$$y = y_0 + \frac{A}{1 + \sum_{i=0}^{3} A_i \left(2\frac{x - x_c}{\omega}\right)^{2i}} \tag{43}$$

where – $y_0 = 5.333$, $x_c = 616.418$, $\omega = 259.374$, $A = 13.2824$, $A_1 = 3.527$, $A_2 = -4.374$, $A_3 = 1.513$.

The *Lung_ipsilat* structure mathematical model is given by formula 44:

$$y = A + bx \tag{44}$$

where – $A = 30.0862$, $B = -0.0076$.

The *Spinal_cord* structure equation is given in formula 45:

$$y = y_0 + Ae^{-\frac{0.5(x - x_{c_1})}{\omega}} + AB\left(1 - 0.5\left(1 - \tanh\left(k_2(x - x_{c_2})\right)\right)\right)e^{-0.5k_3}\left(\left|x - x_{c_3}\right| + \left(x - x_{c_3}\right)\right) \tag{45}$$

where – $y_0 = -22.931$, $x_{c_1} = 51.373$, $\omega = 1.369 \cdot 10^3$, $A = 23.757$, $k_2 = -4.338 \cdot 10^4$, $x_{c_1} = 8.885 \cdot 10^4$, $B = 0.232$, $k_3 = 0.099$, $x_{c_3} = 27.923$.

The R^2 (coefficient of determination) criterion was chosen to evaluate the mathematical models. According to Corporate Finance Institute: "R^2 is a statistical measure in a regression model that determines the proportion of variance in the dependent variable that can be explained by the independent variable" [116]. The evaluation of the regression model is based on the R^2 value:

- "if the R^2 value < 0.3, this value is generally considered a none or very weak effect size" [117];
- "if the R^2 value 0.3 < R^2< 0.5, this value is generally considered a weak or low effect size" [117];
- "if the R^2 value 0.5 < R^2< 0.7, this value is generally considered a moderate effect size" [117];
- "if the R^2 value > 0.7, this value is generally considered a strong effect size" [117].

The model value of the *PTV_WB_dvh* structure was found to be R^2=0.6504, indicating that the relationship between the data and the model is moderate. In the case of *Heart*, *Lung_ipsilat*, and *Spinal_cord*, a strong association of the model to the initial data is obtained, with values of 0.9511, 0.9994 (0.9049 if 6 plan point is deleted), and 0.9478, respectively.

PTV_WB_dvh covered volume values varied from 75.53% to 97.95%, *Heart* values ranged from 6.35% to 18.31%, *Lung_ipsilat* values ranged from 14.39% to 15.75%, and *Spinal_cord* dosage values ranged from 1.35 Gy to 1.77 Gy after analysis of clinical targets. *PTV_WB_dvh* volume dependence on structure volume is found to be an 8-order polynomial (R^2=0.6504), covered *Heart* volume dependence on structure volume is an inverse polynomial with centre (R^2=0.9511), covered *Lung_ipsilat* volume dependence on structure volume is linear (R^2=0.9994), and *Spinal_cord* dose dependence on structure volume is Chesler-Cram Peak Function (R^2=0.9478).

Conclusions

1. Segmentation process for different radiation-oncologists delineated structures in computed tomography images was performed using secondary commercial applications – "Crop IMAGE", "Adobe Photoshop 2020". It was found that the threshold value used by the treatment planning system "Eclipse" is set to be in the range of 0.2-0.4 a. u., due to this reason threshold value of 0.4 a. u. was selected for use with "EvaluateSegmentation" software calculating similarity values of different structures. The commercial "Eclipse" program is limited by evaluation of one similarity coefficient (Dice), while with open-source software "EvaluateSegmentation" could be analysed 20 different similarity coefficients which create more detailed study of delineated structures.
2. Using the "Eclipse" and the "EvaluateSegmentation" programs, the similarity characteristics of *CTV_WB* and *PTV_WB* structures between the plans developed by different radiation-oncologists and the reference plan were analysed. It was observed that the DICE coefficient differed as follows: *CTV_WB* (0.880 – 0.960 a. u. ("EvaluateSegmentation") | 0.910 – 0.970 a. u. ("Eclipse")), *PTV_WB* (0.860 – 0.960 a. u. ("EvaluateSegmentation") | 0.860 – 0.960 a. u. ("Eclipse")). Comparing the results of the "Eclipse" and the "EvaluateSegmentation" of the *CTV_WB* and *PTV_WB* structures, it can be seen that the mean value of *CTV_WB* differs by 0.003 a. u., and the median is the same in the case of *PTV_WB* the mean and median values are identical, so with the "EvaluateSegmentation" software, reliable results are obtained. Additionally using an open-source "EvaluateSegmentation" software it is possible to calculate Jaccard Coefficient, the area under ROC Curve, Cohen Kappa, Rand Index, and Adjusted Rand Index.
3. Clinical structures volumes using the treatment planning system "Eclipse" were evaluated, it was found that *CTV_WB* volume was 641 – 834 cm^3 (reference plan value – 723 cm^3), the volume value of *PTV_WB* was 934.4 – 1381.4 cm^3 (reference plan value – 1052 cm^3), and the volume value of *PTV_WB_dvh* was 761.4 – 908.3 cm^3 (reference plan value – 824.4 cm^3). The difference between the volumes of *CTV_WB* and *PTV_WB* can be explained by the *PTV/CTV* ratio, when the value of this ratio is close to 1.45 a. u., structures are defined according to the recommendations of ESTRO (the margin between *PTV* and *CTV* is 0.5 cm), during the work it is estimated that this ratio is 1.34 – 1.85 a. u. The volume value of the *Heart* was 399.7 – 636.5 cm^3 (the value of the reference plan – 626.5 cm^3), the volume value of *Lung_ipsilat* was 1879.4 – 2057.3 cm^3 (the mean value – 2043.1 cm^3) and the volume value of *Spinal_cord* was 26.3 – 48.5 cm^3 (the mean value 37.7 cm^3). Differences in the volume values can be explained by the human factor, as each radiation-oncologists defining structures sees them differently.
4. The main dosimetry data of planned treatment plans for the different volumes were investigated, it was found that *PTV_WB_dvh* covered volume values were 75.30 – 96.18% (clinical target – $V24.70 \geq 95\%$), covered volume dependence on structure volume is found to be an 8-order polynomial (R^2=0.6504). *Heart* volume values were 6.35 – 18.31% (clinical goal – V1.50 <30%), covered *Heart* volume dependence is an inverse polynomial with centre (R^2=0.9511). *Lung_ipsilat* covered volume values were 14.39 – 15.75% (clinical goal – V8.00 <15%), covered *Lung_ipsilat* volume dependence is linear (R^2=0.9994). The dose received by *Spinal_cord* were 1.38 – 1.77 Gy (clinical goal – D_{max} < 23.64 Gy), dose dependence is Chesler-Cram Peak Function (R^2=0.9478). Such a difference in the values of *PTV_WB_dvh* could be explained by the different initial volumes of *PTV_WB_dvh* (761.4 – 1155.5 cm^3) as well as the different ratio of *PTV/PTV_dvh* (1.00 – 1.52 a. u.).

Acknowledgement

Thank you to the head of the Oncology and Hematology Clinic of Kaunas Clinics Lithuanian University of Health Sciences, prof. dr. Elona Juozaitytė, for the opportunity to use the infrastructure of the Radiation Therapy Department of the Oncology Hospital, Lithuanian University of Health Sciences. The head of the Radiation Therapy Department, Kaunas Clinic of Oncology and Hematology, Lithuanian University of Health Sciences, a radiation-oncologist, dr. Laimonas Jaruševičius for the access to patient data and results. An radiation-oncologist at the Radiotherapy Department of the Oncology and Hematology Department of Kaunas Clinics of the Lithuanian University of Health Sciences, dr. Evelina Koleibnikova, for the reference plan structures, developed together with dr. Laimonas Jaruševičius. All the radiation-oncologists from the Department of Radiation Therapy, Kaunas Clinic of Oncology and Hematology, Lithuanian University of Health Sciences, and Department of Radiation Therapy, Oncology Hospital, Lithuanian University of Health Sciences, created patient structures during the practical task. Thank you to cousin Augustė Gitaitytė for help with English philology stuff. Many thanks to a medical physicist in the Radiation Therapy Department of the Oncology Hospital of the Lithuanian University of Health Sciences and an associated professor at the Kaunas University of Technology, dr. Jurgita Laurikaitienė, for consultations and help preparing the final master's thesis.

List of references

1. POORTMANS P. M.P., et al. Winter is over: The use of Artificial Intelligence to individualise radiation therapy for breast cancer. *The Breast* [online]. The Breast. February 2020, vol. **49**, 194-200 [viewed 15 March 2022]. Available from: doi: 10.1016/j.breast.2019.11.011
2. VAASSEN F. et al. Evaluation of measures for assessing time-saving of automatic organ-at-risk segmentation in radiotherapy. *Physics and Imaging in Radiation Oncology* [online]. PhiRO. January 2020, vol. **13**, 1-6 [viewed 15 March 2022]. Available from: doi: 10.1016/j.phro.2019.12.001
3. OUTEIRA R., et al. Oropharyngeal primary tumor segmentation for radiotherapy planning on magnetic resonance imaging using deep learning. *Physics and Imaging in Radiation Oncology* [online]. PhiRO. July 2021, vol. **19**, 39-44 [viewed 15 March 2022]. Available from: doi: 10.1016/j.phro.2021.06.005
4. JEFFERIES S, TAYLOR A, REZNEK R. Results of a national survey of radiotherapy planning and delivery in the UK in 2007. *Clinical Oncology* [online]. Clin Oncol. April 2009, vol. **21**(3), 204-217 [viewed 17 March 2022]. Available from: doi: 10.1016/j.clon.2008.11.017
5. BATUMALAI V., et al. Interobserver variability in clinical target volume delineation in tangential breast irradiation: a comparison between radiation oncologists and radiation therapists. *Clinical Oncology* [online]. Clin Oncol. March 2011, vol. **23**(2), 108-113 [viewed 17 March 2022]. Available from: doi: 10.1016/j.clon.2010.10.004
6. CASTRO PENA P. et al., Anatomical, clinical, and radiological delineation of target volumes in breast cancer radiotherapy planning: individual variability, questions, and answers. *The British Journal of Radiology* [online]. Br J Radiol. July 2009, vol. **82**(576), 595-59 [viewed 17 March 2022]. Available from: doi: 10.1259/bjr/96865511
7. LANDIS DM, et al. Variability among breast radiation oncologists in the delineation of the postsurgical lumpectomy cavity. *International journal of radiation oncology, biology, physics* [online]. Int J Radiat Oncol Biol Phys. April 2007 vol. **67**(5), 1299–1308 [viewed 15 March 2022]. Available from: doi: 10.1016/j.ijrobp.2006.11.026
8. HURKMANS CW., et al. Variability in target volume delineation on CT scans of the breast. *International journal of radiation oncology, biology, physics* [online]. Int J Radiat Oncol Biol Phys. August 2001, vol. **50**(5), 1366–1372 [viewed 15 March 2022]. Available from: doi: 10.1016/s0360-3016(01)01635-2
9. WONG EK, et al. Consistency in seroma contouring for partial breast radiotherapy: impact of guidelines. *International journal of radiation oncology, biology, physics* [online]. Int J Radiat Oncol Biol Phys. October 2006, vol. **66**(2), 372–376 [viewed 15 March 2022]. Available from: doi: 10.1016/j.ijrobp.2006.05.066
10. PITKANEN MA, et al. Quality assurance in radiotherapy of breast cancer--variability in planning target volume delineation. *Acta Oncologica* [online]. Acta Oncol. July 2009, vol. **40**(1), 50-55 [viewed 15 March 2022]. Available from: doi: 10.1080/028418601750071055
11. SANDERS KE, KOMAKI R, BUCHHOLZ TA. Target delineation and treatment planning in breast conserving therapy. *Rays* [online]. Rays. September 2003, vol. **28**(3), 237–245 [viewed 15 March 2022]. Access from: https://tinyurl.com/azusftdk
12. STRUIKMANS H., et al. Interobserver variability of clinical target volume delineation of glandular breast tissue and of boost volume in tangential breast irradiation. *Radiotherapy and Oncology* [online]. Radiother Oncol. September 2005, vol. **76**(3), 293–299 [viewed 15 March 2022]. Available from: doi: 10.1016/j.radonc.2005.03.029

13. PETERSEN RP, et al. Target volume delineation for partial breast radiotherapy planning: clinical characteristics associated with low interobserver concordance. *International journal of radiation oncology, biology, physics* [online]. Int J Radiat Oncol Biol Phys. September 2007, vol. **69**(1), 41–48 [viewed 15 March 2022]. Available from: doi: 10.1016/j.ijrobp.2007.01.070
14. STIEB. S. et al. Imaging for Target Delineation and Treatment Planning in Radiation Oncology. *Hematology/Oncology Clinics of North America* [online]. Hematol Oncol Clin N Am. December 2019, vol. **33**, 963–975 [viewed 15 March 2022]. Available from: doi: 10.1016/j.hoc.2019.08.008
15. WORLD HEALTH ORGANISATION: *Lithuania Source: Globocan 2020* [interactive]. 2021 [viewed 03 February 2022]. Access via: https://tinyurl.com/yckpfe7j
16. GAIDELYTĖ R., GARBUVIENĖ M., ZAVACKAITĖ A., Health Statistics of Lithuania 2017. Vilnius, 2018. ISSN 1648-0899.
17. GAIDELYTĖ R., GARBUVIENĖ M., ZAVACKAITĖ A., Health Statistics of Lithuania 2018. Vilnius, 2019. ISSN 1648-0899.
18. WORLD CANCER RESEARCH FUND: *Worldwide cancer data* [interactive]. 2021 [viewed 03 February 2022]. Access via: https://tinyurl.com/WCRFI
19. WORLD HEALTH ORGANISATION: *Cancer: Key Facts* [interactive]. 2022 [viewed 03 February 2022]. Access via: https://tinyurl.com/mkbyntw9
20. SKUČAITĖ, A, et al. Actuarial Analysis of Survival among Breast Cancer Patients in Lithuania. *Journal of Healthcare* [online]. MDPI, April 2021, vol. **383**(9) [viewed 03 February 2022]. Available from: doi: 10.3390/healthcare9040383
21. ABDUL HALIM, A. A., et al. Existing and Emerging Breast Cancer Detection Technologies and Its Challenges: A Review. *Journal of applied sciences* [online]. Appl. Sci. November 2021, vol. ***11***(22), 10753 [viewed 03 February 2022]. Available from: doi: 10.3390/app112210753
22. AKRAM, M., et al. Awareness and current knowledge of breast cancer. *Journal of biological research* [online]. Biol Res, October 2017, vol. **50**(1), 33 [viewed 03 February 2022]. Available from: doi: 10.1186/s40659-017-0140-9
23. BICK, U. et al. Image-guided breast biopsy and localisation: recommendations for information to women and referring physicians by the European Society of Breast Imaging. *Journal of insights into imaging* [online]. Springer Open, December 2020, vol. **11**(1), 12 [viewed 03 February 2022]. Available from: doi: 10.1186/s13244-019-0803-x
24. NAKAHARA H., et al., Extension of breast cancer: comparison of CT and MRI. Radiat Med. 2002, **20**(1):17-23. ISSN 0288-2043.
25. TRUONG, M. T., et al., Brachial Plexus Contouring with CT and MR Imaging in Radiation Therapy Planning for Head and Neck Cancer. *Journal of radiographics* [online]. RadioGraphics, July 2010, vol. **30**(4), 1095-1003 [viewed 04 February 2022]. Available from: doi: 10.1148/rg.304095105
26. KUAN, L. M. *Dr Lim Siew Kuan from Mount Elizabeth Novena Hospital discusses what to expect when you are sent for a breast biopsy, what type of breast biopsy you may undergo and what to expect during recovery* [interactive]. Health+, 2021 [viewed 04 February 2022]. Access via: https://tinyurl.com/2p8rx6107
27. KRŪTIES VĖŽYS: *Krūties vėžio gydymo metodai* [interactive]. 2022 [viewed 04 February 2022]. Access via: https://tinyurl.com/3e6hnjhv
28. KARPF, D., et al. Left breast irradiation with tangential intensity-modulated radiotherapy (t-IMRT) versus tangential volumetric modulated arc therapy (t-VMAT): trade-offs between secondary cancer induction risk and optimal target coverage. *Journal of radiation oncology*

[online]. Radiat Oncol, September 2019, vol. **156**(14), [viewed 04 February 2022]. Available from: doi: 10.1186/s13014-019-1363-4
29. TAYLOR, A., & POWELL, M. E., Intensity-modulated radiotherapy--what is it? *Journal of cancer imaging* [online]. Cancer imaging: the official publication of the International Cancer Imaging Society, March 2004, vol. **4**(2) 68-7, [viewed 04 February 2022]. Available from: doi: 10.1102/1470-7330.2004.0003
30. BUWENGE, M., et al., Intensity-modulated radiation therapy for breast cancer: current perspectives. *Journal of breast cancer* [online]. Dove Medical Press, March 2017, vol. **9**, 121–126, [viewed 04 February 2022]. Available from: doi: 10.2147/BCTT.S113025
31. ONCO-RADIOTHERAPY MEDICAL INSTITUTE: *VMAT (Volumetric Modulated Arc Therapy)* [interactive]. 2022 [viewed 04 February 2022]. Access via: https://tinyurl.com/53yyv7f8
32. CLEVELAND CLINIC: *Volumetric Modulated Arc Therapy (VMAT)* [interactive]. 2022 [viewed 04 February 2022]. Access via: https://tinyurl.com/bdephtph
33. NGUYEN, B.T., et al., Optimising the dosimetric quality and efficiency of post-prostatectomy radiotherapy: A planning study comparing the performance of volumetric-modulated arc therapy (VMAT) with an optimised seven-field intensity-modulated radiotherapy (IMRT) technique. *Journal of Medical Imaging and Radiation Oncology* [online]. Wiley online library, April 2012, vol. **2**(56), 211-219), [viewed 04 February 2022]. Available from: doi: 10.1111/j.1754-9485.2011.02324.x
34. STONY BROOKS CANCER CENTER: *Respiratory Gating and Deep Inspiration Breath Hold (DIBH)* [interactive]. 2021 [viewed 04 February 2022]. Access via: https://tinyurl.com/2p8nckxk
35. KRENGLI, M., et al., Prone versus supine position for adjuvant breast radiotherapy: a prospective study in patients with pendulous breasts. Journal of radiation oncology [online]. NCBI, October 2013, vol. **8**, 232, [viewed 04 February 2022]. Available from: doi: 10.1186/1748-717X-8-232
36. COOPERMAN BARNABAS MEDICAL CENTER: *Prone Positioning for Breast Cancer Treatment* [interactive]. 2022 [viewed 04 February 2022]. Access via: https://tinyurl.com/2p9bpxzk
37. BOUTE B., et al., Potential benefits of crawl position for prone radiation therapy in breast cancer. *Journal of Applied Clinical Medical Physics* [online]. American Association of Physicists in Medicine, June 2017, vol. **4**(18), 200–205, [viewed 04 February 2022]. Available from: doi: 10.1002/acm2.12118
38. BIRGITTE V., et al., ESTRO consensus guideline on target volume delineation for elective radiation therapy of early-stage breast cancer. Journal of radiotherapy and oncology [online]. ScienceDirect, January 2015, vol. **1**(114), 3-10, [viewed 04 February 2022]. Available from: doi: 10.1016/j.radonc.2014.11.030
39. INTERNATIONAL COMMISSION ON RADIATION UNITS & MEASUREMENTS: *ICRU Report 50, Prescribing, Recording, and Reporting Photon Beam Therapy* [interactive]. 2022 [viewed 04 February 2022]. Access via: https://tinyurl.com/yhfjmc43
40. BERTHELSEN A. K., et al., What's new in target volume definition for radiologists in ICRU Report 71? How can the ICRU volume definitions be integrated into clinical practice? *Journal of cancer imaging* [online]. Cancer Imaging, April 2007, vol. **7**, 104-116, [viewed 04 February 2022]. Available from: doi: 10.1102/1470-7330.2007.00
41. REIFF J. E.: *Internal Target Volume (ITV)*. Encyclopedia of Radiation Oncology [online]. Springer, 2013, [viewed 04 February 2022]. Available from: doi: 10.1007/978-3-540-85516-3_761

42. BURNET N. G. et al., Defining the tumour and target volumes for radiotherapy. *Journal of cancer imaging* [online]. Cancer Imaging, July 2004, vol. **4**, 153-161, [viewed 04 February 2022]. Available from: doi: 10.1102/1470-7330.2004.0054
43. LUO, J., et al., Does the protocol-required uniform margin around the CTV adequately account for setup inaccuracies in whole breast irradiation? *Journal of radiation oncology* [online]. Radiat Oncol, August 2021, vol. **143**(16), [viewed 04 February 2022]. Available from: doi: 10.1186/s13014-021-01863-w
44. MOHAMED, R., et al., A retrospective comparison of two different immobilization systems for radiotherapy of extremity soft tissue sarcomas and its influence on CTV-PTV margin. *Journal of the Egyptian National Cancer Institute* [online]. J Egypt Natl Canc Inst, September 2021, vol. **33**, 27, [viewed 04 February 2022]. Available from: doi: 10.1186/s43046-021-00076-2
45. IAEA: *Optimization in external beam radiotherapy* [interactive]. 2022 [viewed 04 February 2022]. Access via: https://tinyurl.com/m108jvxpk
46. HYSING LB, et al., Planning organ at risk volume margins for organ motion of the intestine. *Journal of radiotherapy and oncology* [online]. Radiother Oncol, September 2006, vol. **80**(3), 349-54, [viewed 04 February 2022]. Available from: doi: 10.1016/j.radonc.2006.07.039
47. CANCER QUEST: *Radiation Therapy* [interactive]. 2022 [viewed 04 February 2022]. Access via: https://tinyurl.com/bdeccf6j
48. RXLIST: *Definition of Ipsilateral* [interactive]. 2021 [viewed 18 February 2022]. Access via: https://tinyurl.com/4hyz2u8c
49. NATIONAL INSTITUTE FOR HEALTH RESEARCH CLINICAL RESEARCH NETWORK: *FAST-Forward Randomised clinical trial testing a 1-week course of curative whole breast radiotherapy against a standard 3-week schedule in terms of local cancer control and late adverse effects in patients with early breast cancer* [interactive]. 2018 [viewed 04 February 2022]. Access via: https://tinyurl.com/hue5zbjj
50. AJITHKUMAR TV, Principles of radiotherapy. From: Specialist Training in Oncology [interactive]. Mosby, 2011, pp. 15-29. ISBN 9780723434580. Access via: doi: 10.1016/B978-0-7234-3458-0.00008-7
51. HASSON B. F.: *Dose Volume Histogram (DVH)*. Encyclopedia of Radiation Oncology [online]. Springer, 2013, [viewed 04 February 2022]. Available from: doi: 10.1007/978-3-540-85516-3_659
52. SHARKEY K. and SELVARAJ J.: Dose-Volume Histogram Calculation in Radiotherapy Treatment Plans Using VTK [interactive]. 2012 [viewed 04 February 2022]. Access via: https://tinyurl.com/22tnnamr
53. KOTETISHVILI, K., et al., Compatision between volumetric modulated arc therapy (VMAT) and 3D tangential beams technique used in patients with breast cancer. *International Journal of Applied Electromagnetics and Mechanics* [online]. JAE, 2019, vol. **11**(21), [viewed 04 February 2022]. Available from: https://tinyurl.com/yckvp7h9
54. DRZYMALA, R.E. et al, Dose-volume histograms. International Journal of Radiation Oncology*Biology*Physics [online]. ScienceDirect, May 1991, vol. **1**(21), 71-78, [viewed 04 February 2022]. Available from: doi: 10.1016/0360-3016(91)90168-4
55. NIH: *Computed Tomography (CT)* [interactive]. 2022 [viewed 04 February 2022]. Access via: https://tinyurl.com/5axxw7p8
56. AGAHI A.: *CT scan* [interactive]. 2022 [viewed 04 February 2022]. Access via: https://tinyurl.com/2kw289ry

57. RADIOLOGYINFO.ORG: Computed Tomography [interactive]. 2022 [viewed 04 February 2022]. Access via: https://tinyurl.com/2p9hetut
58. CALDEMEYER KS, BUCKWALTER KA. The basic principles of computed tomography and magnetic resonance imaging. Journal of the American Academy of Dermatology [online]. J Am Acad Dermatol, November 1999, vol. **5**(41), 768-771, [viewed 04 February 2022]. Available from: doi: 10.1016/s0190-9622(99)70015-0
59. BELL D. J: *Computed tomography.* Reference article, Radiopaedia.org. [interactive]. 2021 [viewed 04 February 2022]. Available from: doi: 10.53347/rID-9027
60. GREENWAY K.: *Hounsfield unit formula*. Case study, Radiopaedia.org. [interactive]. 2021 [viewed 04 February 2022]. Available from: doi: 10.53347/rID-38096
61. LAWTON, T., DSCImageCalc – Software for Determining Similarity Coefficients for the Analysis of Image Segmentations. *Journal of Open Research Software* [online]. Open research software, October 2017, vol. **1**(5), p. 28, [viewed 04 February 2022]. Available from: doi: 10.5334/jors.16
62. TAHA, A.A., HANBURY, A. Metrics for evaluating 3D medical image segmentation: analysis, selection, and tool. *BMC Medical Imaging* [online]. BMC Med Imaging, August 2015, vol. **15**(29), [viewed 04 February 2022]. Available from: doi: 10.1186/s12880-015-0068-x
63. NATARAJAN, P., et al., Tumour detection using threshold operation in MRI brain image. In: IEEE International Conference on Computational Intelligence and Computing Research (ICCIC). Coimbatore, India, 2012, 1-4 p. [viewed 04 February 2022]. Available from: doi: 10.1109/ICCIC.2012.6510299
64. UMIT I., AHMET I, Brain tumour segmentation based on a new threshold approach. In: Journal of procedia computer science: selected per reviewed paper from 9th International Conference on Theory and Application of Soft Computing, Computing with Words and Perception, ICSCCW 2017, 22-23 August 2017, Budapest, Hungary. vol. **120**, 580-587, Available from: 10.1016/j.procs.2017.11.282
65. PANDIAN, DS, et al., Complex threshold method for identifying pixels that contain predominantly noise in magnetic resonance images. *Journal of Magnetic Resonance Imaging* [online]. J Magn Reson Imaging, September 2008, vol. **3**(28), 727-35, [viewed 04 February 2022]. Available from: doi: 10.1002/jmri.21487
66. SAFARI, S., et al., Evidence-Based Emergency Medicine Part 2: Positive and negative predictive values of diagnostic tests. Journal of emergency. Emergency, July 2015, **3**(3), 87–88, viewed 04 February 2022]. Available from: https://tinyurl.com/3b3cr295
67. MODERN STATISTICAL METHODS FOR PSYCHOLOGY: *Decision Errors* [interactive]. 2021 [viewed 04 February 2022]. Access via: https://tinyurl.com/yck68ex8
68. ALLEYDOG.COM: *Decision Errors* [interactive]. 2022 [viewed 04 February 2022]. Access via: https://tinyurl.com/2p9evcvx
69. GEEKFORGEEKS: *Difference between Lossy Compression and Lossless Compression* [interactive]. 2020 [viewed 04 February 2022]. Access via: https://tinyurl.com/yckscpav
70. BROOKES T.: *Lossy vs Lossless Compression: What's the Difference?* [interactive]. 2021 [viewed 04 February 2022]. Access via: https://tinyurl.com/2p88bemk
71. FILEINFO.COM: *.JPG File Extension* [interactive]. 2020 [viewed 04 February 2022]. Access via: https://tinyurl.com/56za4457
72. BRITANNICA.COM: *Raster graphics* [interactive]. 2022 [viewed 04 February 2022]. Access via: https://tinyurl.com/umjfjxfc

73. FILEFORMAT: Documentation [interactive]. 2022 [viewed 04 February 2022]. Access via: https://tinyurl.com/4kjf2pxc
74. FILEINFO.COM: *.DICOM File Extension* [interactive]. 2020 [viewed 04 February 2022]. Access via: https://tinyurl.com/2p947ew6
75. BARASKAR, T. N., & MANKAR, V. R. The DICOM Image Compression and Patient Data Integration using Run Length and Huffman Encoder. In S. Radhakrishnan, & M. Sarfraz (Eds.), Coding Theory. IntechOpen, 2019, [viewed 04 February 2022]. Available from: doi: 10.5772/intechopen.89143
76. VARMA D. R. Managing DICOM images: Tips and tricks for the radiologist. The Indian Journal of Radiology & Imaging [online]. NCBI, January-March 2012, vol. **22**(1), 4–13, [viewed 04 February 2022]. Available from: doi: 10.4103/0971-3026.953
77. *Lietuvos Respublikos biomedicininių tyrimų etikos įstatymas.* 2000 m. gegužės 11 d. Nr. VIII-1679. (2000). [viewed 18 February 2022]. Access via: https://tinyurl.com/2p8e2are
78. MERRIAM-WEBSTER: *contralateral* [interactive]. 2021 [viewed 18 February 2022]. Access via: https://tinyurl.com/24jxu29z
79. GE HEALTHCARE: *510(k) summary of safety and effectiveness* [interactive]. 2008 [viewed 18 February 2022]. Access via: https://tinyurl.com/5n6z6985
80. ALM MEDICAL: *CT scanner GE LightSpeed RT16* [interactive]. 2018 [viewed 18 February 2022]. Access via: https://almmedical.com/product/ge-lightspeed-rt-16-slice-ct-scanner/
81. MEDALLION MEDICAL TECHNOLOGIES: *CT Solutions* [interactive]. 2018 [viewed 18 February 2022]. Access via: https://tinyurl.com/ycktd6tn
82. VARIAN: *Eclipse* [interactive]. 2022 [viewed 18 February 2022]. Access via: https://tinyurl.com/2p92m22t
83. I LOVE IMG: *crop image* [interactive]. 2022 [viewed 18 February 2022]. Access via: https://tinyurl.com/ys393u83
84. PHOTOSHOP ESSENTIALS: *The Magic Wand Tool In Photoshop* [interactive]. 2022 [viewed 18 February 2022]. Access via: https://tinyurl.com/yeyush8y
85. EVALUATESEGMENTATION TOOL, VISCERAL. Developed by Abdel Aziz Taha 24.02.2013. Copyright 2013 Vienna University of Technology Institute of Software Technology and Interactive Systems
86. VISCERAL: *EvaluateSegmentation Software* [interactive]. 2017 [viewed 18 February 2022]. Access via: https://tinyurl.com/2p83nf62
87. TECH TARGET: *command-line interface (CLI)* [interactive]. 2022 [viewed 18 February 2022]. Access via: https://tinyurl.com/2p8k6tnp
88. HANBURY A. et al. Cloud-Based Benchmarking of Medical Image Analysis, *Evaluation Metrics for Medical Organ Segmentation and Lesion Detection*, 2017, pp. 87 - 105.
89. THE FREE DICTIONARY: *tuple* [interactive]. 2016 [viewed 18 February 2022]. Access via: https://tinyurl.com/2ecnjvvs
90. F. GALTON, Dice for Statistical Experiments. *Nature* [online]. Nature, May 1890, vol. **42**, 13–14. [viewed 18 February 2022]. Available from: doi: 10.1038/042013a0
91. K. ZOU et al., Statistical validation of image segmentation quality based on a spatial overlap index. *Radiology Alliance for Health Services Research* [online]. Academic radiology, February 2004, **11**(2), 178–189. Available from: doi: 10.1016/S1076-6332(03)00671-8
92. VARIAN MEDICAL SYSTEMS, *Halcyon* [interactive]. 2017 [viewed 21 March 2022]. Access via: https://tinyurl.com/mubnxaww

93. VARIAN, *Halcyon* [interactive]. 2017 [viewed 21 March 2022]. Access via: https://tinyurl.com/3wcsjjrc
94. PATHAK PK., et al., Commissioning and quality assurance of HalcyonTM 2.0 linear accelerator. Reports of practical Oncology and radiotherapy [online]. Rep Pract Oncol Radiother. June 2021, vol. 26(3), 433–444. [viewed 21 March 2022]. Available from: doi: 10.5603/RPOR.a2021.0065
95. BEACON HOSPITAL, *Varian Halcyon™ Radiotherapy* [interactive]. 2017 [viewed 21 March 2022]. Access via: https://tinyurl.com/5y6us998
96. VARIAN, *Eclipse™ Treatment Planning Software from Varian Medical Systems Named a "Category Leader" in the 2014 "Best in KLAS: Software and Services Report"* [interactive]. 2015 [viewed 21 March 2022]. Access via: https://tinyurl.com/2v93rk5d
97. MURRAY BRUNT A., et al., Hypofractionated breast radiotherapy for 1 week versus 3 weeks (FAST-Forward): 5-year efficacy and late normal tissue effects results from a multicentre, non-inferiority, randomised, phase 3 trial. *The Lancet* [online]. Academic The Lancet, May 2020, vol. **395**(10237), 1613–1626. [viewed 18 February 2022]. Available from: doi: 10.1016/s0140-6736(20)3093
98. YOSHIMURA, ONO Y., et al. Appropriate margin for planning target volume for breast radiotherapy during deep inspiration breath-hold by variance component analysis. *Radiation Oncology* [online]. Radiat Oncol, March 2021, vol. **16**(49). [viewed 18 March 2022]. Available from: doi: 10.1186/s13014-021-01777-7
99. YU, S. et al. Deep Inspiration Breath Hold Provides Fewer Set-up Errors Compared with Free Breathing for Whole-Breast Radiation. *International Journal of Radiation Oncology, Biology, Physics* [online]. Int J Radiat Oncol Biol Phys. September 2019, vol. **1**(105), E37 - E38 [viewed 15 March 2022]. Available from: doi: 10.1016/j.ijrobp.2019.06.702
100. CARMEN B. et al. Deep Inspiration Breath Hold: Techniques and Advantages for Cardiac Sparing During Breast Cancer Irradiation. *Frontiers in Oncology* [online]. Front. Oncol. April 2018, vol. **8**. [viewed 15 March 2022]. Available from: doi: 10.3389/fonc.2018.00087
101. YOO, S. et al. Image-Guided Radiation Therapy (IGRT) for Preoperative Partial Breast Radiosurgery: A Single-Institution Experience. *International Journal of Radiation Oncology, Biology, Physics* [online]. Int J Radiat Oncol Biol Phys. November 2016, vol. **3**(102), E523 – E524 [viewed 15 March 2022]. Available from: doi: 10.1016/j.ijrobp.2018.07.1474
102. HLAVKA, A., et al. Tumor bed radiotherapy in women following breast conserving surgery for breast cancer-safety margin with/without image guidance. *Oncology Letters* [online]. Oncology Letters, February 2018, vol. **4**(15), 6009-6014 [viewed 15 March 2022]. Available from: doi: 10.3892/ol.2018.8083
103. KHAN ACADEMY: *Box plot review* [interactive]. 2022 [viewed 13 March 2022]. Access via: https://tinyurl.com/5dcw385d
104. GALARNYK M.: Understanding Boxplots [interactive]. 2018 [viewed 13 March 2022]. Access via: https://tinyurl.com/2cnskmtf
105. KELTON W.: *Standard Error* [interactive]. 2021 [viewed 13 March 2022]. Access via: https://tinyurl.com/ync2106n7
106. HARGRAVE M.: *Standard Deviation* [interactive]. 2021 [viewed 13 March 2022]. Access via: https://tinyurl.com/2p88rks8
107. CAMBRIDGE DICTIONARY: *accuracy* [interactive]. 2022 [viewed 13 March 2022]. Access via: https://tinyurl.com/27ud3jk6
108. CAMBRIDGE DICTIONARY: *precision* [interactive]. 2022 [viewed 13 March 2022]. Access via: https://tinyurl.com/3axwbahc

109. WANG, C. et al. Artificial Intelligence in Radiotherapy Treatment Planning: Present and Future. *Technology in Cancer Research & Treatment* [online]. Technol Cancer Res Treat, January 2019, vol. **1**(18) [viewed 31 March 2022]. Available from: doi: 10.1177/1533033819873922
110. ENCYCLOPEDIA.COM: *Correlation Coefficient* [interactive]. 2018 [viewed 11 May 2022]. Access via: https://tinyurl.com/yc3xbz2u
111. BROWNLEE, Z. et al. Late complications of radiation therapy for breast cancer: evolution in techniques and risk over time. *Gland surgery* [online]. Gland Surg, August 2018, vol. **7**(4), 371-378 [viewed 31 March 2022]. Available from: doi: 10.21037/gs.2018.01.05
112. ORIGINLAB: *Poly* [interactive]. 2022 [viewed 31 March 2022]. Access via: https://tinyurl.com/3snf5y7p
113. ORIGINLAB: Invs*Poly* [interactive]. 2022 [viewed 31 March 2022]. Access via: https://tinyurl.com/57cae5dn
114. ORIGINLAB: *The Linear Regression Dialog Box* [interactive]. 2022 [viewed 31 March 2022]. Access via: https://tinyurl.com/mwrcja64
115. ORIGINLAB: *CCE* [interactive]. 2022 [viewed 31 March 2022]. Access via: https://tinyurl.com/2p8ubv68
116. CORPORATE FINANCE INSTITUTE: *What is R-Squared?* [interactive]. 2022 [viewed 31 March 2022]. Access via: https://tinyurl.com/2fs8be2n
117. MOORE. S. D., NOTZ W., FLIGNER A. M., The basic practice of statistics (6th ed.). New York, NY: W. H. Freeman and Company, 2013. ISBN 9781464102547.

Appendices

Appendix 1. Simplified work scheme for the master's final degree project

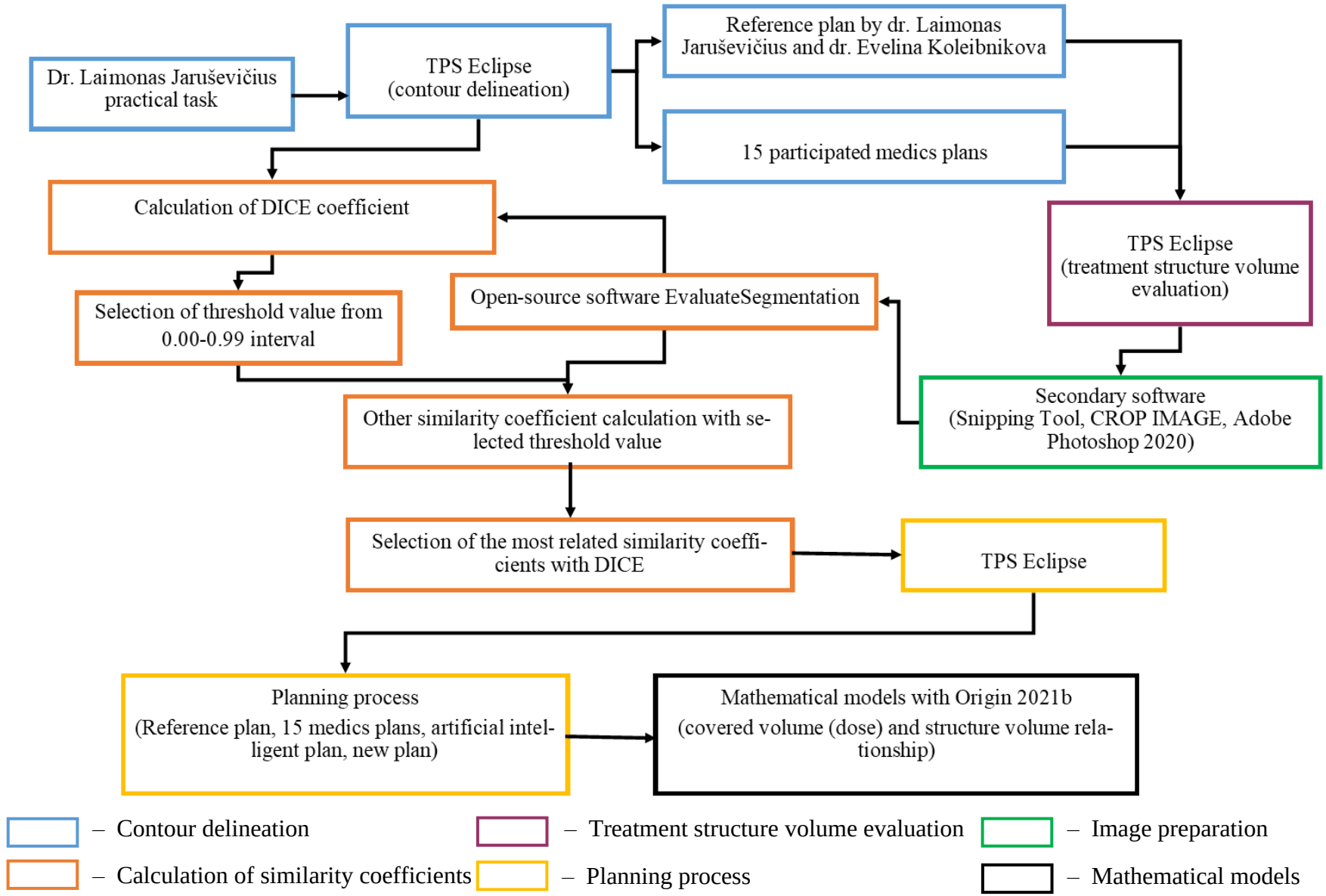

Appendix 2. Images of different *CTV_WB* structures views on a different axis

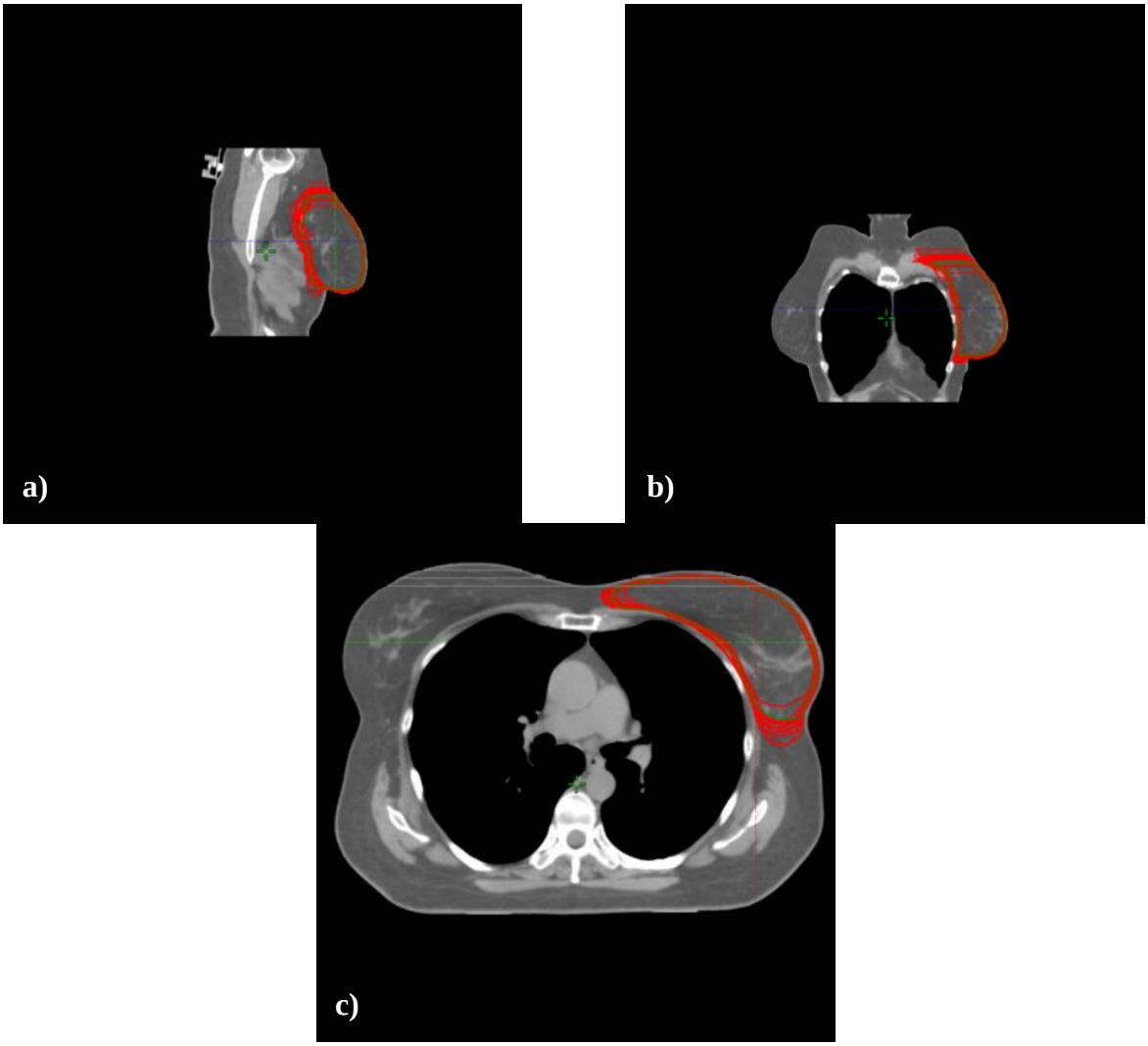

Fig. 44. Different *CTV_WB* structures views in different axis: a) x-axis; b) y-axis; c) z-axis

Appendix 3. Images of different *PTV_WB* structures views on a different axis

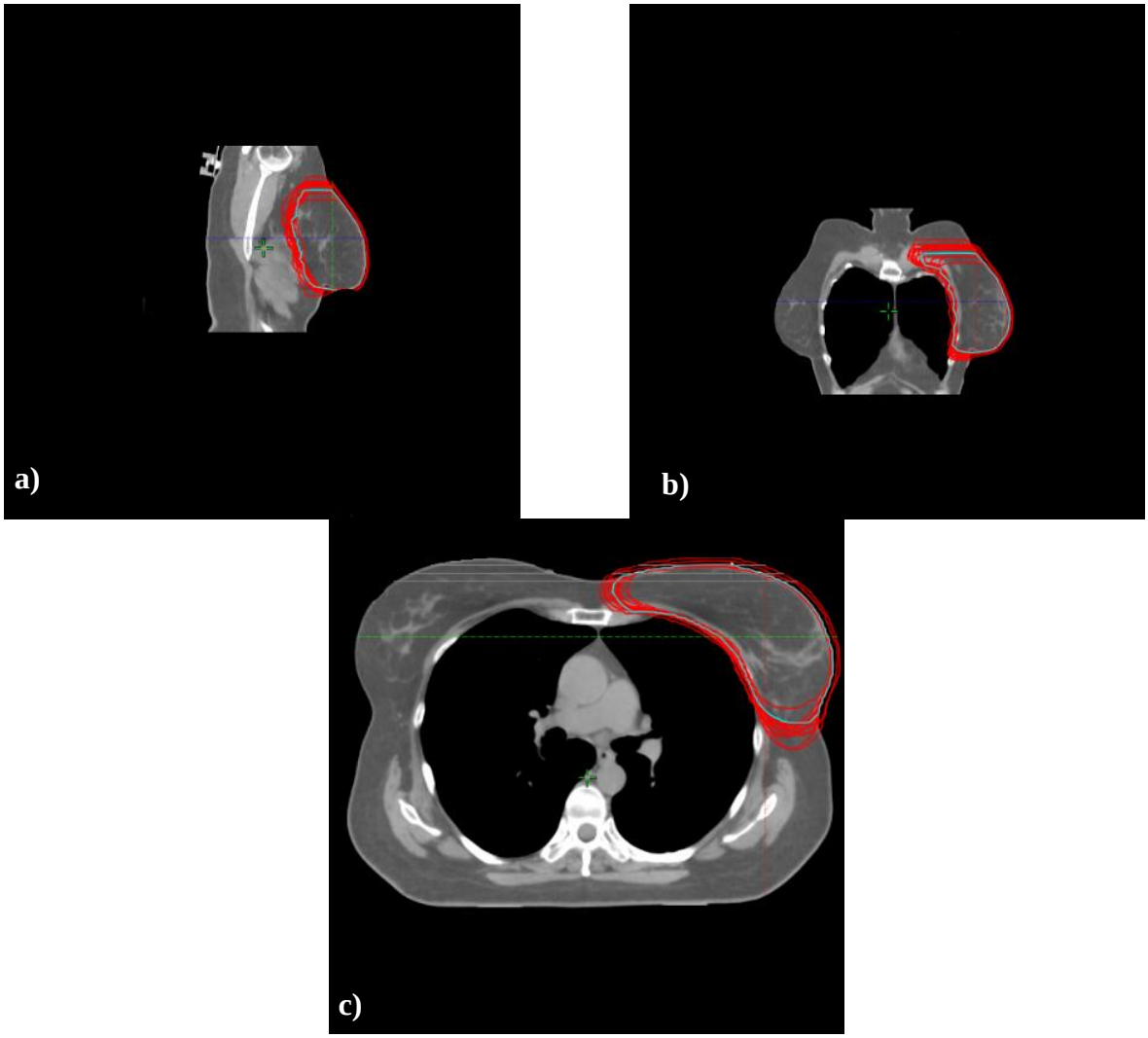

Fig. 45. Different *PTV_WB* structures views in different axis: a) x-axis; b) y-axis; c) z-axis

Appendix 4. Images of different *PTV_WB_dvh* structures views in different axis

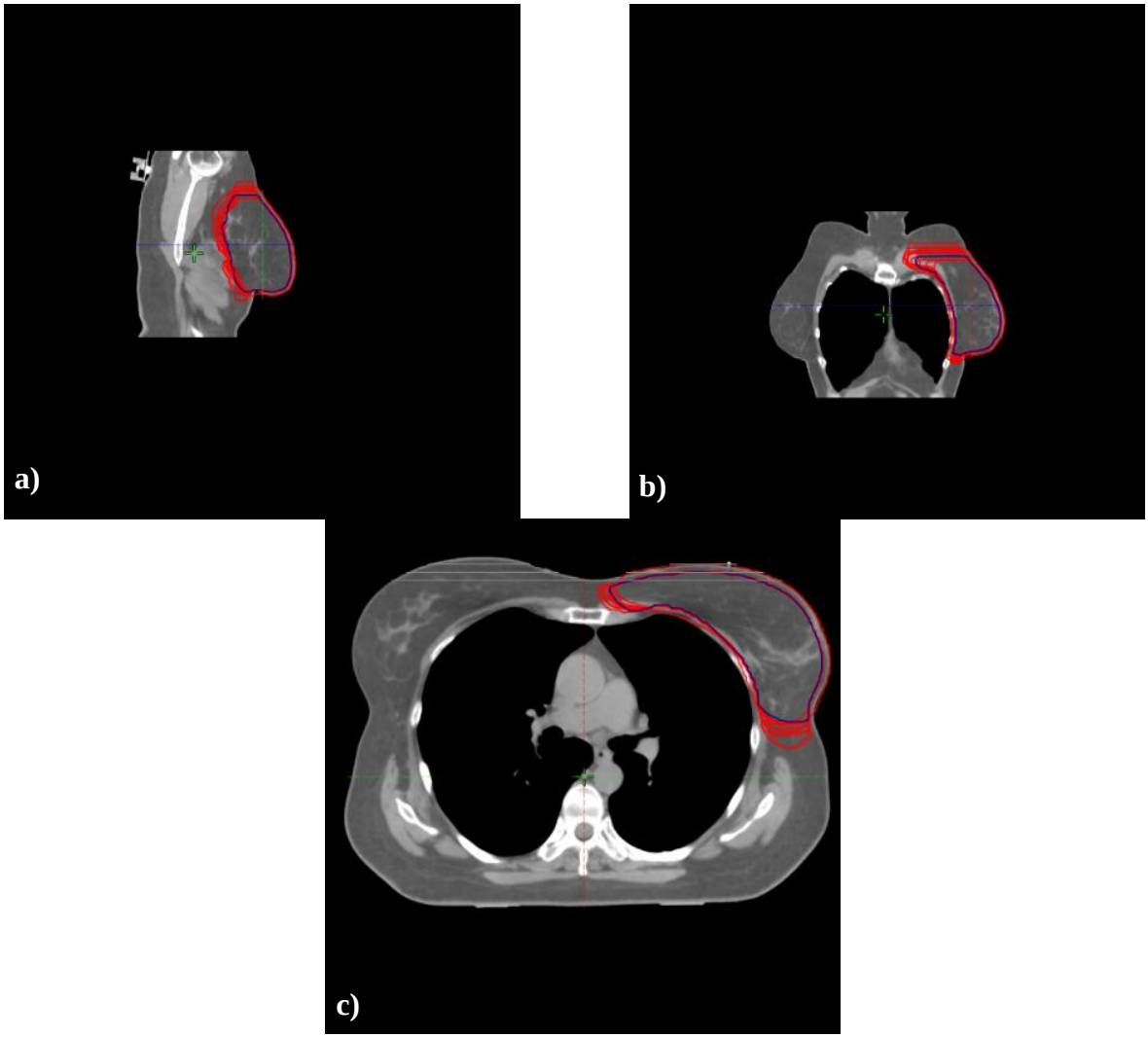

Fig. 46. Different *PTV_WB_dvh* structures views in different axis: a) x-axis; b) y-axis; c) z-axis

Appendix 5. Images of different *Heart* structures views on a different axis

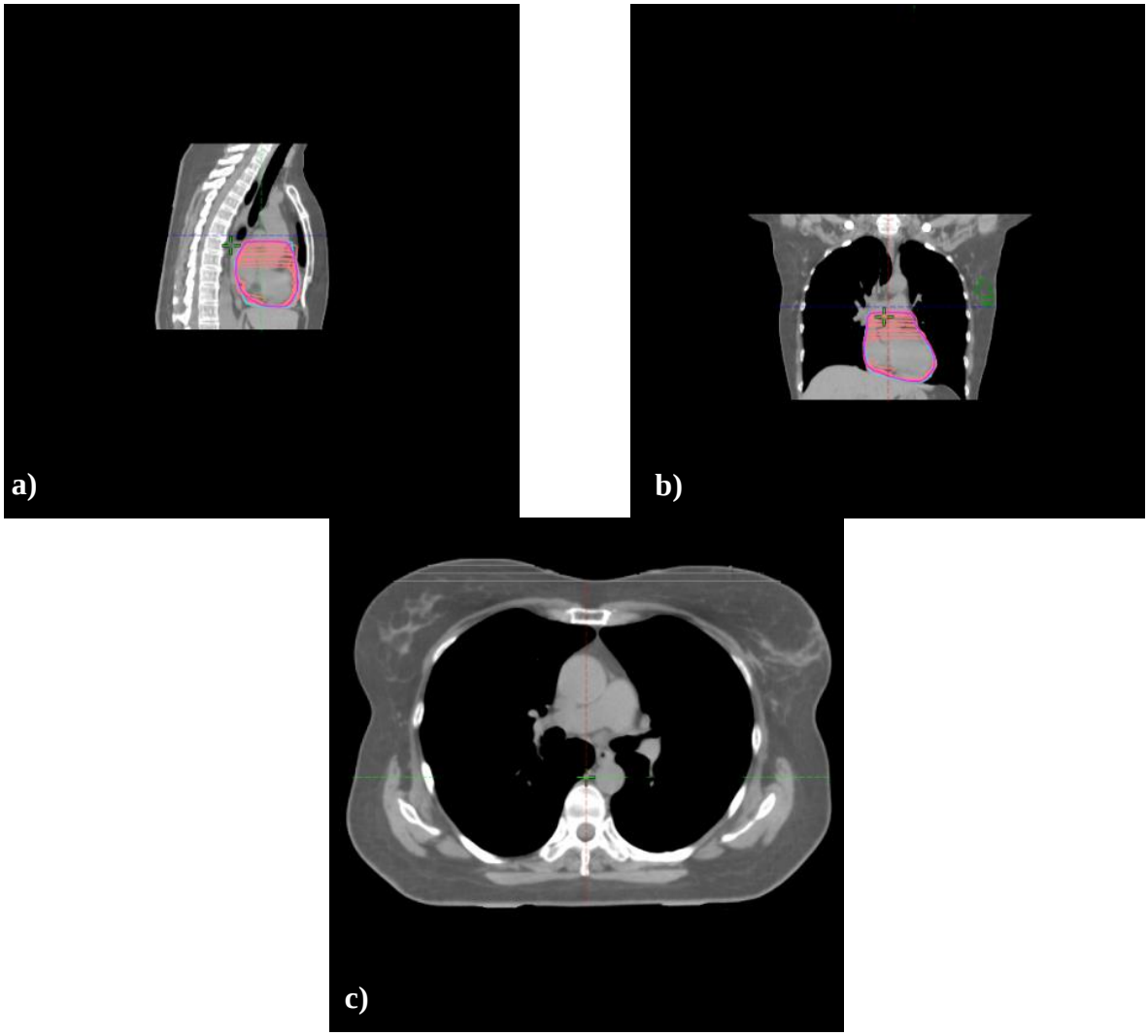

Fig. 47. Different *Heart* structures views in different axis: a) x-axis; b) y-axis; c) z-axis

Appendix 6. Images of different *Lung_ipsilat* structures views in different axis

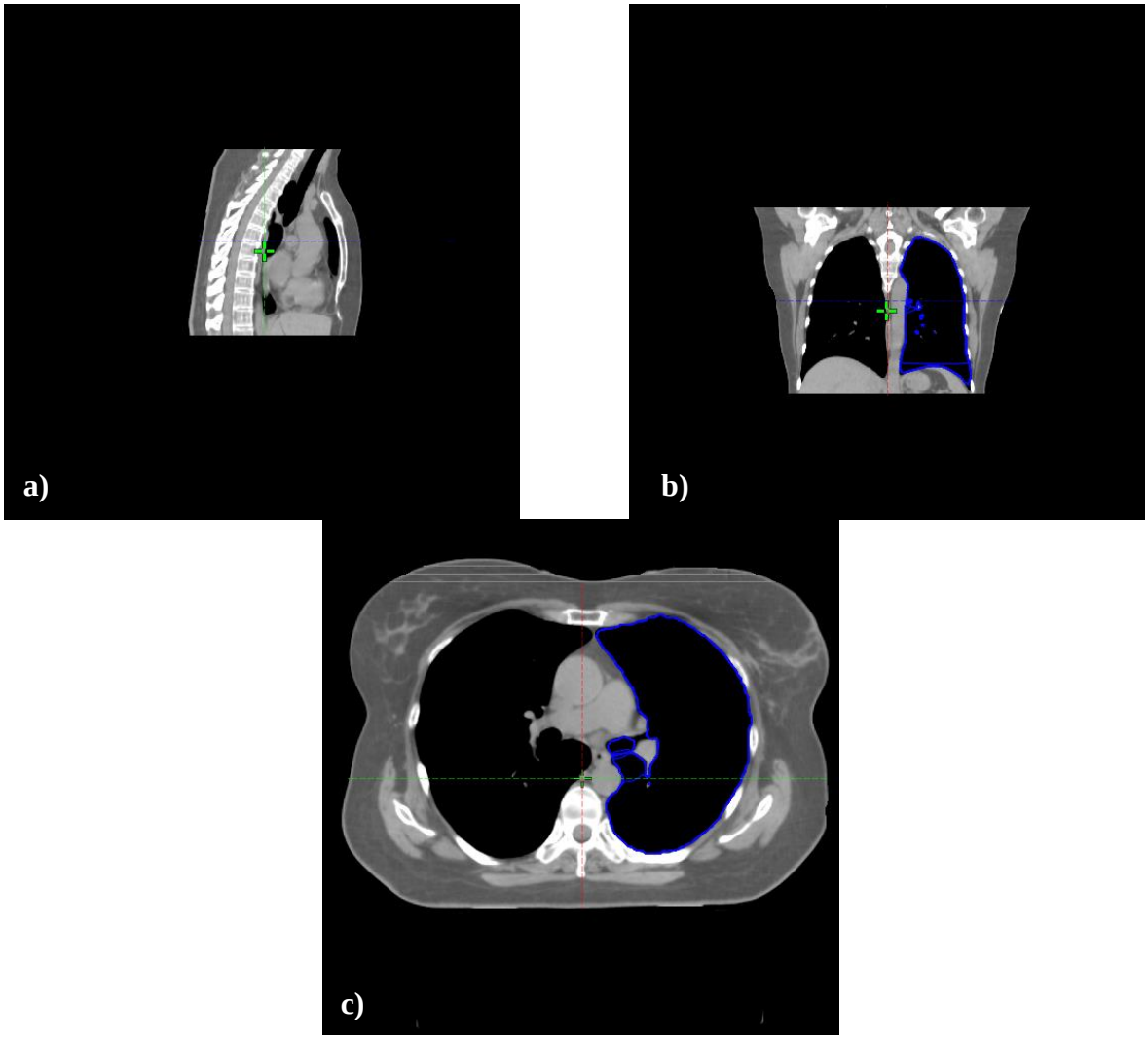

Fig. 48. Different *Lung_ipsilat* structures views in different axis: a) x-axis; b) y-axis; c) z-axis

Appendix 7. Images of different *Spinal_cord* structures views in different axis

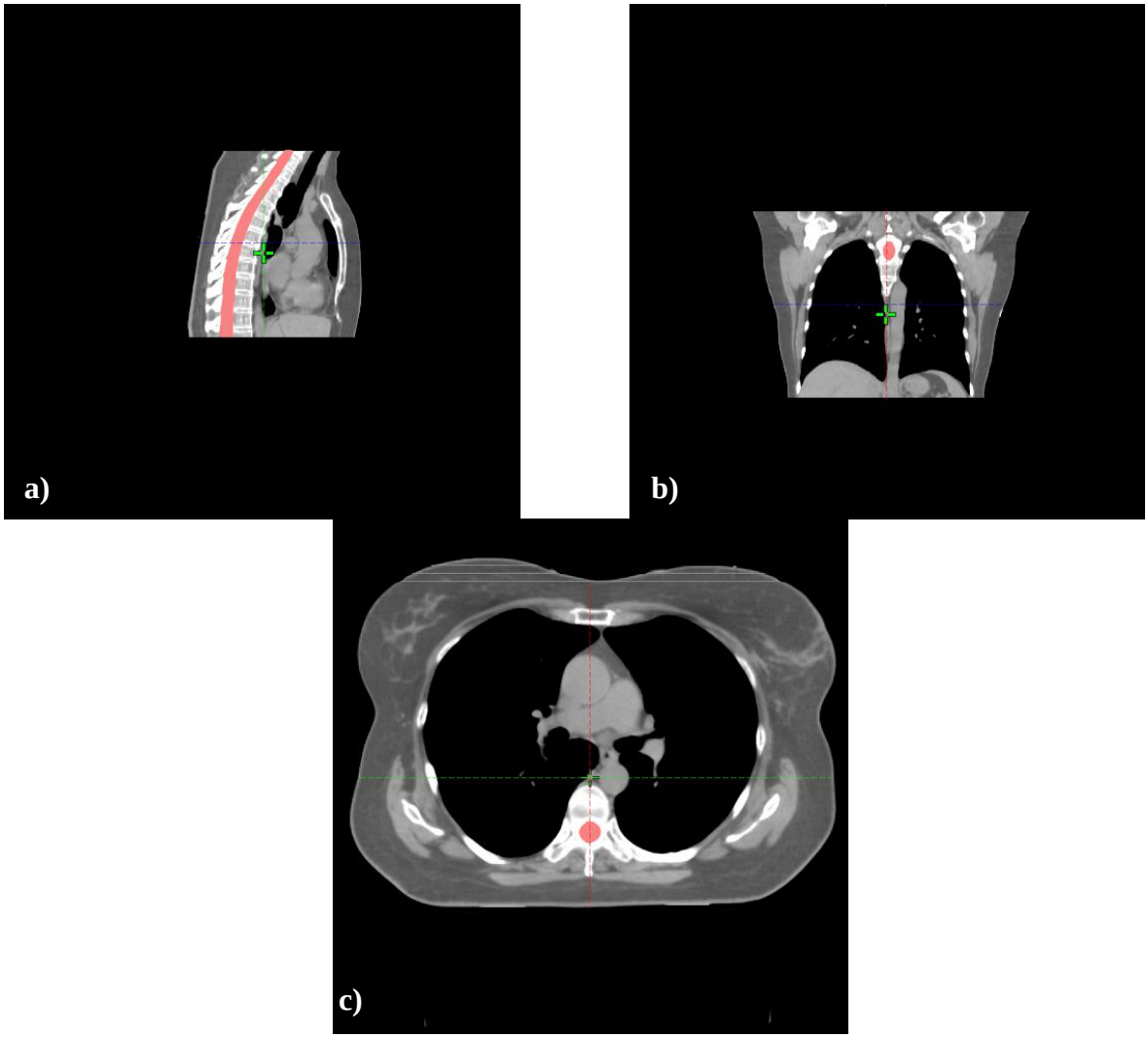

Fig. 49. Different *Spinal_cord* structures views in different axis: a) x-axis; b) y-axis; c) z-axis

Appendix 8. Images of *CTV_WB* structures

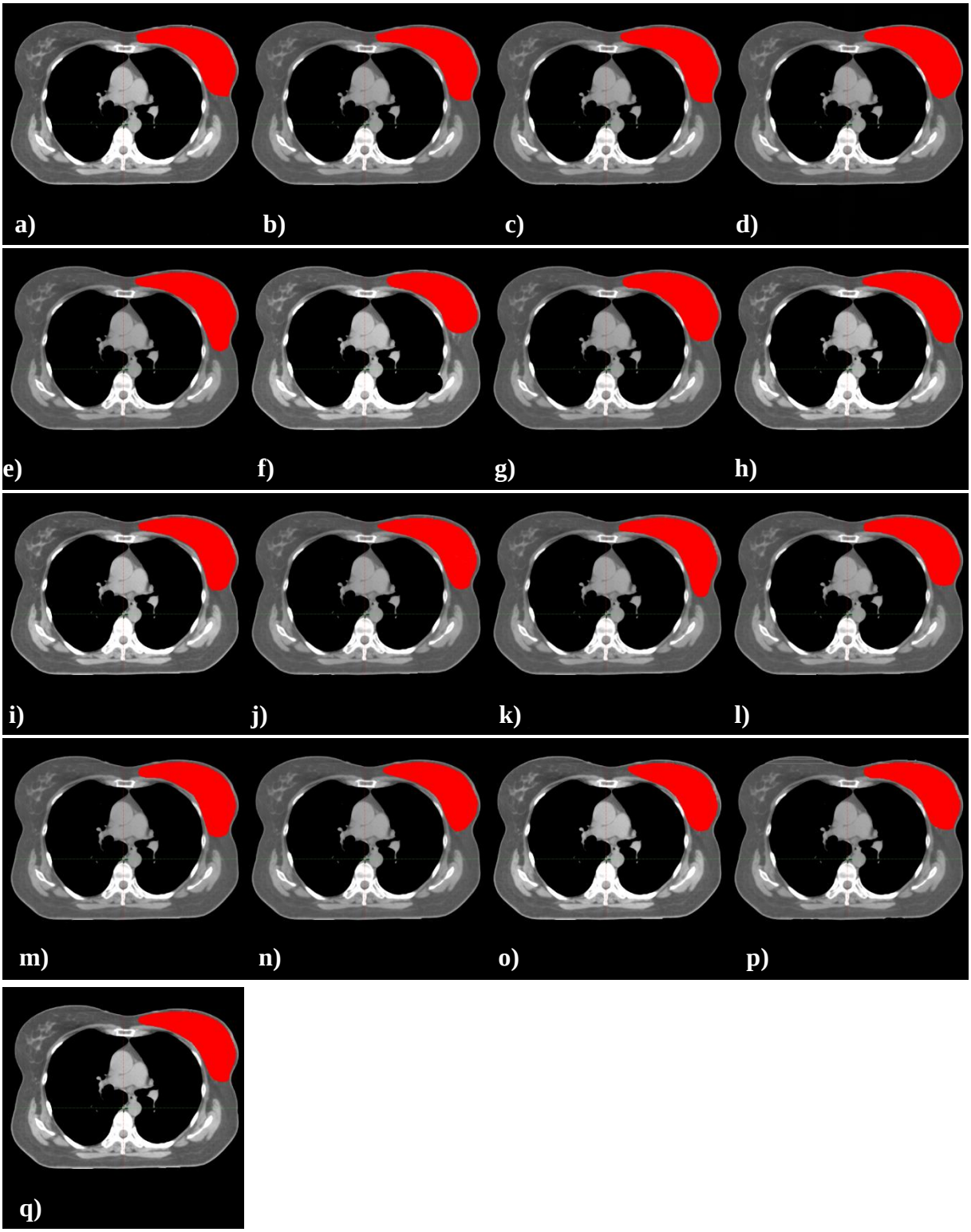

Fig. 50. Images of *CTV_WB* structures: a) 1st plan; b) 2nd plan; c) 3rd plan; d) 4th plan; e) 5th plan; f) 6th plan; g) 7th plan; h) 8th plan; i) 9th plan; j) 10th plan; k) 11th plan; l) 12th plan; m) 13th plan; n) 14th plan; o) 15th plan; p) Reference plan; q) Artificial intelligence plan

Appendix 9. Images of *PTV_WB* structures

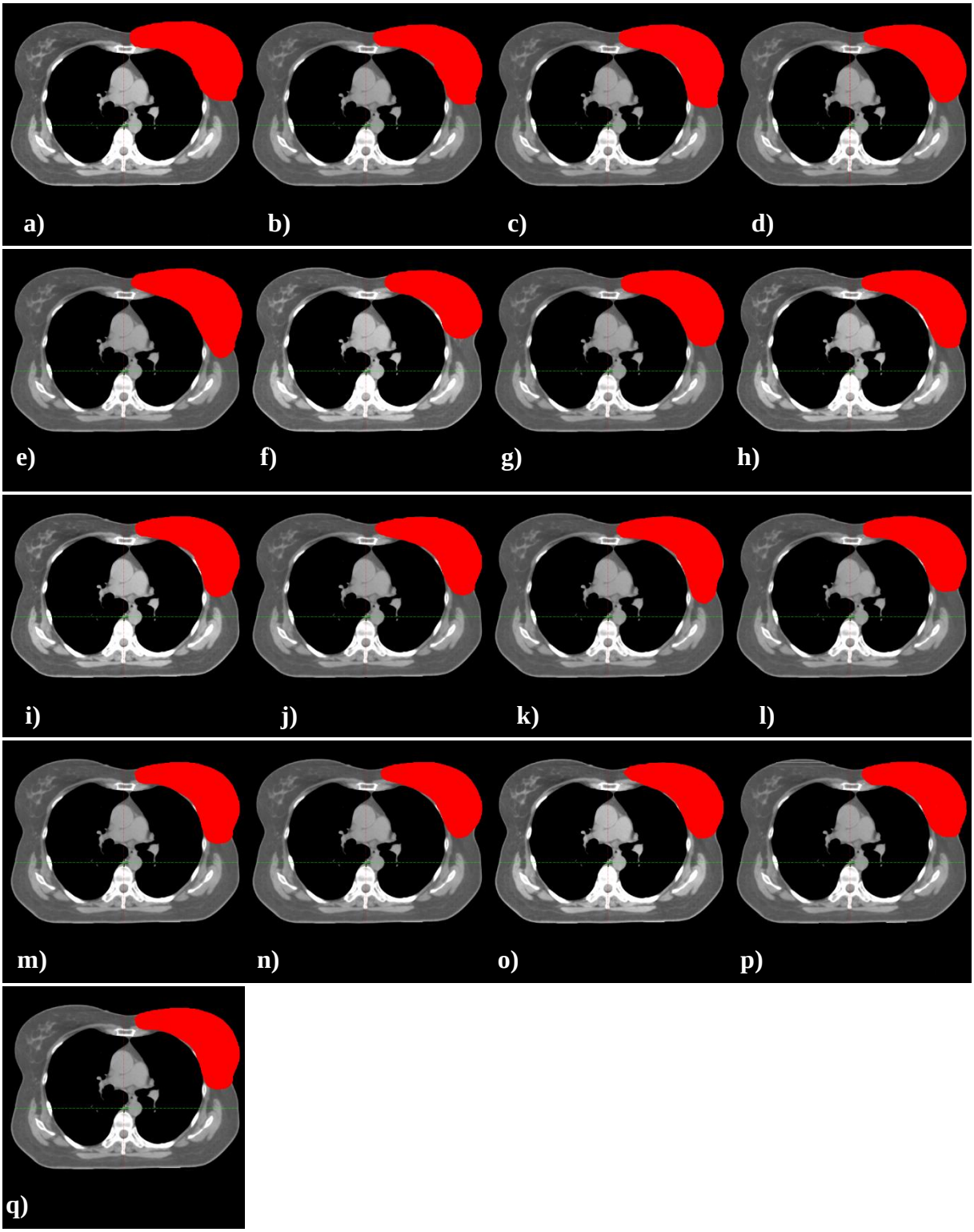

Fig. 51. Images of *PTV_WB* structures: a) 1st plan; b) 2nd plan; c) 3rd plan; d) 4th plan; e) 5th plan; f) 6th plan; g) 7th plan; h) 8th plan; i) 9th plan; j) 10th plan; k) 11th plan; l) 12th plan; m) 13th plan; n) 14th plan; o) 15th plan; Reference plan; q) Artificial intelligence plan

Appendix 10. Images of *CTV_WB* structure at the different threshold value

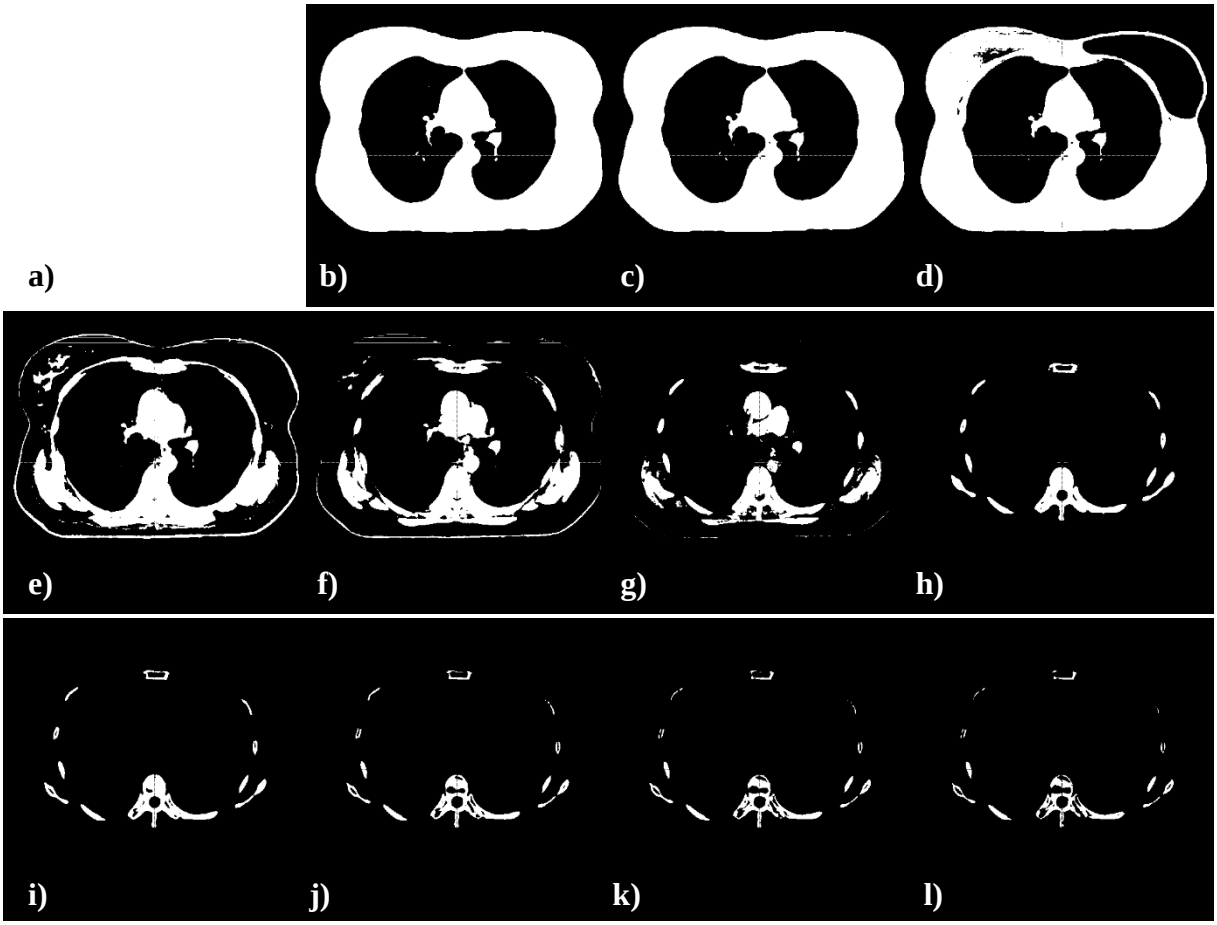

Fig. 52. Images of *CTV_WB* structure at different threshold value: a) 0.0; b) 0.1; c) 0.2; d) 0.3; e) 0.4; f) 0.5; g) 0.6; h) 0.7; i) 0.8; j) 0.9; k) 0.95; l) 0.99

Appendix 11. Images of *PTV_WB* structure at the different threshold value

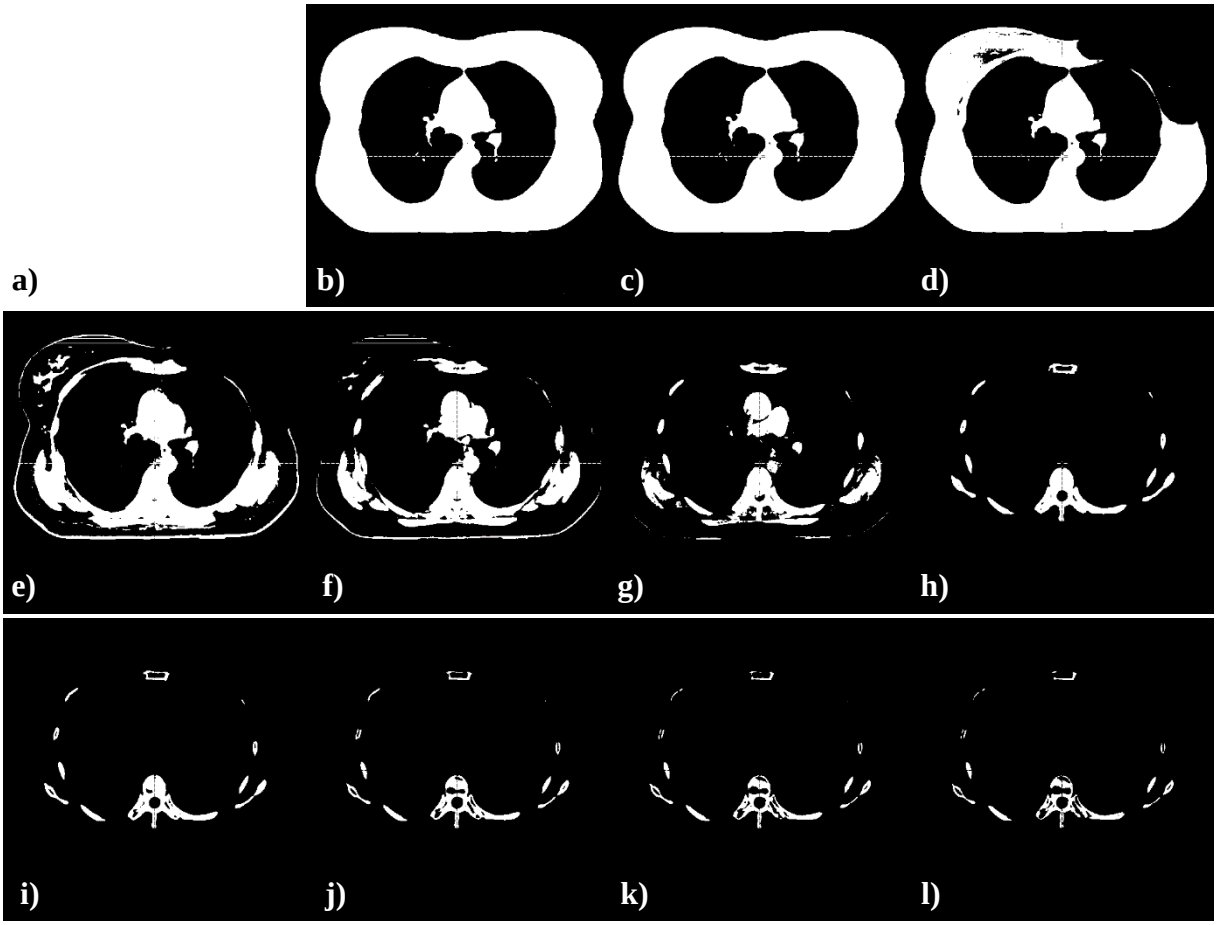

Fig. 53. Images of *PTV_WB* structure at different threshold value: a) 0.0; b) 0.1; c) 0.2; d) 0.3; e) 0.4; f) 0.5; g) 0.6; h) 0.7; i) 0.8; j) 0.9; k) 0.95; l) 0.99

Appendix 12. Analysis of *CTV_WB* similarity characteristics: comparison of 1st plan image with reference plan image

The threshold value, a. u.	0.0	0.1	0.2	0.3	0.4	0.5	0.6	0.7	0.8	0.9	0.95	0.99
DICE, a. u.	0.99581	0.99653	0.99740	0.99132	0.95817	0.92758	0.82909	0.62386	0.91864	0.87091	0.83639	0.80817
JAC, a. u.	0.99166	0.99309	0.99481	0.98280	0.91970	0.86495	0.70808	0.45334	0.84953	0.77133	0.71880	0.67809
AUC, a. u.	0.99616	0.99685	0.99767	0.99190	0.98886	0.98557	0.98512	0.98301	0.99786	0.99709	0.99663	0.99638
KAP, a. u.	0.99336	0.99454	0.99592	0.98759	0.95028	0.91788	0.81449	0.60911	0.91651	0.86803	0.83311	0.80467
RI, a. u.	0.99384	0.99495	0.99624	0.98960	0.97376	0.96624	0.94610	0.93609	0.99166	0.98864	0.98684	0.98584
ARI, a. u.	0.98762	0.98984	0.99243	0.97867	0.93303	0.89794	0.78795	0.58713	0.91247	0.86285	0.82736	0.79872
ICC, a. u.	0.99580	0.99652	0.99739	0.99130	0.95812	0.92752	0.82898	0.62373	0.91863	0.87089	0.83637	0.80814
MI, a. u.	0.92056	0.92228	0.92501	0.83888	0.54303	0.42125	0.27273	0.12113	0.14445	0.11797	0.10368	0.09240
VOI, a. u.	0.05835	0.04940	0.03855	0.08766	0.17721	0.20740	0.26281	0.26817	0.05598	0.07002	0.07752	0.08102
GCE, a. u.	0.00616	0.00506	0.00376	0.01038	0.02571	0.03233	0.04735	0.04803	0.00775	0.01012	0.01139	0.01196
PBD, a. u.	0.00002	0.00001	0.00001	0.00003	0.00017	0.00031	0.00081	0.00236	0.00035	0.00058	0.00077	0.00093
TPR, a. u.	0.99328	0.99453	0.99604	0.98460	0.99198	0.98909	0.99994	1.00000	1.00000	1.00000	1.00000	1.00000
TNR, a. u.	0.99904	0.99916	0.99929	0.99920	0.98575	0.98204	0.97029	0.96602	0.99571	0.99417	0.99326	0.99276
PRN, a. u.	0.99835	0.99855	0.99876	0.99814	0.92659	0.87327	0.70810	0.45334	0.84953	0.77133	0.71880	0.67809
FMS, a. u.	0.99581	0.99653	0.99740	0.99132	0.95817	0.92758	0.82909	0.62386	0.91864	0.87091	0.83639	0.80817
ACU, a. u.	0.99691	0.99747	0.99812	0.99477	0.98670	0.98282	0.97228	0.96695	0.99581	0.99429	0.99337	0.99287
FPR, a. u.	0.00096	0.00084	0.00071	0.00080	0.01425	0.01796	0.02971	0.03398	0.00429	0.00583	0.00674	0.00724
TIME, ms	370	431	456	367	324	351	392	334	284	283	271	266

Appendix 13. Analysis of *CTV_WB* similarity characteristics: comparison of 2nd plan image with reference plan image

The threshold value, a. u.	0.0	0.1	0.2	0.3	0.4	0.5	0.6	0.7	0.8	0.9	0.95	0.99
DICE, a. u.	0.99843	0.99884	0.99896	0.99251	0.95020	0.99046	0.99658	1.00000	1.00000	1.00000	1.00000	1.00000
JAC, a. u.	0.99686	0.99768	0.99792	0.98512	0.94266	0.98111	0.99318	1.00000	1.00000	1.00000	1.00000	1.00000
AUC, a. u.	0.99901	0.99930	0.99938	0.99381	0.95313	0.99380	0.99973	1.00000	1.00000	1.00000	1.00000	1.00000
KAP, a. u.	0.99751	0.99817	0.99837	0.98926	0.94881	0.98927	0.99633	1.00000	1.00000	1.00000	1.00000	1.00000
RI, a. u.	0.99768	0.99830	0.99849	0.99098	0.95317	0.99578	0.99908	1.00000	1.00000	1.00000	1.00000	1.00000
ARI, a. u.	0.99533	0.99658	0.99696	0.98150	0.94567	0.98666	0.99581	1.00000	1.00000	1.00000	1.00000	1.00000
ICC, a. u.	0.99842	0.99884	0.99896	0.99249	0.95019	0.99046	0.99658	1.00000	1.00000	1.00000	1.00000	1.00000
MI, a. u.	0.93849	0.93860	0.93655	0.84340	0.56971	0.48258	0.35148	0.18121	0.16146	0.13735	0.12388	0.11247
VOI, a. u.	0.02467	0.01853	0.01681	0.08146	0.04527	0.04074	0.00978	0.00000	0.00000	0.00000	0.00000	0.00000
GCE, a. u.	0.00232	0.00170	0.00151	0.00903	0.00469	0.00422	0.00092	0.00000	0.00000	0.00000	0.00000	0.00000
PBD, a. u.	0.00001	0.00001	0.00000	0.00003	0.00003	0.00004	0.00001	0.00000	0.00000	0.00000	0.00000	0.00000
TPR, a. u.	0.99969	0.99988	0.99985	0.98958	0.94969	0.98855	0.99994	1.00000	1.00000	1.00000	1.00000	1.00000
TNR, a. u.	0.99834	0.99873	0.99890	0.99803	0.95656	0.99905	0.99951	1.00000	1.00000	1.00000	1.00000	1.00000
PRN, a. u.	0.99717	0.99781	0.99807	0.99544	0.95071	0.99239	0.99324	1.00000	1.00000	1.00000	1.00000	1.00000
FMS, a. u.	0.99843	0.99884	0.99896	0.99251	0.95020	0.99046	0.99658	1.00000	1.00000	1.00000	1.00000	1.00000
ACU, a. u.	0.99884	0.99915	0.99925	0.99547	0.95550	0.99788	0.99954	1.00000	1.00000	1.00000	1.00000	1.00000
FPR, a. u.	0.00166	0.00127	0.00110	0.00197	0.00130	0.00095	0.00049	0.00000	0.00000	0.00000	0.00000	0.00000
TIME, ms	326	468	445	355	288	323	283	247	276	261	262	229

Appendix 14. Analysis of *CTV_WB* similarity characteristics: comparison of 3rd plan image with reference plan image

The threshold value, a. u.	0.0	0.1	0.2	0.3	0.4	0.5	0.6	0.7	0.8	0.9	0.95	0.99
DICE, a. u.	0.91698	0.91744	0.91757	0.91047	0.91059	0.91039	0.91674	1.00000	1.00000	1.00000	1.00000	1.00000
JAC, a. u.	0.91568	0.91661	0.91687	0.90280	0.90303	0.90264	0.91521	1.00000	1.00000	1.00000	1.00000	1.00000
AUC, a. u.	0.91743	0.91774	0.91783	0.91104	0.91173	0.91174	0.91802	1.00000	1.00000	1.00000	1.00000	1.00000
KAP, a. u.	0.91621	0.91696	0.91717	0.90711	0.90920	0.90941	0.91663	1.00000	1.00000	1.00000	1.00000	1.00000
RI, a. u.	0.91636	0.91706	0.91726	0.90892	0.91359	0.91479	0.91786	1.00000	1.00000	1.00000	1.00000	1.00000
ARI, a. u.	0.91442	0.91582	0.91623	0.89909	0.90607	0.90726	0.91639	1.00000	1.00000	1.00000	1.00000	1.00000
ICC, a. u.	0.91697	0.91744	0.91757	0.91045	0.91058	0.91038	0.91674	1.00000	1.00000	1.00000	1.00000	1.00000
MI, a. u.	0.86258	0.86326	0.86160	0.77096	0.54447	0.44423	0.32429	0.18121	0.16146	0.13735	0.12388	0.11247
VOI, a. u.	0.02093	0.01407	0.01204	0.07946	0.04341	0.03318	0.00498	0.00000	0.00000	0.00000	0.00000	0.00000
GCE, a. u.	0.00192	0.00122	0.00102	0.00934	0.00467	0.00347	0.00041	0.00000	0.00000	0.00000	0.00000	0.00000
PBD, a. u.	0.00001	0.00000	0.00000	0.00003	0.00003	0.00003	0.00064	0.00000	0.00000	0.00000	0.00000	0.00000
TPR, a. u.	0.91789	0.91803	0.91804	0.90461	0.90568	0.90558	0.91796	1.00000	1.00000	1.00000	1.00000	1.00000
TNR, a. u.	0.91698	0.91745	0.91761	0.91747	0.91779	0.91790	0.91807	1.00000	1.00000	1.00000	1.00000	1.00000
PRN, a. u.	0.91607	0.91685	0.91711	0.91641	0.91555	0.91525	0.91552	1.00000	1.00000	1.00000	1.00000	1.00000
FMS, a. u.	0.91698	0.91744	0.91757	0.91047	0.91059	0.91039	0.91674	1.00000	1.00000	1.00000	1.00000	1.00000
ACU, a. u.	0.91731	0.91766	0.91777	0.91357	0.91593	0.91653	0.91807	1.00000	1.00000	1.00000	1.00000	1.00000
FPR, a. u.	0.00129	0.00082	0.00066	0.00080	0.00049	0.00037	0.00020	0.00000	0.00000	0.00000	0.00000	0.00000
TIME, ms	328	373	365	318	275	284	262	261	264	262	253	259

Appendix 15. Analysis of *CTV_WB* similarity characteristics: comparison of 4th plan image with reference plan image

The threshold value, a. u.	0.0	0.1	0.2	0.3	0.4	0.5	0.6	0.7	0.8	0.9	0.95	0.99
DICE, a. u.	0.85505	0.91965	0.91979	0.91240	0.91048	0.90970	0.91732	1.00000	1.00000	1.00000	1.00000	1.00000
JAC, a. u.	0.79806	0.91850	0.91878	0.90415	0.90038	0.89885	0.91386	1.00000	1.00000	1.00000	1.00000	1.00000
AUC, a. u.	0.87925	0.92009	0.92019	0.91342	0.91275	0.91248	0.92036	1.00000	1.00000	1.00000	1.00000	1.00000
KAP, a. u.	0.81192	0.91899	0.91921	0.90877	0.90862	0.90832	0.91707	1.00000	1.00000	1.00000	1.00000	1.00000
RI, a. u.	0.82205	0.91912	0.91934	0.91072	0.91452	0.91591	0.91987	1.00000	1.00000	1.00000	1.00000	1.00000
ARI, a. u.	0.72299	0.91741	0.91785	0.90012	0.90442	0.90530	0.91653	1.00000	1.00000	1.00000	1.00000	1.00000
ICC, a. u.	0.85485	0.91965	0.91979	0.91238	0.91047	0.90969	0.91732	1.00000	1.00000	1.00000	1.00000	1.00000
MI, a. u.	0.65224	0.86353	0.86193	0.76992	0.53944	0.43955	0.32311	0.18121	0.16146	0.13735	0.12388	0.11247
VOI, a. u.	0.47712	0.01853	0.01639	0.08677	0.05668	0.04511	0.01008	0.00000	0.00000	0.00000	0.00000	0.00000
GCE, a. u.	0.09775	0.00169	0.00147	0.01008	0.00627	0.00489	0.00094	0.00000	0.00000	0.00000	0.00000	0.00000
PBD, a. u.	0.00028	0.00000	0.00000	0.00003	0.00004	0.00004	0.00001	0.00000	0.00000	0.00000	0.00000	0.00000
TPR, a. u.	0.92071	0.92058	0.92063	0.90752	0.90566	0.90493	0.92039	1.00000	1.00000	1.00000	1.00000	1.00000
TNR, a. u.	0.83780	0.91961	0.91976	0.91931	0.91983	0.92003	0.92034	1.00000	1.00000	1.00000	1.00000	1.00000
PRN, a. u.	0.79814	0.91873	0.91896	0.91733	0.91535	0.91452	0.91427	1.00000	1.00000	1.00000	1.00000	1.00000
FMS, a. u.	0.85505	0.91965	0.91979	0.91240	0.91048	0.90970	0.91732	1.00000	1.00000	1.00000	1.00000	1.00000
ACU, a. u.	0.86845	0.91996	0.92007	0.91574	0.91766	0.91835	0.92034	1.00000	1.00000	1.00000	1.00000	1.00000
FPR, a. u.	0.08301	0.00120	0.00105	0.00150	0.00098	0.00078	0.00047	0.00000	0.00000	0.00000	0.00000	0.00000
TIME, ms	454	448	349	352	283	314	273	276	260	268	281	280

Appendix 16. Analysis of *CTV_WB* similarity characteristics: comparison of 5th plan image with reference plan image

The threshold value, a. u.	0.0	0.1	0.2	0.3	0.4	0.5	0.6	0.7	0.8	0.9	0.95	0.99
DICE, a. u.	0.92795	0.92828	0.92839	0.91924	0.92040	0.91949	0.92595	1.00000	1.00000	1.00000	1.00000	1.00000
JAC, a. u.	0.92653	0.92718	0.92741	0.90934	0.91161	0.90983	0.92256	1.00000	1.00000	1.00000	1.00000	1.00000
AUC, a. u.	0.92849	0.92872	0.92879	0.92018	0.92236	0.92213	0.92902	1.00000	1.00000	1.00000	1.00000	1.00000
KAP, a. u.	0.92711	0.92764	0.92783	0.91488	0.91879	0.91826	0.92571	1.00000	1.00000	1.00000	1.00000	1.00000
RI, a. u.	0.92726	0.92777	0.92794	0.91726	0.92390	0.92500	0.92845	1.00000	1.00000	1.00000	1.00000	1.00000
ARI, a. u.	0.92514	0.92615	0.92650	0.90453	0.91513	0.91557	0.92518	1.00000	1.00000	1.00000	1.00000	1.00000
ICC, a. u.	0.92794	0.92827	0.92838	0.91922	0.92039	0.91949	0.92595	1.00000	1.00000	1.00000	1.00000	1.00000
MI, a. u.	0.87253	0.87227	0.87036	0.77024	0.54810	0.44620	0.32633	0.18121	0.16146	0.13735	0.12388	0.11247
VOI, a. u.	0.02229	0.01732	0.01574	0.09971	0.05043	0.04104	0.00979	0.00000	0.00000	0.00000	0.00000	0.00000
GCE, a. u.	0.00210	0.00160	0.00142	0.01209	0.00545	0.00435	0.00092	0.00000	0.00000	0.00000	0.00000	0.00000
PBD, a. u.	0.00001	0.00000	0.00000	0.00004	0.00004	0.00004	0.00001	0.00000	0.00000	0.00000	0.00000	0.00000
TPR, a. u.	0.92914	0.92928	0.92926	0.91231	0.91621	0.91563	0.92916	1.00000	1.00000	1.00000	1.00000	1.00000
TNR, a. u.	0.92783	0.92815	0.92831	0.92805	0.92852	0.92863	0.92889	1.00000	1.00000	1.00000	1.00000	1.00000
PRN, a. u.	0.92676	0.92727	0.92751	0.92628	0.92464	0.92339	0.92277	1.00000	1.00000	1.00000	1.00000	1.00000
FMS, a. u.	0.92795	0.92828	0.92839	0.91924	0.92040	0.91949	0.92595	1.00000	1.00000	1.00000	1.00000	1.00000
ACU, a. u.	0.92832	0.92857	0.92866	0.92327	0.92663	0.92718	0.92891	1.00000	1.00000	1.00000	1.00000	1.00000
FPR, a. u.	0.00154	0.00121	0.00106	0.00132	0.00085	0.00074	0.00048	0.00000	0.00000	0.00000	0.00000	0.00000
TIME, ms	310	401	409	331	289	284	263	250	249	265	278	275

Appendix 17. Analysis of *CTV_WB* similarity characteristics: comparison of 6th plan image with reference plan image

The threshold value, a. u.	0.0	0.1	0.2	0.3	0.4	0.5	0.6	0.7	0.8	0.9	0.95	0.99
DICE, a. u.	0.99815	0.99901	1.00000	0.98881	0.93066	0.89727	0.79647	0.55192	0.89005	0.84897	0.81347	0.77859
JAC, a. u.	0.99011	0.99181	0.99375	0.97190	0.91885	0.80954	0.65903	0.38023	0.79786	0.73417	0.68264	0.63492
AUC, a. u.	0.99867	0.99950	1.00045	0.99564	0.97253	0.97924	0.98091	0.96943	0.98819	0.98589	0.98399	0.98200
KAP, a. u.	0.99340	0.99483	0.99643	0.98112	0.96739	0.88233	0.77810	0.53332	0.88698	0.84547	0.80960	0.77444
RI, a. u.	0.99438	0.99574	0.99723	0.98517	0.93119	0.95480	0.93847	0.92201	0.99434	0.99253	0.99088	0.98950
ARI, a. u.	0.98231	0.98503	0.98804	0.96302	0.82051	0.85285	0.74597	0.50755	0.88138	0.83938	0.80308	0.76766
ICC, a. u.	0.99812	0.99899	0.99998	0.98877	0.89051	0.89716	0.79633	0.55175	0.89002	0.84894	0.81344	0.77856
MI, a. u.	0.90452	0.90655	0.90924	0.81040	0.45616	0.38815	0.25375	0.10579	0.13414	0.10994	0.09618	0.08486
VOI, a. u.	0.10053	0.09100	0.08027	0.16585	0.40416	0.29515	0.32308	0.33759	0.08058	0.08731	0.09351	0.09825
GCE, a. u.	0.01194	0.01058	0.00909	0.02119	0.07152	0.04877	0.05871	0.06143	0.01106	0.01231	0.01339	0.01420
PBD, a. u.	0.00003	0.00003	0.00003	0.00007	0.00051	0.00048	0.00104	0.00325	0.00052	0.00073	0.00094	0.00115
TPR, a. u.	0.99239	0.99392	0.99570	0.99569	0.98017	0.97843	0.99216	0.97704	0.97548	0.97187	0.96892	0.96568
TNR, a. u.	1.00496	1.00509	1.00520	0.99560	0.96489	0.98005	0.96965	0.96181	1.00089	0.99992	0.99905	0.99833
PRN, a. u.	1.00398	1.00416	1.00433	0.98203	0.81614	0.82854	0.66525	0.38459	0.81838	0.75366	0.70100	0.65224
FMS, a. u.	0.99815	0.99901	1.00000	0.98881	0.89066	0.89727	0.79647	0.55192	0.89005	0.84897	0.81347	0.77859
ACU, a. u.	1.00031	1.00100	1.00176	0.99563	0.96724	0.97987	0.97117	0.96223	1.00029	0.99938	0.99854	0.99784
FPR, a. u.	0.00136	0.00123	0.00112	0.01072	0.04143	0.02627	0.03667	0.04451	0.00543	0.00640	0.00727	0.00799
TIME, ms	478	476	489	520	542	460	451	381	290	296	294	295

Appendix 18. Analysis of *CTV_WB* similarity characteristics: comparison of 7th plan image with reference plan image

The threshold value, a. u.	0.0	0.1	0.2	0.3	0.4	0.5	0.6	0.7	0.8	0.9	0.95	0.99
DICE, a. u.	0.94913	0.94947	0.94960	0.94549	0.94017	0.93943	0.94643	0.94978	0.95042	1.00000	1.00000	1.00000
JAC, a. u.	0.94769	0.94838	0.94862	0.94046	0.93000	0.92856	0.94232	0.94898	0.95026	1.00000	1.00000	1.00000
AUC, a. u.	0.94966	0.94991	0.94999	0.94624	0.94197	0.94183	0.94955	0.94978	0.95042	1.00000	1.00000	1.00000
KAP, a. u.	0.94828	0.94884	0.94904	0.94328	0.93830	0.93805	0.94613	0.94975	0.95041	1.00000	1.00000	1.00000
RI, a. u.	0.94844	0.94896	0.94916	0.94444	0.94425	0.94566	0.94945	0.95048	0.95056	1.00000	1.00000	1.00000
ARI, a. u.	0.94629	0.94734	0.94773	0.93800	0.93408	0.93503	0.94549	0.94971	0.95041	1.00000	1.00000	1.00000
ICC, a. u.	0.94913	0.94947	0.94959	0.94548	0.94016	0.93942	0.94643	0.94978	0.95042	1.00000	1.00000	1.00000
MI, a. u.	0.89242	0.89226	0.89041	0.81161	0.55741	0.45424	0.33253	0.17156	0.15334	0.13735	0.12388	0.11247
VOI, a. u.	0.02277	0.01752	0.01569	0.05791	0.05662	0.04508	0.01215	0.00115	0.00023	0.00000	0.00000	0.00000
GCE, a. u.	0.00213	0.00161	0.00141	0.00613	0.00630	0.00489	0.00111	0.00009	0.00001	0.00000	0.00000	0.00000
PBD, a. u.	0.00001	0.00000	0.00000	0.00002	0.00004	0.00004	0.00002	0.00000	0.00000	0.00000	0.00000	0.00000
TPR, a. u.	0.95027	0.95046	0.95046	0.94306	0.93413	0.93375	0.94901	0.94898	0.95026	1.00000	1.00000	1.00000
TNR, a. u.	0.94906	0.94936	0.94952	0.94943	0.94980	0.94990	0.95008	0.95057	0.95057	1.00000	1.00000	1.00000
PRN, a. u.	0.94800	0.94848	0.94873	0.94793	0.94629	0.94519	0.94387	0.95057	0.95057	1.00000	1.00000	1.00000
FMS, a. u.	0.94913	0.94947	0.94960	0.94549	0.94017	0.93943	0.94643	0.94978	0.95042	1.00000	1.00000	1.00000
ACU, a. u.	0.94950	0.94977	0.94986	0.94750	0.94740	0.94811	0.95001	0.95053	0.95056	1.00000	1.00000	1.00000
FPR, a. u.	0.00151	0.00121	0.00105	0.00114	0.00077	0.00067	0.00049	0.00000	0.00000	0.00000	0.00000	0.00000
TIME, ms	364	387	399	369	320	308	302	279	267	262	259	263

Appendix 19. Analysis of *CTV_WB* similarity characteristics: comparison of 8th plan image with reference plan image

The threshold value, a. u.	0.0	0.1	0.2	0.3	0.4	0.5	0.6	0.7	0.8	0.9	0.95	0.99
DICE, a. u.	0.99534	0.99609	0.99696	0.98883	0.95523	0.92478	0.82671	0.62194	0.91864	0.87091	0.83639	0.80817
JAC, a. u.	0.99073	0.99220	0.99393	0.97791	0.91430	0.86008	0.70461	0.45131	0.84953	0.77133	0.71880	0.67809
AUC, a. u.	0.99585	0.99657	0.99740	0.99071	0.98846	0.98554	0.98489	0.98287	0.99786	0.99709	0.99663	0.99638
KAP, a. u.	0.99262	0.99383	0.99523	0.98401	0.94675	0.91466	0.81187	0.60710	0.91651	0.86803	0.83311	0.80467
RI, a. u.	0.99315	0.99429	0.99560	0.98661	0.97184	0.96481	0.94522	0.93559	0.99166	0.98864	0.98684	0.98584
ARI, a. u.	0.98623	0.98853	0.99115	0.97254	0.92827	0.89392	0.78495	0.58500	0.91247	0.86285	0.82736	0.79872
ICC, a. u.	0.99533	0.99607	0.99695	0.98881	0.95518	0.92471	0.82660	0.62181	0.91863	0.87089	0.83637	0.80814
MI, a. u.	0.91752	0.91933	0.92206	0.82690	0.53977	0.41972	0.27197	0.12090	0.14445	0.11797	0.10368	0.09240
VOI, a. u.	0.06460	0.05551	0.04468	0.11321	0.18636	0.21307	0.26589	0.26971	0.05598	0.07002	0.07752	0.08102
GCE, a. u.	0.00686	0.00571	0.00440	0.01340	0.02752	0.03360	0.04805	0.04835	0.00775	0.01012	0.01139	0.01196
PBD, a. u.	0.00002	0.00002	0.00001	0.00004	0.00018	0.00032	0.00082	0.00238	0.00035	0.00058	0.00077	0.00093
TPR, a. u.	0.99310	0.99442	0.99597	0.98424	0.99242	0.98999	1.00000	1.00000	1.00000	1.00000	1.00000	1.00000
TNR, a. u.	0.99860	0.99871	0.99883	0.99719	0.98450	0.98110	0.96978	0.96574	0.99571	0.99417	0.99326	0.99276
PRN, a. u.	0.99760	0.99775	0.99794	0.99347	0.92073	0.86763	0.70461	0.45131	0.84953	0.77133	0.71880	0.67809
FMS, a. u.	0.99534	0.99609	0.99696	0.98883	0.95523	0.92478	0.82671	0.62194	0.91864	0.87091	0.83639	0.80817
ACU, a. u.	0.99656	0.99714	0.99780	0.99326	0.98572	0.98209	0.97181	0.96668	0.99581	0.99429	0.99337	0.99287
FPR, a. u.	0.00140	0.00129	0.00117	0.00281	0.01550	0.01890	0.03022	0.03426	0.00429	0.00583	0.00674	0.00724
TIME, ms	392	514	472	400	373	403	392	351	281	302	292	279

Appendix 20. Analysis of *CTV_WB* similarity characteristics: comparison of 9th plan image with reference plan image

The threshold value, a. u.	0.0	0.1	0.2	0.3	0.4	0.5	0.6	0.7	0.8	0.9	0.95	0.99
DICE, a. u.	0.99545	0.99617	0.99704	0.98699	0.95517	0.92471	0.82695	0.62229	0.91864	0.87091	0.83639	0.80817
JAC, a. u.	0.99094	0.99237	0.99410	0.97431	0.91419	0.85997	0.70496	0.45168	0.84953	0.77133	0.71880	0.67809
AUC, a. u.	0.99592	0.99662	0.99745	0.98908	0.98855	0.98550	0.98489	0.98290	0.99786	0.99709	0.99663	0.99638
KAP, a. u.	0.99279	0.99396	0.99536	0.98137	0.94668	0.91459	0.81214	0.60747	0.91651	0.86803	0.83311	0.80467
RI, a. u.	0.99331	0.99442	0.99572	0.98443	0.97180	0.96479	0.94531	0.93568	0.99166	0.98864	0.98684	0.98584
ARI, a. u.	0.98655	0.98877	0.99139	0.96807	0.92817	0.89383	0.78526	0.58539	0.91247	0.86285	0.82736	0.79872
ICC, a. u.	0.99544	0.99616	0.99703	0.98696	0.95512	0.92464	0.82684	0.62216	0.91863	0.87089	0.83637	0.80814
MI, a. u.	0.91821	0.91987	0.92261	0.81907	0.53990	0.41962	0.27199	0.12094	0.14445	0.11797	0.10368	0.09240
VOI, a. u.	0.06317	0.05439	0.04355	0.12802	0.18632	0.21326	0.26566	0.26943	0.05598	0.07002	0.07752	0.08102
GCE, a. u.	0.00670	0.00559	0.00428	0.01558	0.02756	0.03363	0.04798	0.04830	0.00775	0.01012	0.01139	0.01196
PBD, a. u.	0.00002	0.00002	0.00001	0.00005	0.00018	0.00032	0.00082	0.00238	0.00035	0.00058	0.00077	0.00093
TPR, a. u.	0.99313	0.99444	0.99599	0.98127	0.99267	0.98992	0.99994	1.00000	1.00000	1.00000	1.00000	1.00000
TNR, a. u.	0.99871	0.99880	0.99892	0.99689	0.98443	0.98109	0.96984	0.96580	0.99571	0.99417	0.99326	0.99276
PRN, a. u.	0.99778	0.99791	0.99809	0.99277	0.92041	0.86756	0.70499	0.45168	0.84953	0.77133	0.71880	0.67809
FMS, a. u.	0.99545	0.99617	0.99704	0.98699	0.95517	0.92471	0.82695	0.62229	0.91864	0.87091	0.83639	0.80817
ACU, a. u.	0.99664	0.99720	0.99786	0.99215	0.98570	0.98207	0.97186	0.96673	0.99581	0.99429	0.99337	0.99287
FPR, a. u.	0.00130	0.00120	0.00108	0.00311	0.01557	0.01891	0.03016	0.03421	0.00429	0.00583	0.00674	0.00724
TIME, ms	399	427	524	381	352	433	391	375	285	282	287	281

Appendix 21. Analysis of *CTV_WB* similarity characteristics: comparison of 10th plan image with reference plan image

The threshold value, a. u.	0.0	0.1	0.2	0.3	0.4	0.5	0.6	0.7	0.8	0.9	0.95	0.99
DICE, a. u.	0.95633	0.95675	0.95691	0.95115	0.95025	0.94908	0.95487	1.00000	1.00000	1.00000	1.00000	1.00000
JAC, a. u.	0.95482	0.95565	0.95597	0.94453	0.94276	0.94047	0.95191	1.00000	1.00000	1.00000	1.00000	1.00000
AUC, a. u.	0.95689	0.95718	0.95729	0.95326	0.95324	0.95210	0.95764	1.00000	1.00000	1.00000	1.00000	1.00000
KAP, a. u.	0.95544	0.95611	0.95638	0.94823	0.94887	0.94799	0.95466	1.00000	1.00000	1.00000	1.00000	1.00000
RI, a. u.	0.95561	0.95624	0.95649	0.94975	0.95320	0.95397	0.95705	1.00000	1.00000	1.00000	1.00000	1.00000
ARI, a. u.	0.95334	0.95461	0.95511	0.94125	0.94574	0.94559	0.95420	1.00000	1.00000	1.00000	1.00000	1.00000
ICC, a. u.	0.95633	0.95675	0.95691	0.95113	0.95024	0.94907	0.95487	1.00000	1.00000	1.00000	1.00000	1.00000
MI, a. u.	0.89877	0.89902	0.89748	0.81079	0.56991	0.46290	0.33701	0.18121	0.16146	0.13735	0.12388	0.11247
VOI, a. u.	0.02394	0.01775	0.01528	0.07479	0.04505	0.03769	0.00857	0.00000	0.00000	0.00000	0.00000	0.00000
GCE, a. u.	0.00225	0.00161	0.00136	0.00812	0.00466	0.00388	0.00080	0.00000	0.00000	0.00000	0.00000	0.00000
PBD, a. u.	0.00001	0.00000	0.00000	0.00003	0.00003	0.00003	0.00001	0.00000	0.00000	0.00000	0.00000	0.00000
TPR, a. u.	0.95751	0.95768	0.95773	0.95191	0.94995	0.94721	0.95785	1.00000	1.00000	1.00000	1.00000	1.00000
TNR, a. u.	0.95627	0.95668	0.95685	0.95460	0.95653	0.95700	0.95742	1.00000	1.00000	1.00000	1.00000	1.00000
PRN, a. u.	0.95516	0.95582	0.95609	0.95038	0.95054	0.95096	0.95191	1.00000	1.00000	1.00000	1.00000	1.00000
FMS, a. u.	0.95633	0.95675	0.95691	0.95115	0.95025	0.94908	0.95487	1.00000	1.00000	1.00000	1.00000	1.00000
ACU, a. u.	0.95673	0.95705	0.95717	0.95378	0.95552	0.95591	0.95745	1.00000	1.00000	1.00000	1.00000	1.00000
FPR, a. u.	0.00158	0.00118	0.00100	0.00326	0.00133	0.00086	0.00043	0.00000	0.00000	0.00000	0.00000	0.00000
TIME, ms	307	392	379	347	322	312	289	263	263	264	271	264

Appendix 22. Analysis of *CTV_WB* similarity characteristics: comparison of 11th plan image with reference plan image

The threshold value, a. u.	0.0	0.1	0.2	0.3	0.4	0.5	0.6	0.7	0.8	0.9	0.95	0.99
DICE, a. u.	0.88726	0.88764	0.88776	0.87854	0.88113	0.88011	0.88552	1.00000	1.00000	1.00000	1.00000	1.00000
JAC, a. u.	0.88581	0.88657	0.88681	0.86861	0.87368	0.87169	0.88235	1.00000	1.00000	1.00000	1.00000	1.00000
AUC, a. u.	0.88780	0.88806	0.88814	0.88088	0.88457	0.88331	0.88845	1.00000	1.00000	1.00000	1.00000	1.00000
KAP, a. u.	0.88640	0.88702	0.88722	0.87414	0.87975	0.87904	0.88529	1.00000	1.00000	1.00000	1.00000	1.00000
RI, a. u.	0.88656	0.88714	0.88733	0.87649	0.88406	0.88490	0.88785	1.00000	1.00000	1.00000	1.00000	1.00000
ARI, a. u.	0.88439	0.88556	0.88594	0.86367	0.87664	0.87669	0.88480	1.00000	1.00000	1.00000	1.00000	1.00000
ICC, a. u.	0.88725	0.88764	0.88776	0.87852	0.88112	0.88011	0.88552	1.00000	1.00000	1.00000	1.00000	1.00000
MI, a. u.	0.83372	0.83387	0.83218	0.73393	0.52787	0.42877	0.31222	0.18121	0.16146	0.13735	0.12388	0.11247
VOI, a. u.	0.02260	0.01702	0.01523	0.10409	0.04441	0.03670	0.00906	0.00000	0.00000	0.00000	0.00000	0.00000
GCE, a. u.	0.00215	0.00157	0.00137	0.01224	0.00464	0.00380	0.00086	0.00000	0.00000	0.00000	0.00000	0.00000
PBD, a. u.	0.00001	0.00000	0.00000	0.00004	0.00003	0.00003	0.00001	0.00000	0.00000	0.00000	0.00000	0.00000
TPR, a. u.	0.88845	0.88858	0.88859	0.87661	0.88195	0.87883	0.88866	1.00000	1.00000	1.00000	1.00000	1.00000
TNR, a. u.	0.88715	0.88755	0.88770	0.88515	0.88718	0.88780	0.88825	1.00000	1.00000	1.00000	1.00000	1.00000
PRN, a. u.	0.88606	0.88670	0.88693	0.88049	0.88031	0.88140	0.88240	1.00000	1.00000	1.00000	1.00000	1.00000
FMS, a. u.	0.88726	0.88764	0.88776	0.87854	0.88113	0.88011	0.88552	1.00000	1.00000	1.00000	1.00000	1.00000
ACU, a. u.	0.88763	0.88792	0.88802	0.88256	0.88638	0.88680	0.88828	1.00000	1.00000	1.00000	1.00000	1.00000
FPR, a. u.	0.00155	0.00116	0.00101	0.00356	0.00153	0.00091	0.00046	0.00000	0.00000	0.00000	0.00000	0.00000
TIME, ms	323	437	445	380	299	334	279	267	259	270	284	257

Appendix 23. Analysis of *CTV_WB* similarity characteristics: comparison of 12th plan image with reference plan image

The threshold value, a. u.	0.0	0.1	0.2	0.3	0.4	0.5	0.6	0.7	0.8	0.9	0.95	0.99
DICE, a. u.	0.94618	0.94662	0.94673	0.94420	0.94028	0.93852	0.94358	1.00000	1.00000	1.00000	1.00000	1.00000
JAC, a. u.	0.94449	0.94537	0.94559	0.94056	0.93282	0.92936	0.93934	1.00000	1.00000	1.00000	1.00000	1.00000
AUC, a. u.	0.94682	0.94713	0.94719	0.94557	0.94335	0.94186	0.94756	1.00000	1.00000	1.00000	1.00000	1.00000
KAP, a. u.	0.94518	0.94590	0.94608	0.94260	0.93891	0.93735	0.94327	1.00000	1.00000	1.00000	1.00000	1.00000
RI, a. u.	0.94537	0.94604	0.94621	0.94342	0.94322	0.94373	0.94671	1.00000	1.00000	1.00000	1.00000	1.00000
ARI, a. u.	0.94285	0.94419	0.94454	0.93876	0.93579	0.93480	0.94262	1.00000	1.00000	1.00000	1.00000	1.00000
ICC, a. u.	0.94617	0.94662	0.94672	0.94419	0.94027	0.93851	0.94358	1.00000	1.00000	1.00000	1.00000	1.00000
MI, a. u.	0.88838	0.88878	0.88678	0.81728	0.56389	0.45689	0.33222	0.18121	0.16146	0.13735	0.12388	0.11247
VOI, a. u.	0.02588	0.01944	0.01793	0.04443	0.04488	0.03976	0.01172	0.00000	0.00000	0.00000	0.00000	0.00000
GCE, a. u.	0.00250	0.00183	0.00165	0.00445	0.00465	0.00414	0.00115	0.00000	0.00000	0.00000	0.00000	0.00000
PBD, a. u.	0.00001	0.00000	0.00000	0.00001	0.00003	0.00004	0.00002	0.00000	0.00000	0.00000	0.00000	0.00000
TPR, a. u.	0.94761	0.94778	0.94776	0.94540	0.94019	0.93681	0.94787	1.00000	1.00000	1.00000	1.00000	1.00000
TNR, a. u.	0.94603	0.94648	0.94663	0.94575	0.94651	0.94692	0.94725	1.00000	1.00000	1.00000	1.00000	1.00000
PRN, a. u.	0.94475	0.94546	0.94570	0.94300	0.94038	0.94023	0.93934	1.00000	1.00000	1.00000	1.00000	1.00000
FMS, a. u.	0.94618	0.94662	0.94673	0.94420	0.94028	0.93852	0.94358	1.00000	1.00000	1.00000	1.00000	1.00000
ACU, a. u.	0.94662	0.94695	0.94704	0.94564	0.94554	0.94579	0.94729	1.00000	1.00000	1.00000	1.00000	1.00000
FPR, a. u.	0.00184	0.00139	0.00124	0.00212	0.00136	0.00095	0.00062	0.00000	0.00000	0.00000	0.00000	0.00000
TIME, ms.	338	407	431	372	337	300	291	265	260	280	245	269

Appendix 24. Analysis of *CTV_WB* similarity characteristics: comparison of 13th plan image with reference plan image

The threshold value, a. u.	0.0	0.1	0.2	0.3	0.4	0.5	0.6	0.7	0.8	0.9	0.95	0.99
DICE, a. u.	0.95626	0.95663	0.95675	0.95006	0.95006	0.94897	0.95432	1.00000	1.00000	1.00000	1.00000	1.00000
JAC, a. u.	0.95477	0.95549	0.95573	0.94248	0.94248	0.94034	0.95091	1.00000	1.00000	1.00000	1.00000	1.00000
AUC, a. u.	0.95684	0.95709	0.95716	0.95108	0.95245	0.95184	0.95749	1.00000	1.00000	1.00000	1.00000	1.00000
KAP, a. u.	0.95538	0.95597	0.95617	0.94673	0.94867	0.94787	0.95408	1.00000	1.00000	1.00000	1.00000	1.00000
RI, a. u.	0.95554	0.95610	0.95629	0.94851	0.95305	0.95387	0.95684	1.00000	1.00000	1.00000	1.00000	1.00000
ARI, a. u.	0.95331	0.95442	0.95480	0.93878	0.94551	0.94547	0.95355	1.00000	1.00000	1.00000	1.00000	1.00000
ICC, a. u.	0.95626	0.95662	0.95674	0.95004	0.95005	0.94896	0.95432	1.00000	1.00000	1.00000	1.00000	1.00000
MI, a. u.	0.89900	0.89885	0.89692	0.80547	0.56914	0.46273	0.33648	0.18121	0.16146	0.13735	0.12388	0.11247
VOI, a. u.	0.02337	0.01799	0.01628	0.08164	0.04526	0.03769	0.00977	0.00000	0.00000	0.00000	0.00000	0.00000
GCE, a. u.	0.00222	0.00166	0.00147	0.00926	0.00470	0.00389	0.00093	0.00000	0.00000	0.00000	0.00000	0.00000
PBD, a. u.	0.00001	0.00000	0.00000	0.00003	0.00003	0.00003	0.00001	0.00000	0.00000	0.00000	0.00000	0.00000
TPR, a. u.	0.95755	0.95767	0.95765	0.94592	0.94820	0.94673	0.95771	1.00000	1.00000	1.00000	1.00000	1.00000
TNR, a. u.	0.95613	0.95650	0.95667	0.95624	0.95671	0.95695	0.95727	1.00000	1.00000	1.00000	1.00000	1.00000
PRN, a. u.	0.95498	0.95558	0.95584	0.95424	0.95193	0.95123	0.95096	1.00000	1.00000	1.00000	1.00000	1.00000
FMS, a. u.	0.95626	0.95663	0.95675	0.95006	0.95006	0.94897	0.95432	1.00000	1.00000	1.00000	1.00000	1.00000
ACU, a. u.	0.95665	0.95693	0.95702	0.95311	0.95540	0.95581	0.95730	1.00000	1.00000	1.00000	1.00000	1.00000
FPR, a. u.	0.00163	0.00126	0.00109	0.00152	0.00105	0.00081	0.00049	0.00000	0.00000	0.00000	0.00000	0.00000
TIME, ms	331	431	430	351	310	335	288	281	261	275	266	262

Appendix 25. Analysis of *CTV_WB* similarity characteristics: comparison of 14th plan image with reference plan image

The threshold value, a. u.	0.0	0.1	0.2	0.3	0.4	0.5	0.6	0.7	0.8	0.9	0.95	0.99
DICE, a. u.	0.95605	0.95639	0.95653	0.95193	0.94930	0.94797	0.95327	1.00000	1.00000	1.00000	1.00000	1.00000
JAC, a. u.	0.95433	0.95501	0.95531	0.94617	0.94099	0.93837	0.94883	1.00000	1.00000	1.00000	1.00000	1.00000
AUC, a. u.	0.95666	0.95693	0.95703	0.95450	0.95325	0.95190	0.95744	1.00000	1.00000	1.00000	1.00000	1.00000
KAP, a. u.	0.95504	0.95559	0.95583	0.94938	0.94776	0.94674	0.95295	1.00000	1.00000	1.00000	1.00000	1.00000
RI, a. u.	0.95522	0.95575	0.95598	0.95069	0.95257	0.95342	0.95655	1.00000	1.00000	1.00000	1.00000	1.00000
ARI, a. u.	0.95266	0.95371	0.95418	0.94329	0.94429	0.94406	0.95226	1.00000	1.00000	1.00000	1.00000	1.00000
ICC, a. u.	0.95604	0.95638	0.95653	0.95192	0.94929	0.94796	0.95327	1.00000	1.00000	1.00000	1.00000	1.00000
MI, a. u.	0.89734	0.89717	0.89551	0.81655	0.56828	0.46127	0.33554	0.18121	0.16146	0.13735	0.12388	0.11247
VOI, a. u.	0.02669	0.02143	0.01921	0.06494	0.04931	0.04157	0.01222	0.00000	0.00000	0.00000	0.00000	0.00000
GCE, a. u.	0.00254	0.00201	0.00178	0.00707	0.00519	0.00434	0.00121	0.00000	0.00000	0.00000	0.00000	0.00000
PBD, a. u.	0.00001	0.00001	0.00000	0.00002	0.00003	0.00004	0.00002	0.00000	0.00000	0.00000	0.00000	0.00000
TPR, a. u.	0.95733	0.95758	0.95762	0.95522	0.95048	0.94715	0.95776	1.00000	1.00000	1.00000	1.00000	1.00000
TNR, a. u.	0.95600	0.95628	0.95644	0.95378	0.95601	0.95664	0.95711	1.00000	1.00000	1.00000	1.00000	1.00000
PRN, a. u.	0.95477	0.95519	0.95545	0.94867	0.94813	0.94878	0.94883	1.00000	1.00000	1.00000	1.00000	1.00000
FMS, a. u.	0.95605	0.95639	0.95653	0.95193	0.94930	0.94797	0.95327	1.00000	1.00000	1.00000	1.00000	1.00000
ACU, a. u.	0.95649	0.95675	0.95687	0.95422	0.95516	0.95558	0.95716	1.00000	1.00000	1.00000	1.00000	1.00000
FPR, a. u.	0.00176	0.00149	0.00132	0.00399	0.00175	0.00112	0.00065	0.00000	0.00000	0.00000	0.00000	0.00000
TIME, ms	326	440	404	368	320	325	284	254	253	256	266	275

Appendix 26. Analysis of *CTV_WB* similarity characteristics: comparison of 15th plan image with reference plan image

The threshold value, a. u.	0.0	0.1	0.2	0.3	0.4	0.5	0.6	0.7	0.8	0.9	0.95	0.99
DICE, a. u.	0.99526	0.99600	0.99684	0.98599	0.91003	0.92408	0.82681	0.62121	0.91851	0.87091	0.83639	0.80817
JAC, a. u.	0.99056	0.99203	0.99370	0.97236	0.87000	0.85888	0.70475	0.45055	0.84929	0.77133	0.71880	0.67809
AUC, a. u.	0.99584	0.99654	0.99735	0.98968	0.94177	0.98465	0.98490	0.98282	0.99785	0.99709	0.99663	0.99638
KAP, a. u.	0.99248	0.99369	0.99505	0.97989	0.90172	0.91388	0.81197	0.60634	0.91637	0.86803	0.83311	0.80467
RI, a. u.	0.99302	0.99417	0.99543	0.98316	0.92636	0.96454	0.94525	0.93539	0.99164	0.98864	0.98684	0.98584
ARI, a. u.	0.98598	0.98827	0.99081	0.96549	0.88366	0.89300	0.78507	0.58419	0.91232	0.86285	0.82736	0.79872
ICC, a. u.	0.99524	0.99599	0.99683	0.98595	0.90998	0.92401	0.82670	0.62108	0.91849	0.87089	0.83637	0.80814
MI, a. u.	0.91692	0.91875	0.92132	0.81531	0.51164	0.41798	0.27200	0.12081	0.14443	0.11797	0.10368	0.09240
VOI, a. u.	0.06597	0.05680	0.04627	0.13909	0.18350	0.21580	0.26576	0.27030	0.05606	0.07002	0.07752	0.08102
GCE, a. u.	0.00699	0.00584	0.00457	0.01689	0.02698	0.03390	0.04802	0.04848	0.00776	0.01012	0.01139	0.01196
PBD, a. u.	0.00002	0.00002	0.00001	0.00006	0.00018	0.00032	0.00082	0.00239	0.00035	0.00058	0.00077	0.00093
TPR, a. u.	0.99330	0.99455	0.99604	0.98503	0.94442	0.98813	1.00000	1.00000	1.00000	1.00000	1.00000	1.00000
TNR, a. u.	0.99837	0.99853	0.99866	0.99433	0.93912	0.98117	0.96980	0.96564	0.99570	0.99417	0.99326	0.99276
PRN, a. u.	0.99721	0.99745	0.99764	0.98694	0.87806	0.86783	0.70475	0.45055	0.84929	0.77133	0.71880	0.67809
FMS, a. u.	0.99526	0.99600	0.99684	0.98599	0.91003	0.92408	0.82681	0.62121	0.91851	0.87091	0.83639	0.80817
ACU, a. u.	0.99650	0.99707	0.99771	0.99151	0.93994	0.98194	0.97183	0.96658	0.99580	0.99429	0.99337	0.99287
FPR, a. u.	0.00163	0.00147	0.00134	0.00567	0.01480	0.01883	0.03020	0.03436	0.00430	0.00583	0.00674	0.00724
TIME, ms	371	378	472	379	379	390	408	344	302	287	297	282

Appendix 27. Analysis of *PTV_WB* similarity characteristics: comparison of 1st plan image with reference plan image

The threshold value, a. u.	0.0	0.1	0.2	0.3	0.4	0.5	0.6	0.7	0.8	0.9	0.95	0.99
DICE, a. u.	0.88462	0.88537	0.88591	0.88944	0.86000	0.84020	0.75147	0.55463	0.82872	0.78837	0.75774	0.73328
JAC, a. u.	0.86972	0.87118	0.87222	0.87909	0.82338	0.78783	0.64501	0.40081	0.76787	0.70135	0.65430	0.61866
AUC, a. u.	0.88953	0.89038	0.89112	0.88961	0.88656	0.88560	0.88576	0.88263	0.89697	0.89729	0.89704	0.89692
KAP, a. u.	0.87531	0.87665	0.87761	0.88519	0.85293	0.83248	0.73888	0.54131	0.82688	0.78592	0.75491	0.73027
RI, a. u.	0.87712	0.87842	0.87936	0.88798	0.87629	0.87303	0.85362	0.84202	0.89287	0.89036	0.88873	0.88785
ARI, a. u.	0.85403	0.85663	0.85850	0.87510	0.83762	0.81657	0.71592	0.52161	0.82341	0.78148	0.74995	0.72511
ICC, a. u.	0.88457	0.88533	0.88586	0.88941	0.85995	0.84015	0.75138	0.55451	0.82870	0.78835	0.75772	0.73326
MI, a. u.	0.77426	0.77686	0.77916	0.73141	0.46672	0.37499	0.24512	0.10558	0.12812	0.10574	0.09327	0.08344
VOI, a. u.	0.17145	0.16156	0.15304	0.09202	0.16528	0.17419	0.23218	0.24419	0.04932	0.06050	0.06731	0.07040
GCE, a. u.	0.02295	0.02162	0.02066	0.01199	0.02337	0.02608	0.04103	0.04346	0.00668	0.00866	0.00983	0.01035
PBD, a. u.	0.00006	0.00006	0.00006	0.00004	0.00016	0.00025	0.00070	0.00220	0.00030	0.00050	0.00066	0.00080
TPR, a. u.	0.89388	0.89530	0.89688	0.87927	0.88452	0.88467	0.89682	0.89595	0.89753	0.89949	0.89983	0.90003
TNR, a. u.	0.88519	0.88547	0.88537	0.89996	0.88860	0.88652	0.87471	0.86931	0.89641	0.89508	0.89425	0.89381
PRN, a. u.	0.87555	0.87565	0.87520	0.89984	0.83680	0.79999	0.64667	0.40162	0.76971	0.70168	0.65441	0.61866
FMS, a. u.	0.88462	0.88537	0.88591	0.88944	0.86000	0.84020	0.75147	0.55463	0.82872	0.78837	0.75774	0.73328
ACU, a. u.	0.88843	0.88909	0.88957	0.89397	0.88800	0.88632	0.87620	0.87003	0.89643	0.89517	0.89434	0.89390
FPR, a. u.	0.01485	0.01457	0.01467	0.00008	0.01143	0.01351	0.02532	0.03072	0.00362	0.00495	0.00578	0.00623
TIME, ms	375	438	453	328	313	344	359	328	250	266	266	250

Appendix 28. Analysis of *PTV_WB* similarity characteristics: comparison of 2nd plan image with reference plan image

The threshold value, a. u.	0.0	0.1	0.2	0.3	0.4	0.5	0.6	0.7	0.8	0.9	0.95	0.99
DICE, a. u.	0.95602	0.95640	0.95639	0.95020	0.95004	0.95010	0.95610	0.95538	0.95615	0.95720	0.95738	1.00000
JAC, a. u.	0.95456	0.95531	0.95529	0.94301	0.94271	0.94283	0.95472	0.95328	0.95482	0.95691	0.95727	1.00000
AUC, a. u.	0.95627	0.95659	0.95660	0.95063	0.95059	0.95027	0.95613	0.95538	0.95615	0.95720	0.95738	1.00000
KAP, a. u.	0.95515	0.95576	0.95576	0.94725	0.94877	0.94921	0.95600	0.95532	0.95612	0.95719	0.95738	1.00000
RI, a. u.	0.95531	0.95588	0.95588	0.94913	0.95317	0.95430	0.95712	0.95726	0.95736	0.95747	0.95748	1.00000
ARI, a. u.	0.95311	0.95426	0.95426	0.94021	0.94592	0.94725	0.95579	0.95520	0.95606	0.95718	0.95737	1.00000
ICC, a. u.	0.95602	0.95640	0.95639	0.95018	0.95003	0.95009	0.95610	0.95538	0.95615	0.95720	0.95738	1.00000
MI, a. u.	0.89992	0.90005	0.89762	0.79300	0.55240	0.45842	0.33782	0.16932	0.15181	0.13032	0.11796	0.11224
VOI, a. u.	0.02435	0.01863	0.01864	0.07196	0.03952	0.02910	0.00444	0.00269	0.00157	0.00033	0.00012	0.00000
GCE, a. u.	0.00218	0.00161	0.00161	0.00834	0.00430	0.00317	0.00037	0.00023	0.00012	0.00002	0.00001	0.00000
PBD, a. u.	0.00001	0.00000	0.00000	0.00003	0.00003	0.00003	0.00001	0.00001	0.00000	0.00000	0.00000	0.00000
TPR, a. u.	0.95577	0.95624	0.95628	0.94432	0.94391	0.94309	0.95477	0.95328	0.95482	0.95691	0.95727	1.00000
TNR, a. u.	0.95677	0.95694	0.95692	0.95695	0.95728	0.95745	0.95748	0.95749	0.95749	0.95749	0.95749	1.00000
PRN, a. u.	0.95627	0.95656	0.95650	0.95615	0.95625	0.95721	0.95743	0.95749	0.95749	0.95749	0.95749	1.00000
FMS, a. u.	0.95602	0.95640	0.95639	0.95020	0.95004	0.95010	0.95610	0.95538	0.95615	0.95720	0.95738	1.00000
ACU, a. u.	0.95640	0.95668	0.95668	0.95329	0.95533	0.95589	0.95730	0.95737	0.95743	0.95748	0.95748	1.00000
FPR, a. u.	0.00072	0.00054	0.00057	0.00054	0.00021	0.00003	0.00000	0.00000	0.00000	0.00000	0.00000	0.00000
TIME, ms	344	359	359	328	281	281	265	250	250	234	250	250

Appendix 29. Analysis of *PTV_WB* similarity characteristics: comparison of 3rd plan image with reference plan image

The threshold value, a. u.	0.0	0.1	0.2	0.3	0.4	0.5	0.6	0.7	0.8	0.9	0.95	0.99
DICE, a. u.	0.94543	0.94572	0.94572	0.93867	0.94000	0.94025	0.94667	0.94677	0.94685	0.94714	1.00000	1.00000
JAC, a. u.	0.94363	0.94420	0.94420	0.93026	0.93288	0.93337	0.94611	0.94630	0.94646	0.94705	1.00000	1.00000
AUC, a. u.	0.94583	0.94606	0.94610	0.93888	0.94027	0.94042	0.94670	0.94677	0.94685	0.94714	1.00000	1.00000
KAP, a. u.	0.94436	0.94483	0.94484	0.93522	0.93878	0.93940	0.94663	0.94676	0.94684	0.94714	1.00000	1.00000
RI, a. u.	0.94455	0.94499	0.94502	0.93745	0.94305	0.94422	0.94709	0.94719	0.94720	0.94723	1.00000	1.00000
ARI, a. u.	0.94183	0.94273	0.94277	0.92700	0.93601	0.93755	0.94655	0.94673	0.94682	0.94714	1.00000	1.00000
ICC, a. u.	0.94542	0.94571	0.94571	0.93865	0.93999	0.94025	0.94667	0.94677	0.94685	0.94714	1.00000	1.00000
MI, a. u.	0.88782	0.88725	0.88500	0.77961	0.54698	0.45414	0.33559	0.16871	0.15082	0.12905	0.12328	0.11224
VOI, a. u.	0.02923	0.02496	0.02470	0.07931	0.03770	0.02774	0.00202	0.00071	0.00052	0.00012	0.00000	0.00000
GCE, a. u.	0.00269	0.00225	0.00222	0.00975	0.00417	0.00300	0.00015	0.00005	0.00004	0.00001	0.00000	0.00000
PBD, a. u.	0.00001	0.00001	0.00001	0.00003	0.00003	0.00003	0.00000	0.00000	0.00000	0.00000	0.00000	0.00000
TPR, a. u.	0.94558	0.94586	0.94599	0.93070	0.93339	0.93363	0.94616	0.94630	0.94646	0.94705	1.00000	1.00000
TNR, a. u.	0.94608	0.94627	0.94620	0.94706	0.94715	0.94721	0.94724	0.94724	0.94724	0.94724	1.00000	1.00000
PRN, a. u.	0.94528	0.94557	0.94544	0.94678	0.94671	0.94697	0.94718	0.94724	0.94724	0.94724	1.00000	1.00000
FMS, a. u.	0.94543	0.94572	0.94572	0.93867	0.94000	0.94025	0.94667	0.94677	0.94685	0.94714	1.00000	1.00000
ACU, a. u.	0.94589	0.94612	0.94613	0.94232	0.94514	0.94573	0.94716	0.94721	0.94722	0.94724	1.00000	1.00000
FPR, a. u.	0.00116	0.00097	0.00104	0.00018	0.00009	0.00003	0.00000	0.00000	0.00000	0.00000	0.00000	0.00000
TIME, ms	311	355	370	326	266	251	252	222	252	222	234	234

Appendix 30. Analysis of *PTV_WB* similarity characteristics: comparison of 4th plan image with reference plan image

The threshold value, a. u.	0.0	0.1	0.2	0.3	0.4	0.5	0.6	0.7	0.8	0.9	0.95	0.99
DICE, a. u.	0.94748	0.94777	0.94780	0.94290	0.94000	0.94093	0.94612	0.94684	0.94753	0.94864	0.94861	1.00000
JAC, a. u.	0.94603	0.94662	0.94668	0.93696	0.93124	0.93306	0.94333	0.94476	0.94613	0.94836	0.94828	1.00000
AUC, a. u.	0.94766	0.94790	0.94793	0.94388	0.94129	0.94178	0.94613	0.94684	0.94753	0.94864	0.94861	1.00000
KAP, a. u.	0.94661	0.94710	0.94716	0.94046	0.93849	0.93996	0.94592	0.94678	0.94749	0.94864	0.94860	1.00000
RI, a. u.	0.94677	0.94723	0.94729	0.94200	0.94376	0.94547	0.94818	0.94870	0.94880	0.94891	0.94891	1.00000
ARI, a. u.	0.94459	0.94551	0.94563	0.93461	0.93508	0.93783	0.94549	0.94666	0.94743	0.94863	0.94859	1.00000
ICC, a. u.	0.94747	0.94777	0.94780	0.94289	0.93999	0.94092	0.94612	0.94684	0.94753	0.94864	0.94861	1.00000
MI, a. u.	0.89188	0.89148	0.88935	0.79064	0.54353	0.45282	0.33257	0.16781	0.15041	0.12916	0.11679	0.11224
VOI, a. u.	0.02396	0.01930	0.01874	0.06422	0.04719	0.03242	0.00809	0.00266	0.00163	0.00033	0.00032	0.00000
GCE, a. u.	0.00216	0.00170	0.00164	0.00693	0.00515	0.00344	0.00075	0.00022	0.00013	0.00002	0.00002	0.00000
PBD, a. u.	0.00001	0.00000	0.00000	0.00002	0.00004	0.00003	0.00001	0.00001	0.00001	0.00000	0.00000	0.00000
TPR, a. u.	0.94694	0.94723	0.94729	0.94015	0.93416	0.93486	0.94333	0.94476	0.94613	0.94836	0.94828	1.00000
TNR, a. u.	0.94839	0.94857	0.94858	0.94761	0.94842	0.94871	0.94893	0.94893	0.94893	0.94893	0.94893	1.00000
PRN, a. u.	0.94801	0.94832	0.94832	0.94567	0.94592	0.94708	0.94893	0.94893	0.94893	0.94893	0.94893	1.00000
FMS, a. u.	0.94748	0.94777	0.94780	0.94290	0.94000	0.94093	0.94612	0.94684	0.94753	0.94864	0.94861	1.00000
ACU, a. u.	0.94785	0.94808	0.94811	0.94545	0.94634	0.94720	0.94855	0.94882	0.94886	0.94892	0.94892	1.00000
FPR, a. u.	0.00054	0.00036	0.00035	0.00132	0.00051	0.00022	0.00000	0.00000	0.00000	0.00000	0.00000	0.00000
TIME, ms	297	328	343	328	313	297	266	234	250	234	250	234

Appendix 31. Analysis of *PTV_WB* similarity characteristics: comparison of 5th plan image with reference plan image

The threshold value, a. u.	0.0	0.1	0.2	0.3	0.4	0.5	0.6	0.7	0.8	0.9	0.95	0.99
DICE, a. u.	0.85751	0.85784	0.85763	0.85666	0.86001	0.86083	0.86569	0.86502	0.86572	0.86667	0.86683	1.00000
JAC, a. u.	0.84830	0.84893	0.84854	0.84663	0.85320	0.85481	0.86447	0.86311	0.86451	0.86641	0.86673	1.00000
AUC, a. u.	0.86109	0.86144	0.86142	0.85699	0.86048	0.86111	0.86570	0.86502	0.86572	0.86667	0.86683	1.00000
KAP, a. u.	0.85183	0.85244	0.85219	0.85253	0.85884	0.86009	0.86561	0.86496	0.86569	0.86666	0.86683	1.00000
RI, a. u.	0.85287	0.85349	0.85330	0.85524	0.86292	0.86429	0.86660	0.86672	0.86681	0.86691	0.86692	1.00000
ARI, a. u.	0.83870	0.83993	0.83956	0.84275	0.85619	0.85846	0.86542	0.86486	0.86563	0.86665	0.86682	1.00000
ICC, a. u.	0.85748	0.85781	0.85761	0.85663	0.86000	0.86082	0.86569	0.86502	0.86572	0.86667	0.86683	1.00000
MI, a. u.	0.77425	0.77438	0.77194	0.70355	0.49973	0.41615	0.30592	0.15330	0.13745	0.11800	0.10681	0.11224
VOI, a. u.	0.10793	0.10283	0.10354	0.09094	0.03642	0.02476	0.00390	0.00243	0.00142	0.00030	0.00011	0.00000
GCE, a. u.	0.01404	0.01341	0.01359	0.01164	0.00399	0.00262	0.00033	0.00020	0.00011	0.00002	0.00001	0.00000
PBD, a. u.	0.00004	0.00004	0.00004	0.00004	0.00003	0.00002	0.00001	0.00001	0.00000	0.00000	0.00000	0.00000
TPR, a. u.	0.86599	0.86636	0.86646	0.84736	0.85420	0.85535	0.86447	0.86311	0.86451	0.86641	0.86673	1.00000
TNR, a. u.	0.85619	0.85653	0.85638	0.86662	0.86675	0.86686	0.86693	0.86693	0.86693	0.86693	0.86693	1.00000
PRN, a. u.	0.84920	0.84948	0.84899	0.86616	0.86589	0.86637	0.86693	0.86693	0.86693	0.86693	0.86693	1.00000
FMS, a. u.	0.85751	0.85784	0.85763	0.85666	0.86001	0.86083	0.86569	0.86502	0.86572	0.86667	0.86683	1.00000
ACU, a. u.	0.85984	0.86015	0.86006	0.86104	0.86492	0.86561	0.86676	0.86682	0.86687	0.86692	0.86692	1.00000
FPR, a. u.	0.01074	0.01040	0.01055	0.00031	0.00017	0.00007	0.00000	0.00000	0.00000	0.00000	0.00000	0.00000
TIME, ms	406	438	468	328	281	297	250	281	250	250	234	328

Appendix 32. Analysis of *PTV_WB* similarity characteristics: comparison of 6th plan image with reference plan image

The threshold value, a. u.	0.0	0.1	0.2	0.3	0.4	0.5	0.6	0.7	0.8	0.9	0.95	0.99
DICE, a. u.	0.99616	0.99698	0.99781	0.98593	0.93411	0.90824	0.80076	0.55307	0.89531	0.86004	0.82702	0.79486
JAC, a. u.	0.99235	0.99397	0.99563	0.97225	0.80849	0.83191	0.66773	0.38223	0.81046	0.75445	0.70507	0.65956
AUC, a. u.	0.99623	0.99703	0.99787	0.99397	0.97707	0.98380	0.98179	0.97760	0.99721	0.99683	0.99642	0.99608
KAP, a. u.	0.99389	0.99522	0.99655	0.98009	0.87384	0.89597	0.78330	0.53497	0.89254	0.85693	0.82354	0.79109
RI, a. u.	0.99431	0.99556	0.99681	0.98362	0.93362	0.95736	0.93537	0.91687	0.98917	0.98765	0.98602	0.98466
ARI, a. u.	0.98857	0.99108	0.99358	0.96626	0.83256	0.87127	0.75234	0.50933	0.88742	0.85136	0.81750	0.78474
ICC, a. u.	0.99615	0.99697	0.99780	0.98590	0.89397	0.90816	0.80063	0.55290	0.89529	0.86002	0.82700	0.79483
MI, a. u.	0.92576	0.92802	0.93070	0.81195	0.46488	0.40321	0.26260	0.11098	0.13942	0.11596	0.10238	0.09123
VOI, a. u.	0.05180	0.04193	0.03195	0.12227	0.34697	0.24376	0.30110	0.32377	0.06875	0.07467	0.08119	0.08620
GCE, a. u.	0.00569	0.00444	0.00319	0.01630	0.06250	0.04022	0.05578	0.06007	0.00986	0.01090	0.01201	0.01283
PBD, a. u.	0.00002	0.00001	0.00001	0.00006	0.00046	0.00040	0.00098	0.00317	0.00046	0.00064	0.00082	0.00101
TPR, a. u.	0.99263	0.99419	0.99588	0.99925	0.99324	0.99096	0.99938	0.99986	1.00000	1.00000	1.00000	1.00000
TNR, a. u.	0.99983	0.99987	0.99986	0.98868	0.96091	0.97665	0.96420	0.95535	0.99442	0.99367	0.99284	0.99215
PRN, a. u.	0.99971	0.99978	0.99975	0.97296	0.81297	0.83827	0.66801	0.38225	0.81046	0.75445	0.70507	0.65956
FMS, a. u.	0.99616	0.99698	0.99781	0.98593	0.89411	0.90824	0.80076	0.55307	0.89531	0.86004	0.82702	0.79486
ACU, a. u.	0.99715	0.99778	0.99840	0.99174	0.96563	0.97821	0.96657	0.95655	0.99455	0.99379	0.99296	0.99227
FPR, a. u.	0.00017	0.00013	0.00014	0.01132	0.03909	0.02335	0.03580	0.04465	0.00558	0.00634	0.00716	0.00785
TIME, ms	328	375	500	437	436	484	515	359	254	266	266	245

Appendix 33. Analysis of *PTV_WB* similarity characteristics: comparison of 7th plan image with reference plan image

The threshold value, a. u.	0.0	0.1	0.2	0.3	0.4	0.5	0.6	0.7	0.8	0.9	0.95	0.99
DICE, a. u.	0.94445	0.94467	0.94459	0.94288	0.94012	0.94004	0.94473	0.94399	0.94475	0.94579	0.94597	1.00000
JAC, a. u.	0.94284	0.94328	0.94312	0.93970	0.93425	0.93407	0.94339	0.94191	0.94344	0.94551	0.94586	1.00000
AUC, a. u.	0.94483	0.94499	0.94497	0.94328	0.94046	0.94016	0.94473	0.94399	0.94476	0.94579	0.94597	1.00000
KAP, a. u.	0.94349	0.94386	0.94374	0.94158	0.93911	0.93930	0.94463	0.94393	0.94472	0.94578	0.94596	1.00000
RI, a. u.	0.94366	0.94401	0.94391	0.94239	0.94262	0.94346	0.94571	0.94585	0.94595	0.94605	0.94607	1.00000
ARI, a. u.	0.94122	0.94193	0.94173	0.93846	0.93683	0.93770	0.94443	0.94381	0.94466	0.94577	0.94596	1.00000
ICC, a. u.	0.94445	0.94467	0.94459	0.94287	0.94012	0.94003	0.94473	0.94399	0.94475	0.94579	0.94597	1.00000
MI, a. u.	0.88807	0.88702	0.88421	0.80207	0.54949	0.45547	0.33384	0.16730	0.15000	0.12877	0.11656	0.11224
VOI, a. u.	0.02657	0.02317	0.02409	0.03710	0.03240	0.02450	0.00426	0.00265	0.00155	0.00032	0.00012	0.00000
GCE, a. u.	0.00242	0.00206	0.00216	0.00369	0.00344	0.00260	0.00036	0.00022	0.00012	0.00002	0.00001	0.00000
PBD, a. u.	0.00001	0.00001	0.00001	0.00001	0.00002	0.00002	0.00001	0.00001	0.00000	0.00000	0.00000	0.00000
TPR, a. u.	0.94470	0.94479	0.94491	0.94103	0.93498	0.93427	0.94339	0.94191	0.94344	0.94551	0.94586	1.00000
TNR, a. u.	0.94496	0.94519	0.94504	0.94553	0.94595	0.94605	0.94607	0.94607	0.94607	0.94607	0.94607	1.00000
PRN, a. u.	0.94421	0.94456	0.94428	0.94474	0.94532	0.94587	0.94607	0.94607	0.94607	0.94607	0.94607	1.00000
FMS, a. u.	0.94445	0.94467	0.94459	0.94288	0.94012	0.94004	0.94473	0.94399	0.94475	0.94579	0.94597	1.00000
ACU, a. u.	0.94486	0.94504	0.94499	0.94423	0.94435	0.94477	0.94589	0.94596	0.94601	0.94606	0.94607	1.00000
FPR, a. u.	0.00111	0.00089	0.00104	0.00054	0.00013	0.00002	0.00000	0.00000	0.00000	0.00000	0.00000	0.00000
TIME, ms	328	343	406	313	297	281	250	250	266	250	250	250

Appendix 34. Analysis of *PTV_WB* similarity characteristics: comparison of 8th plan image with reference plan image

The threshold value, a. u.	0.0	0.1	0.2	0.3	0.4	0.5	0.6	0.7	0.8	0.9	0.95	0.99
DICE, a. u.	0.99596	0.99671	0.99754	0.99017	0.95672	0.93341	0.83203	0.61536	0.91579	0.87081	0.83746	0.81095
JAC, a. u.	0.99196	0.99344	0.99510	0.98052	0.91703	0.87514	0.71237	0.44442	0.84465	0.77119	0.72037	0.68201
AUC, a. u.	0.99609	0.99681	0.99765	0.99152	0.98911	0.98717	0.98517	0.98266	0.99781	0.99711	0.99668	0.99646
KAP, a. u.	0.99358	0.99479	0.99613	0.98619	0.94900	0.92475	0.81773	0.60048	0.91360	0.86797	0.83422	0.80752
RI, a. u.	0.99402	0.99517	0.99642	0.98873	0.97411	0.96971	0.94722	0.93504	0.99147	0.98873	0.98702	0.98613
ARI, a. u.	0.98799	0.99029	0.99280	0.97672	0.93225	0.90687	0.79166	0.57845	0.90949	0.86283	0.82854	0.80166
ICC, a. u.	0.99595	0.99670	0.99754	0.99014	0.95667	0.93335	0.83193	0.61523	0.91577	0.87079	0.83744	0.81092
MI, a. u.	0.92427	0.92611	0.92880	0.81778	0.52645	0.42105	0.27326	0.11852	0.14237	0.11711	0.10330	0.09243
VOI, a. u.	0.05484	0.04575	0.03574	0.09662	0.17401	0.18979	0.25953	0.27091	0.05690	0.06948	0.07664	0.07973
GCE, a. u.	0.00598	0.00483	0.00358	0.01126	0.02531	0.02908	0.04647	0.04855	0.00790	0.01003	0.01124	0.01175
PBD, a. u.	0.00002	0.00001	0.00001	0.00004	0.00018	0.00028	0.00079	0.00245	0.00036	0.00058	0.00076	0.00091
TPR, a. u.	0.99253	0.99389	0.99557	0.98482	0.99225	0.99043	0.99938	0.99986	1.00000	1.00000	1.00000	1.00000
TNR, a. u.	0.99966	0.99973	0.99973	0.99821	0.98597	0.98391	0.97096	0.96546	0.99561	0.99423	0.99335	0.99291
PRN, a. u.	0.99942	0.99954	0.99953	0.99557	0.92365	0.88260	0.71269	0.44444	0.84465	0.77119	0.72037	0.68201
FMS, a. u.	0.99596	0.99671	0.99754	0.99017	0.95672	0.93341	0.83203	0.61536	0.91579	0.87081	0.83746	0.81095
ACU, a. u.	0.99700	0.99758	0.99821	0.99434	0.98689	0.98462	0.97287	0.96639	0.99572	0.99434	0.99347	0.99302
FPR, a. u.	0.00034	0.00027	0.00027	0.00179	0.01403	0.01609	0.02904	0.03454	0.00439	0.00578	0.00665	0.00709
TIME, ms	344	406	406	328	328	312	343	344	250	265	266	250

Appendix 35. Analysis of *PTV_WB* similarity characteristics: comparison of 9th plan image with reference plan image

The threshold value, a. u.	0.0	0.1	0.2	0.3	0.4	0.5	0.6	0.7	0.8	0.9	0.95	0.99
DICE, a. u.	0.99529	0.99607	0.99683	0.98739	0.95552	0.93330	0.83235	0.61611	0.91737	0.87233	0.83921	0.81229
JAC, a. u.	0.99062	0.99217	0.99369	0.97509	0.91483	0.87494	0.71283	0.44520	0.84735	0.77357	0.72297	0.68391
AUC, a. u.	0.99536	0.99612	0.99688	0.98884	0.98788	0.98670	0.98508	0.98272	0.99785	0.99715	0.99672	0.99649
KAP, a. u.	0.99251	0.99379	0.99502	0.98231	0.94760	0.92463	0.81807	0.60127	0.91523	0.86952	0.83601	0.80889
RI, a. u.	0.99303	0.99424	0.99540	0.98562	0.97344	0.96969	0.94735	0.93524	0.99164	0.98889	0.98718	0.98625
ARI, a. u.	0.98599	0.98843	0.99074	0.97026	0.93043	0.90675	0.79207	0.57928	0.91119	0.86445	0.83040	0.80308
ICC, a. u.	0.99527	0.99606	0.99683	0.98736	0.95547	0.93324	0.83224	0.61598	0.91735	0.87231	0.83919	0.81226
MI, a. u.	0.92086	0.92278	0.92483	0.80652	0.52317	0.42028	0.27316	0.11861	0.14260	0.11727	0.10345	0.09253
VOI, a. u.	0.06109	0.05187	0.04307	0.11719	0.17965	0.19070	0.25938	0.27031	0.05598	0.06875	0.07588	0.07919
GCE, a. u.	0.00697	0.00575	0.00460	0.01437	0.02601	0.02912	0.04638	0.04842	0.00775	0.00991	0.01111	0.01166
PBD, a. u.	0.00002	0.00002	0.00001	0.00005	0.00018	0.00028	0.00079	0.00244	0.00035	0.00057	0.00075	0.00091
TPR, a. u.	0.99087	0.99235	0.99387	0.97954	0.98976	0.98938	0.99909	0.99986	1.00000	1.00000	1.00000	1.00000
TNR, a. u.	0.99985	0.99990	0.99990	0.99814	0.98599	0.98403	0.97106	0.96557	0.99570	0.99430	0.99344	0.99297
PRN, a. u.	0.99974	0.99982	0.99982	0.99537	0.92357	0.88323	0.71330	0.44523	0.84735	0.77357	0.72297	0.68391
FMS, a. u.	0.99529	0.99607	0.99683	0.98739	0.95552	0.93330	0.83235	0.61611	0.91737	0.87233	0.83921	0.81229
ACU, a. u.	0.99650	0.99711	0.99769	0.99276	0.98654	0.98461	0.97294	0.96650	0.99580	0.99441	0.99355	0.99308
FPR, a. u.	0.00015	0.00010	0.00010	0.00186	0.01401	0.01598	0.02894	0.03443	0.00430	0.00570	0.00656	0.00703
TIME, ms	359	406	422	344	328	344	359	328	250	266	250	250

Appendix 36. Analysis of *PTV_WB* similarity characteristics: comparison of 10th plan image with reference plan image

The threshold value, a. u.	0.0	0.1	0.2	0.3	0.4	0.5	0.6	0.7	0.8	0.9	0.95	0.99
DICE, a. u.	0.95361	0.95377	0.95360	0.95120	0.95001	0.94957	0.95468	0.95437	0.95537	1.00000	1.00000	1.00000
JAC, a. u.	0.95131	0.95162	0.95130	0.94653	0.94416	0.94330	0.95343	0.95281	0.95483	1.00000	1.00000	1.00000
AUC, a. u.	0.95375	0.95385	0.95368	0.95199	0.95161	0.95084	0.95556	0.95581	0.95591	1.00000	1.00000	1.00000
KAP, a. u.	0.95224	0.95251	0.95227	0.94928	0.94900	0.94879	0.95459	0.95432	0.95536	1.00000	1.00000	1.00000
RI, a. u.	0.95249	0.95276	0.95254	0.95048	0.95248	0.95317	0.95559	0.95576	0.95587	1.00000	1.00000	1.00000
ARI, a. u.	0.94902	0.94956	0.94913	0.94469	0.94672	0.94710	0.95439	0.95423	0.95533	1.00000	1.00000	1.00000
ICC, a. u.	0.95360	0.95376	0.95360	0.95119	0.95000	0.94956	0.95467	0.95437	0.95537	1.00000	1.00000	1.00000
MI, a. u.	0.89282	0.89145	0.88813	0.80288	0.55558	0.45964	0.33785	0.16982	0.15223	0.13632	0.12328	0.11224
VOI, a. u.	0.03479	0.03194	0.03358	0.05241	0.03437	0.02746	0.00427	0.00210	0.00071	0.00000	0.00000	0.00000
GCE, a. u.	0.00344	0.00317	0.00338	0.00544	0.00344	0.00275	0.00034	0.00017	0.00005	0.00000	0.00000	0.00000
PBD, a. u.	0.00001	0.00001	0.00001	0.00002	0.00002	0.00002	0.00000	0.00001	0.00000	0.00000	0.00000	0.00000
TPR, a. u.	0.95197	0.95202	0.95165	0.94913	0.94796	0.94611	0.95533	0.95579	0.95592	1.00000	1.00000	1.00000
TNR, a. u.	0.95553	0.95569	0.95572	0.95485	0.95526	0.95557	0.95579	0.95584	0.95590	1.00000	1.00000	1.00000
PRN, a. u.	0.95525	0.95553	0.95556	0.95328	0.95206	0.95305	0.95403	0.95295	0.95483	1.00000	1.00000	1.00000
FMS, a. u.	0.95361	0.95377	0.95360	0.95120	0.95001	0.94957	0.95468	0.95437	0.95537	1.00000	1.00000	1.00000
ACU, a. u.	0.95420	0.95434	0.95423	0.95320	0.95420	0.95454	0.95576	0.95584	0.95590	1.00000	1.00000	1.00000
FPR, a. u.	0.00039	0.00023	0.00021	0.00107	0.00066	0.00035	0.00014	0.00008	0.00003	0.00000	0.00000	0.00000
TIME, ms	390	422	500	297	297	297	281	250	250	250	234	234

Appendix 37. Analysis of *PTV_WB* similarity characteristics: comparison of 11th plan image with reference plan image

The threshold value, a. u.	0.0	0.1	0.2	0.3	0.4	0.5	0.6	0.7	0.8	0.9	0.95	0.99
DICE, a. u.	0.92583	0.92600	0.92581	0.91744	0.92000	0.92061	0.92700	0.92682	0.92763	1.00000	1.00000	1.00000
JAC, a. u.	0.92366	0.92400	0.92363	0.90711	0.91214	0.91332	0.92601	0.92564	0.92725	1.00000	1.00000	1.00000
AUC, a. u.	0.92592	0.92604	0.92585	0.91830	0.92134	0.92118	0.92759	0.92778	0.92800	1.00000	1.00000	1.00000
KAP, a. u.	0.92453	0.92483	0.92455	0.91318	0.91864	0.91971	0.92693	0.92679	0.92762	1.00000	1.00000	1.00000
RI, a. u.	0.92477	0.92506	0.92481	0.91595	0.92337	0.92481	0.92774	0.92788	0.92797	1.00000	1.00000	1.00000
ARI, a. u.	0.92150	0.92208	0.92158	0.90307	0.91558	0.91774	0.92678	0.92672	0.92760	1.00000	1.00000	1.00000
ICC, a. u.	0.92582	0.92599	0.92581	0.91741	0.91999	0.92060	0.92700	0.92682	0.92763	1.00000	1.00000	1.00000
MI, a. u.	0.86733	0.86621	0.86280	0.75353	0.53336	0.44368	0.32819	0.16495	0.14785	0.13632	0.12328	0.11224
VOI, a. u.	0.03251	0.02936	0.03129	0.09821	0.04322	0.02990	0.00354	0.00169	0.00051	0.00000	0.00000	0.00000
GCE, a. u.	0.00324	0.00295	0.00319	0.01203	0.00463	0.00318	0.00027	0.00013	0.00004	0.00000	0.00000	0.00000
PBD, a. u.	0.00001	0.00001	0.00001	0.00004	0.00003	0.00003	0.00000	0.00000	0.00000	0.00000	0.00000	0.00000
TPR, a. u.	0.92409	0.92418	0.92377	0.90964	0.91521	0.91451	0.92727	0.92761	0.92801	1.00000	1.00000	1.00000
TNR, a. u.	0.92775	0.92790	0.92792	0.92695	0.92747	0.92786	0.92791	0.92795	0.92799	1.00000	1.00000	1.00000
PRN, a. u.	0.92757	0.92783	0.92786	0.92537	0.92485	0.92679	0.92674	0.92603	0.92725	1.00000	1.00000	1.00000
FMS, a. u.	0.92583	0.92600	0.92581	0.91744	0.92000	0.92061	0.92700	0.92682	0.92763	1.00000	1.00000	1.00000
ACU, a. u.	0.92638	0.92653	0.92641	0.92194	0.92568	0.92641	0.92787	0.92794	0.92799	1.00000	1.00000	1.00000
FPR, a. u.	0.00026	0.00010	0.00008	0.00106	0.00053	0.00015	0.00009	0.00005	0.00002	0.00000	0.00000	0.00000
TIME, ms	313	438	422	328	281	297	265	250	266	250	234	234

Appendix 38. Analysis of *PTV_WB* similarity characteristics: comparison of 12th plan image with reference plan image

The threshold value, a. u.	0.0	0.1	0.2	0.3	0.4	0.5	0.6	0.7	0.8	0.9	0.95	0.99
DICE, a. u.	0.94384	0.94395	0.94394	0.94251	0.94000	0.93943	0.94421	0.94410	0.94481	1.00000	1.00000	1.00000
JAC, a. u.	0.94264	0.94287	0.94285	0.94000	0.93501	0.93389	0.94338	0.94317	0.94458	1.00000	1.00000	1.00000
AUC, a. u.	0.94393	0.94399	0.94398	0.94319	0.94071	0.93985	0.94456	0.94462	0.94481	1.00000	1.00000	1.00000
KAP, a. u.	0.94313	0.94332	0.94331	0.94148	0.93914	0.93875	0.94415	0.94408	0.94480	1.00000	1.00000	1.00000
RI, a. u.	0.94325	0.94344	0.94344	0.94212	0.94211	0.94261	0.94482	0.94494	0.94502	1.00000	1.00000	1.00000
ARI, a. u.	0.94145	0.94183	0.94182	0.93901	0.93720	0.93725	0.94402	0.94402	0.94479	1.00000	1.00000	1.00000
ICC, a. u.	0.94384	0.94395	0.94394	0.94251	0.93999	0.93943	0.94421	0.94410	0.94481	1.00000	1.00000	1.00000
MI, a. u.	0.89015	0.88852	0.88614	0.80477	0.55120	0.45572	0.33442	0.16805	0.15059	0.13632	0.12328	0.11224
VOI, a. u.	0.01989	0.01764	0.01753	0.03111	0.02911	0.02372	0.00301	0.00141	0.00033	0.00000	0.00000	0.00000
GCE, a. u.	0.00179	0.00160	0.00160	0.00292	0.00292	0.00242	0.00022	0.00010	0.00002	0.00000	0.00000	0.00000
PBD, a. u.	0.00000	0.00000	0.00000	0.00001	0.00002	0.00002	0.00000	0.00000	0.00000	0.00000	0.00000	0.00000
TPR, a. u.	0.94308	0.94306	0.94300	0.94228	0.93667	0.93477	0.94413	0.94424	0.94458	1.00000	1.00000	1.00000
TNR, a. u.	0.94478	0.94493	0.94496	0.94411	0.94475	0.94493	0.94499	0.94501	0.94504	1.00000	1.00000	1.00000
PRN, a. u.	0.94460	0.94485	0.94489	0.94275	0.94335	0.94414	0.94429	0.94397	0.94504	1.00000	1.00000	1.00000
FMS, a. u.	0.94384	0.94395	0.94394	0.94251	0.94000	0.93943	0.94421	0.94410	0.94481	1.00000	1.00000	1.00000
ACU, a. u.	0.94415	0.94424	0.94424	0.94358	0.94357	0.94382	0.94493	0.94499	0.94503	1.00000	1.00000	1.00000
FPR, a. u.	0.00026	0.00011	0.00009	0.00093	0.00029	0.00011	0.00005	0.00003	0.00000	0.00000	0.00000	0.00000
TIME, ms	313	343	453	313	281	281	266	250	234	250	250	250

Appendix 39. Analysis of *PTV_WB* similarity characteristics: comparison of 13th plan image with reference plan image

The threshold value, a. u.	0.0	0.1	0.2	0.3	0.4	0.5	0.6	0.7	0.8	0.9	0.95	0.99
DICE, a. u.	0.96515	0.96545	0.96543	0.95980	0.96007	0.96016	0.96652	0.96666	0.96685	1.00000	1.00000	1.00000
JAC, a. u.	0.96338	0.96398	0.96393	0.95278	0.95331	0.95348	0.96611	0.96638	0.96677	1.00000	1.00000	1.00000
AUC, a. u.	0.96528	0.96553	0.96552	0.96019	0.96053	0.96035	0.96660	0.96686	0.96693	1.00000	1.00000	1.00000
KAP, a. u.	0.96410	0.96459	0.96456	0.95693	0.95891	0.95934	0.96649	0.96665	0.96685	1.00000	1.00000	1.00000
RI, a. u.	0.96429	0.96476	0.96474	0.95876	0.96296	0.96401	0.96682	0.96690	0.96692	1.00000	1.00000	1.00000
ARI, a. u.	0.96162	0.96256	0.96252	0.95005	0.95628	0.95754	0.96643	0.96663	0.96685	1.00000	1.00000	1.00000
ICC, a. u.	0.96515	0.96545	0.96542	0.95979	0.96006	0.96015	0.96652	0.96666	0.96685	1.00000	1.00000	1.00000
MI, a. u.	0.90682	0.90641	0.90379	0.80196	0.55956	0.46427	0.34288	0.17243	0.15422	0.13632	0.12328	0.11224
VOI, a. u.	0.02804	0.02331	0.02363	0.07042	0.03681	0.02721	0.00158	0.00046	0.00012	0.00000	0.00000	0.00000
GCE, a. u.	0.00264	0.00217	0.00220	0.00815	0.00396	0.00291	0.00011	0.00003	0.00001	0.00000	0.00000	0.00000
PBD, a. u.	0.00001	0.00001	0.00001	0.00003	0.00003	0.00003	0.00000	0.00000	0.00000	0.00000	0.00000	0.00000
TPR, a. u.	0.96402	0.96433	0.96434	0.95391	0.95431	0.95382	0.96627	0.96679	0.96693	1.00000	1.00000	1.00000
TNR, a. u.	0.96655	0.96673	0.96669	0.96646	0.96676	0.96689	0.96692	0.96692	0.96693	1.00000	1.00000	1.00000
PRN, a. u.	0.96629	0.96658	0.96652	0.96577	0.96591	0.96659	0.96677	0.96652	0.96677	1.00000	1.00000	1.00000
FMS, a. u.	0.96515	0.96545	0.96543	0.95980	0.96007	0.96016	0.96652	0.96666	0.96685	1.00000	1.00000	1.00000
ACU, a. u.	0.96561	0.96584	0.96583	0.96283	0.96494	0.96547	0.96688	0.96692	0.96693	1.00000	1.00000	1.00000
FPR, a. u.	0.00038	0.00020	0.00024	0.00047	0.00017	0.00004	0.00001	0.00001	0.00000	0.00000	0.00000	0.00000
TIME, ms	344	406	437	328	281	297	250	250	266	234	234	250

Appendix 40. Analysis of *PTV_WB* similarity characteristics: comparison of 14th plan image with reference plan image

The threshold value, a. u.	0.0	0.1	0.2	0.3	0.4	0.5	0.6	0.7	0.8	0.9	0.95	0.99
DICE, a. u.	0.94525	0.94556	0.94557	0.94227	0.94001	0.93986	0.94645	0.94661	1.00000	1.00000	1.00000	1.00000
JAC, a. u.	0.94335	0.94399	0.94400	0.93744	0.93299	0.93269	0.94575	0.94608	1.00000	1.00000	1.00000	1.00000
AUC, a. u.	0.94534	0.94559	0.94559	0.94453	0.94300	0.94208	0.94682	0.94707	1.00000	1.00000	1.00000	1.00000
KAP, a. u.	0.94412	0.94464	0.94466	0.94028	0.93879	0.93897	0.94640	0.94660	1.00000	1.00000	1.00000	1.00000
RI, a. u.	0.94432	0.94482	0.94485	0.94150	0.94299	0.94399	0.94696	0.94709	1.00000	1.00000	1.00000	1.00000
ARI, a. u.	0.94147	0.94246	0.94252	0.93549	0.93604	0.93703	0.94629	0.94657	1.00000	1.00000	1.00000	1.00000
ICC, a. u.	0.94524	0.94556	0.94557	0.94226	0.94001	0.93986	0.94645	0.94661	1.00000	1.00000	1.00000	1.00000
MI, a. u.	0.88733	0.88716	0.88493	0.79655	0.54793	0.45375	0.33544	0.16875	0.15955	0.13632	0.12328	0.11224
VOI, a. u.	0.02914	0.02404	0.02364	0.05347	0.04072	0.03137	0.00258	0.00083	0.00000	0.00000	0.00000	0.00000
GCE, a. u.	0.00283	0.00233	0.00230	0.00565	0.00416	0.00315	0.00019	0.00006	0.00000	0.00000	0.00000	0.00000
PBD, a. u.	0.00001	0.00001	0.00001	0.00002	0.00003	0.00003	0.00000	0.00000	0.00000	0.00000	0.00000	0.00000
TPR, a. u.	0.94567	0.94411	0.94409	0.94504	0.94008	0.93762	0.94656	0.94701	1.00000	1.00000	1.00000	1.00000
TNR, a. u.	0.94690	0.94707	0.94710	0.94402	0.94592	0.94654	0.94709	0.94712	1.00000	1.00000	1.00000	1.00000
PRN, a. u.	0.94672	0.94702	0.94706	0.93952	0.93995	0.94211	0.94634	0.94621	1.00000	1.00000	1.00000	1.00000
FMS, a. u.	0.94525	0.94556	0.94557	0.94227	0.94001	0.93986	0.94645	0.94661	1.00000	1.00000	1.00000	1.00000
ACU, a. u.	0.94573	0.94598	0.94600	0.94432	0.94506	0.94557	0.94706	0.94712	1.00000	1.00000	1.00000	1.00000
FPR, a. u.	0.00025	0.00007	0.00005	0.00313	0.00123	0.00061	0.00006	0.00003	0.00000	0.00000	0.00000	0.00000
TIME, ms	328	344	375	313	281	297	250	250	250	250	250	234

Appendix 41. Analysis of *PTV_WB* similarity characteristics: comparison of 15th plan image with reference plan image

The threshold value, a. u.	0.0	0.1	0.2	0.3	0.4	0.5	0.6	0.7	0.8	0.9	0.95	0.99
DICE, a. u.	0.95723	0.95791	0.95853	0.95152	0.92001	0.89797	0.80069	0.59339	0.88591	0.84298	0.81029	0.78412
JAC, a. u.	0.95189	0.95323	0.95446	0.94065	0.88100	0.84145	0.68539	0.42888	0.82051	0.74978	0.69958	0.66146
AUC, a. u.	0.95733	0.95798	0.95861	0.95387	0.95142	0.94971	0.94767	0.94461	0.95949	0.95969	0.95943	0.95930
KAP, a. u.	0.95405	0.95516	0.95618	0.94701	0.91241	0.88956	0.78691	0.57914	0.88393	0.84035	0.80726	0.78089
RI, a. u.	0.95466	0.95572	0.95667	0.94989	0.93715	0.93324	0.91181	0.90055	0.95491	0.95226	0.95052	0.94959
ARI, a. u.	0.94662	0.94873	0.95065	0.93630	0.89594	0.87223	0.76183	0.55806	0.88019	0.83560	0.80194	0.77537
ICC, a. u.	0.95722	0.95789	0.95852	0.95149	0.91996	0.89791	0.80059	0.59326	0.88589	0.84296	0.81027	0.78410
MI, a. u.	0.88160	0.88287	0.88399	0.78018	0.50463	0.40415	0.26194	0.11328	0.13704	0.11307	0.09974	0.08923
VOI, a. u.	0.06807	0.06029	0.05348	0.10856	0.17155	0.18467	0.25142	0.26079	0.05294	0.06481	0.07206	0.07536
GCE, a. u.	0.00796	0.00691	0.00595	0.01276	0.02493	0.02823	0.04479	0.04648	0.00719	0.00928	0.01052	0.01108
PBD, a. u.	0.00002	0.00002	0.00002	0.00004	0.00018	0.00027	0.00076	0.00235	0.00033	0.00054	0.00071	0.00086
TPR, a. u.	0.95222	0.95348	0.95476	0.94830	0.95383	0.95227	0.96056	0.95949	0.96027	0.96205	0.96241	0.96263
TNR, a. u.	0.96243	0.96248	0.96246	0.95944	0.94902	0.94714	0.93478	0.92972	0.95872	0.95733	0.95644	0.95597
PRN, a. u.	0.96229	0.96237	0.96233	0.95475	0.88850	0.84952	0.68645	0.42951	0.82224	0.75013	0.69969	0.66146
FMS, a. u.	0.95723	0.95791	0.95853	0.95152	0.92001	0.89797	0.80069	0.59339	0.88591	0.84298	0.81029	0.78412
ACU, a. u.	0.95863	0.95916	0.95964	0.95622	0.94972	0.94770	0.93651	0.93052	0.95876	0.95742	0.95654	0.95606
FPR, a. u.	0.00020	0.00015	0.00017	0.00319	0.01362	0.01549	0.02785	0.03291	0.00391	0.00531	0.00619	0.00667
TIME, ms	375	406	437	375	313	328	375	328	250	282	281	250

Appendix 42. Analysis of *CTV_WB* similarity characteristics at threshold 0.4: comparison of all plan images with reference plan image

	1	2	3	4	5	6	7	8	9	10	11	12	13	14	15
DICE,a. u.	0.95817	0.95020	0.91059	0.91048	0.92040	0.93066	0.94017	0.95523	0.95517	0.95025	0.88113	0.94028	0.95006	0.94930	0.91003
JAC, a. u.	0.91970	0.94266	0.90303	0.90038	0.91161	0.91885	0.93000	0.91430	0.91419	0.94276	0.87368	0.93282	0.94248	0.94099	0.87000
AUC, a. u.	0.98886	0.95313	0.91173	0.91275	0.92236	0.97253	0.94197	0.98846	0.98855	0.95324	0.88457	0.94335	0.95245	0.95325	0.94177
KAP, a. u.	0.95028	0.94881	0.90920	0.90862	0.91879	0.96739	0.93830	0.94675	0.94668	0.94887	0.87975	0.93891	0.94867	0.94776	0.90172
RI, a. u.	0.97376	0.95317	0.91359	0.91452	0.92390	0.93119	0.94425	0.97184	0.97180	0.95320	0.88406	0.94322	0.95305	0.95257	0.92636
ARI, a. u.	0.93303	0.94567	0.90607	0.90442	0.91513	0.82051	0.93408	0.92827	0.92817	0.94574	0.87664	0.93579	0.94551	0.94429	0.88366
ICC, a. u.	0.95812	0.95019	0.91058	0.91047	0.92039	0.89051	0.94016	0.95518	0.95512	0.95024	0.88112	0.94027	0.95005	0.94929	0.90998
MI, a. u.	0.54303	0.56971	0.54447	0.53944	0.54810	0.45616	0.55741	0.53977	0.53990	0.56991	0.52787	0.56389	0.56914	0.56828	0.51164
VOI, a. u.	0.17721	0.04527	0.04341	0.05668	0.05043	0.40416	0.05662	0.18636	0.18632	0.04505	0.04441	0.04488	0.04526	0.04931	0.18350
GCE, a. u.	0.02571	0.00469	0.00467	0.00627	0.00545	0.07152	0.00630	0.02752	0.02756	0.00466	0.00464	0.00465	0.00470	0.00519	0.02698
PBD, a. u.	0.00017	0.00003	0.00003	0.00004	0.00004	0.00051	0.00004	0.00018	0.00018	0.00003	0.00003	0.00003	0.00003	0.00003	0.00018
TPR, a. u.	0.99198	0.94969	0.90568	0.90566	0.91621	0.98017	0.93413	0.99242	0.99267	0.94995	0.88195	0.94019	0.94820	0.95048	0.94442
TNR, a. u.	0.98575	0.95656	0.91779	0.91983	0.92852	0.96489	0.94980	0.98450	0.98443	0.95653	0.88718	0.94651	0.95671	0.95601	0.93912
PRN, a. u.	0.92659	0.95071	0.91555	0.91535	0.92464	0.81614	0.94629	0.92073	0.92041	0.95054	0.88031	0.94038	0.95193	0.94813	0.87806
FMS, a. u.	0.95817	0.95020	0.91059	0.91048	0.92040	0.89066	0.94017	0.95523	0.95517	0.95025	0.88113	0.94028	0.95006	0.94930	0.91003
ACU, a. u.	0.98670	0.95550	0.91593	0.91766	0.92663	0.96724	0.94740	0.98572	0.98570	0.95552	0.88638	0.94554	0.95540	0.95516	0.93994
FPR, a. u.	0.01425	0.00130	0.00049	0.00098	0.00085	0.04143	0.00077	0.01550	0.01557	0.00133	0.00153	0.00136	0.00105	0.00175	0.01480
TIME, ms	324	288	275	283	289	542	320	373	352	322	299	337	310	320	379

Appendix 43. Analysis of *PTV_WB* similarity characteristics at threshold 0.4: comparison of all plan images with reference plan image

Plan, No	1	2	3	4	5	6	7	8	9	10	11	12	13	14	15
DICE, a. u.	0.86000	0.95004	0.94000	0.94000	0.86001	0.93411	0.94012	0.95672	0.95552	0.95001	0.92000	0.94000	0.96007	0.94001	0.92001
JAC, a. u.	0.82338	0.94271	0.93288	0.93124	0.85320	0.80849	0.93425	0.91703	0.91483	0.94416	0.91214	0.93501	0.95331	0.93299	0.88100
AUC, a. u.	0.88656	0.95059	0.94027	0.94129	0.86048	0.97707	0.94046	0.98911	0.98788	0.95161	0.92134	0.94071	0.96053	0.94300	0.95142
KAP, a. u.	0.85293	0.94877	0.93878	0.93849	0.85884	0.87384	0.93911	0.94900	0.94760	0.94900	0.91864	0.93914	0.95891	0.93879	0.91241
RI, a. u.	0.87629	0.95317	0.94305	0.94376	0.86292	0.93362	0.94262	0.97411	0.97344	0.95248	0.92337	0.94211	0.96296	0.94299	0.93715
ARI, a. u.	0.83762	0.94592	0.93601	0.93508	0.85619	0.83256	0.93683	0.93225	0.93043	0.94672	0.91558	0.93720	0.95628	0.93604	0.89594
ICC, a. u.	0.85995	0.95003	0.93999	0.93999	0.86000	0.89397	0.94012	0.95667	0.95547	0.95000	0.91999	0.93999	0.96006	0.94001	0.91996
MI, a. u.	0.46672	0.55240	0.54698	0.54353	0.49973	0.46488	0.54949	0.52645	0.52317	0.55558	0.53336	0.55120	0.55956	0.54793	0.50463
VOI, a. u.	0.16528	0.03952	0.03770	0.04719	0.03642	0.34697	0.03240	0.17401	0.17965	0.03437	0.04322	0.02911	0.03681	0.04072	0.17155
GCE, a. u.	0.02337	0.00430	0.00417	0.00515	0.00399	0.06250	0.00344	0.02531	0.02601	0.00344	0.00463	0.00292	0.00396	0.00416	0.02493
PBD, a. u.	0.00016	0.00003	0.00003	0.00004	0.00003	0.00046	0.00002	0.00018	0.00018	0.00002	0.00003	0.00002	0.00003	0.00003	0.00018
TPR, a. u.	0.88452	0.94391	0.93339	0.93416	0.85420	0.99324	0.93498	0.99225	0.98976	0.94796	0.91521	0.93667	0.95431	0.94008	0.95383
TNR, a. u.	0.88860	0.95728	0.94715	0.94842	0.86675	0.96091	0.94595	0.98597	0.98599	0.95526	0.92747	0.94475	0.96676	0.94592	0.94902
PRN, a. u.	0.83680	0.95625	0.94671	0.94592	0.86589	0.81297	0.94532	0.92365	0.92357	0.95206	0.92485	0.94335	0.96591	0.93995	0.88850
FMS, a. u.	0.86000	0.95004	0.94000	0.94000	0.86001	0.89411	0.94012	0.95672	0.95552	0.95001	0.92000	0.94000	0.96007	0.94001	0.92001
ACU, a. u.	0.88800	0.95533	0.94514	0.94634	0.86492	0.96563	0.94435	0.98689	0.98654	0.95420	0.92568	0.94357	0.96494	0.94506	0.94972
FPR, a. u.	0.01143	0.00021	0.00009	0.00051	0.00017	0.03909	0.00013	0.01403	0.01401	0.00066	0.00053	0.00029	0.00017	0.00123	0.01362
TIME, ms	313	281	266	313	281	436	297	328	328	297	281	281	281	281	313